

Fluid-Particle Interaction in Geophysical Flows Debris Flows

Paloma Paleo Cageao

A Thesis presented for the degree of
Doctor of Philosophy



University of Nottingham
England
April 2014

Dedicated to

My daughter, my dear Ariadna, who, from her small world of understanding, has had constant patience with me, and has showed excitement and admiration always for my work. To my parents Rafael and Celia, who have given me strength, encouragement and motivation, in this, and in my life. To my sister Teresa, who has never failed in the giving of her constant and caring support. I would like to make a special dedication our little Roman, dearly loved, having given his gift of beautiful memories, he will be forever missed.

Dedicada a

Mi querida hija Ariadna que, desde su pequeño mundo de entendimiento, ha sido siempre paciente conmigo, mostrando interés y admiración por mi trabajo. A mis padres Rafael y Celia, quienes me han dado fuerzas, coraje y motivación, en esto como en todos los caminos de mi vida. A mi hermana Teresa, que nunca ha fallado en su constante y cariñosa ayuda.

Quisiera hacer una especial dedicación a nuestro pequeño Román, que nos dejó maravillosos recuerdos y a quien siempre echaremos de menos.

Abstract

Small scale laboratory experiments were conducted to study the dynamic morphology and rheological behaviour of fluid-particle mixtures, such as snout-body architecture, levee formation, deposition and particle segregation effects. Debris flows consist of an agitated mixture of rock and sediment saturated with water. They are mobilized under the influence of gravity from hill slopes and channels and can reach long run-out distance and have extremely destructive power. Better understanding of the mechanisms that govern these flows is required to assess and mitigate the hazard of debris flows and similar geophysical flows. Debris flow models are required to accurately deal with evolving behaviours in space and time, to be able to predict flow height, velocity profiles and run-out distances and shapes. The evolution of laboratory debris flows, both dry glass beads and mixtures with water or glycerol, released from behind a lock gate to flow down an inclined flume, was observed through the channel side wall and captured with high speed video and PIV analysis to provide velocity profiles through out the flow depth. Pore pressure and the normal and shear stress at the base of the flow were also measured.

Distinct regions were characterized by the non-fluctuating region and the intermittent granular cloud surrounding the flows. The extent of these regions was shown to be related to flow properties. The separation of these two regions allowed the systematic definition of bulk flow characteristics such as characteristic height and flow front position. Laboratory flows showed variations in morphology and rheological characteristics under the influence of particle size, roughness element diameter, interstitial fluid viscosity and solid volume fraction. Mono-dispersed and poly-dispersed components mixed with liquids without fine sediments, reveal a head and body structure and an appearance similar to the classic anatomy of real debris flows. Unsaturated fronts were observed in mono-dispersed flows, suggesting that particle segregation is not the only mechanism.

A numerical simulation of laboratory debris flows using the computer model RAMMS (RAPid Mass Movements Simulation) was tested with dry laboratory flows, showing close similarity to calculated mean velocities.

Acknowledgements

I would like to express my sincere gratitude to my supervisor Dr Barbara Turnbull who gave me the opportunity to do this PhD, and for her constructive involvement from the beginning of my research to its conclusion.

I owe a very important debt to Dr Perry Bartel who has been extraordinarily supportive and for giving me such warm encouragement.

This research has been supported by the WSL Institute for Snow and Avalanche research SLF and EPSRC DTG funds.

I am particularly grateful for the assistance given by Jim Meakin and Steve Gange, for their help in the laboratory, for the building of the flume, and for making the long hours of experiments enjoyable.

I would like to thank Dr Jim McElwaine and Dr Stuart Dalziel for their advice and support; Dr Dave Hargreaves for his help finishing my thesis; and my examiner Dr Barry Azzopardi for his feedback.

My deepest heartfelt thanks to my family, especially my parents, my sister, and my cousin Carmen; my friends and research colleagues from C11, in particular Bruce; my thanks to Raquel and Laura for putting up with me on a daily basis; and my dear friends Eva, Noelia, Carlos and Danny.

Contents

Abstract	iii
Acknowledgements	iv
Notation	xxiii
1 Introduction	1
1.1 Background	1
1.2 Debris flow definition	2
1.3 Debris flow from initiation to deposition	3
1.3.1 Initiation	4
1.3.2 Transportation	4
1.3.3 Deposition	7
1.4 Mechanical classification of debris flow	8
1.5 Mathematical modelling of debris flows	11
1.5.1 Continuum models	11
1.5.2 Multi-phase models	15
1.6 Physical modelling of debris flows	16
1.6.1 Field measurements and large-scale debris flows	16
1.6.2 Small-scale debris flows	18
1.7 Summary	19
1.8 Structure of the thesis	20
2 Flume experiments	21
2.1 Laboratory modelling design	21

2.2	Experimental set up	25
2.2.1	Flow mixtures	28
2.3	Measurements Methods	28
2.3.1	Sensors	28
2.3.2	Data acquisition and processing	35
2.3.3	Image acquisition	36
2.4	Data Analysis	37
2.4.1	Particle Image Velocimetry technique	37
2.4.2	Image processing	39
2.4.3	Characteristic front flow position and flow height	43
2.5	Conclusions	45
3	Morphological characteristics of laboratory debris flow	46
3.1	The structure of laboratory debris flows	48
3.1.1	Effect of particle and roughness element diameters on structure	50
3.1.2	Effect of interstitial fluid on structure	56
3.1.3	Effect of solid volume fraction on structure	58
3.2	Segregation	61
3.3	Unsaturated flow front	64
3.4	Deposition	66
3.5	Conclusions	74
4	Experimental results	75
4.1	Flow evolution	75
4.1.1	Effect of particle and roughness element diameters	77
4.1.2	Effect of interstitial fluid	85
4.1.3	Effect of solid volume fraction	91
4.2	Flow friction: Shear and normal stress ratio	98
4.3	Conclusions	100
5	Experimental flow simulation with RAMMS	102
5.1	Numerical Model	102

Contents	vii
5.1.1 Governing equations	102
5.1.2 Constitutive relations	105
5.1.3 Numerical solution	106
5.1.4 Model input	107
5.1.5 Model results	108
5.2 Conclusions	113
6 Conclusions	114
References	116

List of Figures

1.1	(a) Debris flow deposits from the December 1999 event in Carraballeda, coastal Venezuela. The debris flow front was estimated as 3.5 m in height, leaving 1 m boulders on second floor of a building. (b) House partially buried by the passage of a debris flow triggered by rapid snow melt in May 1983, in Slide Mountain, Nevada (USA). Both photographs by U.S. Geological Survey.	2
1.2	Idealized representation of a typical debris flow path (Schematic diagram from www.dnv.org).	3
1.3	(a) Advancing surge of viscous debris flow in the Jiangjia Gully, China (Photography from Disaster Prevention Research Institute Kyoto University). Characteristic surge height ~ 3 m and frontal velocity $\sim 10 \text{ m s}^{-1}$. (b) Laboratory study on surge instability in custard power suspensions flowing down on 20° inclined plane.	4
1.4	Schematic representation of the characteristic parts of a debris flow. .	5
1.5	Large boulders were transported by the debris flows in Venezuela December 1999. Using the person standing on debris flow deposits as scale, the boulders are of order 4–5 m in diameter. Photographs by U.S. Geological Survey.	6
1.6	Formation of a ‘plug’ in the upper layer h_p , where the shear stress τ is smaller than the yield stress τ_o and the velocity is constant. In the lower layer h_s , the velocity increases with the height above the bed due to shearing.	13

1.7	(a) Debris flow catchment at Dorbach Randa in the Matter Valley, Switzerland. (b) Topographical map of Illagraben showing the distribution of the instrument devices. Debris flows in a northerly direction in this catchment. Courtesy of WSL (Swiss Federal Institute for Forest, Snow and Landscape Research).	17
1.8	Debris flow descending the U.S. Geological Survey debris flume. Debris flow material of $\sim 10 \text{ m}^3$ down a 95 m flume of 31° incline.	18
2.1	Schematic illustration of the flume with a lock gate and run-out tray.	25
2.2	Photographs of the lock gate (a) before release of a mixture of glass beads of 2×10^{-3} m in water with a solid volume fractions 0.6 and (b) after releasing the mixture.	26
2.3	Flume bed surface with different roughness element diameter (a) $d_{r1} = 0$ m, (b) $d_{r2} = 2 \times 10^{-3}$ m, (c) $d_{r3} = 4 \times 10^{-3}$ m and (d) $d_{r4} = 8 \times 10^{-3}$ m.	27
2.4	(a) Opening in the base of the flume to locate the metal plate which holds the sensors for easy assembly. (b) Metal plate with the sensors..	27
2.5	(a) Top front view of the flume showing the sensor location (highlighted with a circle) with a 0 m roughness element surface. (b) Zoom in of the pore pressure sensor (left) covered with a metal grid and the force plate (right) with a 0 m and (c) 4×10^{-3} m roughness element diameter cover. (d) Interchangeable circular plates to cover the force plate to match the corresponding roughness element diameter of the base; from left to right 8×10^{-3} , 4×10^{-3} , 2×10^{-3} and 0 m roughness element diameter.	29
2.6	Calibration curve of the differential pressure transducer. The voltage output from the sensor is converted to pressure using linear regression with a coefficient of determination $R^2 > 0.997$. The dashed lines delineate the 95% confidence intervals.	30
2.7	Assembly view sketch of the sensors located beneath the flume. . . .	31
2.8	Calibration system (a) without weights and (b) with the calibrated weights. (c) Sketch of the calibration arrangement.	32

- 2.9 Calibration curves for the (a) normal and (b) shear forces. The voltage output from the sensor is converted to pressure using linear regression with a coefficient of determination $R^2 > 0.997$ and $R^2 > 0.999$ for normal and shear forces respectively. The dashed lines delineate the 95% confidence intervals. 33
- 2.10 Calibration curves for the normal and shear forces under a dynamic applied load by realising 10^{-3} m^3 of water from behind the lock gate of the flume. 34
- 2.11 (a) Front view of the flow approaching the sensors. The centre line of the sensors is shown. The circles with solid and dashed lines delineate the pore pressure sensor and the force plate respectively. (b) The flow edge passes the centre line of the force plate sensor before reaching the pore pressure sensor due to their relative streamwise location. . . 36
- 2.12 Illustration of the flume with a built-in lock gate and adjacent run-out tray. 37
- 2.13 (a) Original image before being processed and (b) the corresponding histogram of the pixel intensity values. Intensity level of the histogram should be cover from 0 to 255, however it only shows relevant data which occurs until 100 intensity level. 40
- 2.14 (a) Enhanced contrast of the grey scale image. (b) Histogram of the pixel intensity. Intensity level of the histogram should be cover from 0 to 255, however it only shows relevant data which occurs until 100 intensity level. 40

- 2.15 (a) The binary image obtained by grey level thresholding Otsu's method and (b) after dilation with filled holes. (c) The grey scale image before masking the background. The edge of the flow is highlighted with a line around the flow, which corresponds to the perimeter of the above image. The dashed line box marks the maxima region of the flow, which delimits the solid line polygon size. The index defined by the polygon were added as part of the foreground region. (d) The grey scale image after masking the background of the foreground. 42
- 2.16 (a) Colour map visualising the standard deviation of the velocities from the local 14 frame average, of a mixture with 8×10^{-3} m particle diameter mixed in water with solid volume fraction 0.6 over a 8×10^{-3} m roughness element diameter. Colour bar represents the standard deviation in m s^{-1} from blue (low standard deviation) to red (high standard deviation). (b) The edges correspond to the standard deviations, with white and grey line corresponding to the non-fluctuating region with low standard deviation ($< 150 \times 10^{-3} \text{ m s}^{-1}$) and intermittent collisional region with high standard deviation ($\geq 150 \times 10^{-3} \text{ m s}^{-1}$) respectively. The edge of the two regions are superimposed with the 14th frame of the corresponding block. (c) The convex hull of the non-fluctuating edge values corresponds to the dashed line. The front position is highlighted with a small circle. . . . 44
- 2.17 Schematic of the flow moving down a flume with an inclination angle of $\theta = 27^\circ$. The flow is divided in two regions. Pseudo-plug region, with the low standard deviation from the local average, shaded light grey and intermittent collisional region with high standard deviation is shaded dark grey. The characteristic height of the flow and front flow position are defined by the non-fluctuating region as h and x_f respectively. The total flow height H includes the intermittent collisional region. 44

- 3.1 Side view of a laboratory experimental flow demonstrating reproducible key feature of natural debris flows. The release of $1 \times 10^{-3} \text{ m}^3$ volume of a mixture of particles from $2 \times 10^{-3} \text{ m}$ (colourless), $4 \times 10^{-3} \text{ m}$ (black) to $8 \times 10^{-3} \text{ m}$ (white) to solid volume fraction of 0.6 in water over a roughness element of $8 \times 10^{-3} \text{ m}$, moving down a flume with an inclination angle of 27° . The percentage of the release volumes were 50 %, 30 % and 20 % of 2×10^{-3} , 4×10^{-3} and $8 \times 10^{-3} \text{ m}$ particle diameters respectively. (a) A granular front characterized by low fluid content and by the accumulation of large particles, follow by (b) the non-fluctuating region or core of the flow, and (c) the tail mostly liquefied with some scattered big particles. 47
- 3.2 Front flow evolution of poly-disperse mixture of solid volume fraction 0.6 with water at $t = 0.39 \text{ s}$ and 0.46 s since gate opening. The blue line depicts edge of the front flow. 48
- 3.3 Colour map visualising regions of non-fluctuating (light grey corresponding to standard deviation $\leq 150 \times 10^{-3} \text{ m s}^{-1}$) and intermittent collisional behaviour (dark grey corresponding to standard deviation $> 150 \times 10^{-3} \text{ m s}^{-1}$) through the flow depth z along the length of the flume x , at the flow front position $x_f = 350 \times 10^{-3} \text{ m}$. Columns are arranged by particle size, from mono-disperse $2 \times 10^{-3} \text{ m}$ flows to mixtures of 2×10^{-3} , 4×10^{-3} and $8 \times 10^{-3} \text{ m}$ particles. Rows are arranged by roughness element diameter from 2×10^{-3} , 4×10^{-3} to $8 \times 10^{-3} \text{ m}$. Flows consist in particles mixed in water to a solid volume fraction of 0.6. Quiver plots of local velocity average at positions 10%, 50% and 90% distance from the nose of the flow, scaled accordingly to the legend. 52

- 3.4 Colour map visualising regions of non-fluctuating behaviour through the flow depth z along the length of the flume x , at the flow front position $x_f = 350 \times 10^{-3}$ m. Intermittent collisional behaviour is not shown. The flow boundary depicted with a grey line. Columns are arranged by particle size, from mono-disperse 2×10^{-3} m to mixtures of 2×10^{-3} , 4×10^{-3} and 8×10^{-3} m particles. Rows are arranged by roughness element diameter from 2×10^{-3} , 4×10^{-3} to 8×10^{-3} m. Flows consist in particles mixed in water to a solid volume fraction of 0.6. Colour bar represents standard deviation from 14 frame average velocities in m s^{-1} , from blue (zero standard deviation) to orange ($150 \times 10^{-3} \text{ m s}^{-1}$ standard deviation) with same scale for the all the flows. 53
- 3.5 Influence of roughness element on the flow head. Left and right column for 0 and 8×10^{-3} m roughness element diameter respectively. Rows are arranged by particle size, from mono-disperse 2×10^{-3} m flows to mixtures of 2×10^{-3} , 4×10^{-3} and 8×10^{-3} m particles. Flows consist of particle mixed with water to a solid volume fraction of 0.6. 54
- 3.6 Influence of roughness element on the flow head where $d_p = d_r$. Flows consist of particle mixed with water to a solid volume fraction of 0.6. 56
- 3.7 Colour map visualising regions of non-fluctuating (light grey corresponding to standard deviation $\leq 150 \times 10^{-3} \text{ m s}^{-1}$) and intermittent collisional behaviour (dark grey corresponding to standard deviation $> 150 \times 10^{-3} \text{ m s}^{-1}$) through the flow depth y along the length of the flume x , at the flow front position $x_f = 350 \times 10^{-3}$ m. Columns are arranged by particle size, from mono-disperse 2×10^{-3} m to mixtures of 2×10^{-3} , 4×10^{-3} and 8×10^{-3} m particles. Rows are arranged by interstitial fluids; dry, water, glycerol. All flows have roughness element diameter of 8×10^{-3} m and solid volume fraction of 0.6. Quiver plots of local velocity average at positions 10%, 50% and 90% distance from the nose of the flow, scaled accordingly to the legend. 57

- 3.8 Effect produced on the flow head when adding glycerol as interstitial fluid. Columns are arranged by dry flows on the left and glycerol mixtures with solid volume fraction 0.6 on the right. Rows are sorted by particle size, from mono-disperse 2×10^{-3} m flows to mixtures of 2×10^{-3} , 4×10^{-3} and 8×10^{-3} m particles. The roughness element diameter of 8×10^{-3} m remained fixed. 59
- 3.9 Colour map visualising regions of non-fluctuating and intermittent collisional behaviour through the flow depth y along the length of the flume x , at the flow front position $x_f = 350 \times 10^{-3}$ m with roughness element diameter 8×10^{-3} m. Columns are arranged by particle size, from mono-disperse 2×10^{-3} m to mixtures of 2×10^{-3} , 4×10^{-3} and 8×10^{-3} m particles. Rows are arranged by interstitial fluids (water and glycerol) and by solid volume fraction (0.4 and 0.6). Colour bar represents standard deviation from 14 frame average velocities in m s^{-1} , from blue (low standard deviation) to red (high standard deviation) with the same scale for the all flows. Dark blue represents non-fluctuating region of low granular temperature (standard deviation $\leq 150 \times 10^{-3} \text{ m s}^{-1}$). Colours from cyan, yellow, orange to red define the intermittent collisional behaviour (standard deviation $> 150 \times 10^{-3} \text{ m s}^{-1}$). 60
- 3.10 Side view of flows with solid volume fraction of 0.4, moving down a flume with at inclination 27° and a roughness element diameter of 8×10^{-3} m, consisting of 1 litre (a) mixed 2×10^{-3} (colourless), 4×10^{-3} (black) and 8×10^{-3} m (white) glass beads in glycerol. (b) 8×10^{-3} m glass beads in glycerol. In the poly-disperse case a fast moving layer of liquid forms at the top surface of the flow. For the mono-disperse flow, a dry granular front is formed followed by a saturated tail, with no fluid layer formed. 61

- 3.11 Shape of flow head in glycerol mixtures to different solid volume fractions. Columns are arranged by solid volume fraction 0.4 on the left and 0.6 on the right. Rows are sorted by particle size, from mono-disperse 2×10^{-3} m flows to mixtures of 2×10^{-3} , 4×10^{-3} and 8×10^{-3} m particles. The roughness element diameter of 8×10^{-3} m remained fixed. 62
- 3.12 Schematic of particle size segregation in an experimental debris flows with mixtures of particles moving down an inclined flume. Small particles percolate into the random space to the base of the flume, surpassing larger particles in the upper layers. the velocity distribution shows the faster layers on the top. The large particles near the free surface, tend to migrate to the front of the flow. 63
- 3.13 Particle size segregation in experimental flow of a dry mixture of particles from 2×10^{-3} (colourless), 4×10^{-3} (black) to 8×10^{-3} m (white) moving down a flume with a roughness element diameter of 8×10^{-3} m. Front of the flow, which contains high concentration of larger particles accompanied by a small particles cloud, separates from the body. The flow body decelerates to eventually stops within the flume. 64
- 3.14 Time evolution of the (a) flow height H , and (b) pore pressure, normal and shear stresses at the sensor location, 232×10^{-3} m from the gate of the flume. The flow consists of 2×10^{-3} m particles with solid volume fraction 0.6 over 8×10^{-3} m rough element diameter. Arrival of the flow at $t = 0.37$ s. 65
- 3.15 Time evolution of the (a) flow height H , and (b) pore pressure, normal and shear stresses at the sensor location, 232×10^{-3} m from the gate of the flume. The flow consists of mixed particles of 2×10^{-3} , 4×10^{-3} and 8×10^{-3} m with solid volume fraction 0.6 over 8×10^{-3} m rough element diameter. Arrival of the flow at $t = 0.28$ s. 66

- 3.16 Front camera images of the experimental flows run-out showing formation of lateral levees (a) with poly-disperse particles from 2×10^{-3} , 4×10^{-3} to 8×10^{-3} m to solid volume fraction 0.6 with water and (b) with mono-disperse of 8×10^{-3} m particles, to solid volume fraction 0.4 with glycerol. Liquefied core material is observed in the central region and accreted particles around the perimeter of the flow. Roughness element fixed to 8×10^{-3} m at the flume. Smooth run-out tray surface. 69
- 3.17 Deposits of laboratory debris flows showing variations with roughness element diameter and particle size in the flows. Columns are arranged by particle size, from mono-disperse 2×10^{-3} m flows to mixtures of 2×10^{-3} , 4×10^{-3} and 8×10^{-3} m particles. Rows are arranged by roughness element diameter of 0, 2×10^{-3} , 4×10^{-3} m and 8×10^{-3} m. Flows consist of particles mixed in water with solid volume fraction 0.6 and with a smooth run-out tray surface. 70
- 3.18 Deposits of laboratory debris flows varying with interstitial fluid. Columns are arranged by particle size from mono-disperse 2×10^{-3} m flows to mixtures of 2×10^{-3} , 4×10^{-3} and 8×10^{-3} m particles. Rows are arranged by type of interstitial fluid: dry, water or glycerol. The roughness element diameter of 2×10^{-3} m, volume fraction 0.6 and smooth run-out tray surface are the same for all flows. 71
- 3.19 Deposits of laboratory debris flows consisting of 1 litre of mixed 2×10^{-3} (colourless), 4×10^{-3} (black) and 8×10^{-3} m (white) particles. Columns are arranged by particle solid volume fraction: 0.4 (maximum fluid content), 0.5 and 0.6 (minimum fluid content). Rows are arranged by type of interstitial fluid, water or glycerol. The roughness element diameter of 2×10^{-3} m and smooth run-out tray surface are the same for all flows. 72

- 3.20 Deposits of laboratory debris flows consisting of 1 litre of mixed of particles. Columns are arranged by solid volume fraction, 0.7, 0.6 and 0.4. Rows are arranged by particles with 2×10^{-3} or 4×10^{-3} m diameter and interstitial fluid water or glycerol. The roughness element diameter of 2×10^{-3} m and smooth run-out tray surface are the same for all flows. 73
- 4.1 (a) Edge of the flow superimposed on the side view of a laboratory experimental flow. On the right of the image the gate is located corresponding to $x = 0$ m and $t = 0$ s. (b) Schematic of the flow showing the the pseudo-plug and intermittent collisional regions, shaded light and dark grey respectively. The characteristic flow height and front flow position are defined by the pseudo-plug region as h and x_f respectively. The total flow height H includes the extend of the intermittent collisional region. (c) Sensor position and σ normal stress and τ shear stress. 76
- 4.2 Flow evolution from the arrival of the flow to the sensor located at 232×10^{-3} m from the gate of water flow mixtures with solid volume fraction 0.6 over 8×10^{-3} m roughness element diameter of mono-disperse (a-e) 2×10^{-3} m and (f-j) 4×10^{-3} m particles diameter. . . . 79
- 4.3 Flow evolution from the arrival of the flow to the sensor located at 232×10^{-3} m from the gate of water flow mixtures with solid volume fraction 0.6 over 8×10^{-3} m roughness element diameter of (a-e) 8×10^{-3} m and (f-j) 2,4 and 8×10^{-3} m particles diameter. 80
- 4.4 Average velocity profiles within the pseudo-plug region at 50% flow length from the front. Flows consist in particles mixed in water to a solid volume fraction of 0.6 for different roughness element diameters from (a) 2×10^{-3} m, (b) 4×10^{-3} m to (c) 8×10^{-3} m. Dashed black lines represents the fit power law (Equation 4.1.5). The particle diameter of the experimental flows is represented by the grey lines becoming lighter by increasing particle diameter from 2, 4, 8×10^{-3} m and poly-disperse mixture with a mean diameter of 4×10^{-3} 81

- 4.5 Top view of small particles trapped between the large roughness element. 83
- 4.6 Time dependence of front position x_f (a-d) and height of the flow h (e-f). Rows are arranged by particle size, from mono dispersed 2×10^{-3} m flows to mixtures of 2×10^{-3} , 4×10^{-3} and 8×10^{-3} m particles versus roughness element diameter from 0, 2×10^{-3} , 4×10^{-3} and 8×10^{-3} m. Flows consist of particles mixed in water to a solid volume fraction of 0.6. The flow heights and velocities front are considered within the pseudo-plug region. 84
- 4.7 Flow evolution from the arrival of the flow to the sensor located at 232×10^{-3} m from the gate flows consisting of 2×10^{-3} m particles diameter over 8×10^{-3} m roughness element diameter (a-e) dry and with solid volume fraction 0.6 (f-j) water and (k-o) glycerol as interstitial fluid. 86
- 4.8 Average velocity profiles within the pseudo-plug region at 50% flow length from the front. Flows consist in (a) dry flows, and mixed to solid fraction of 0.6 with (b) water and (c) glycerol. Dashed black lines represents the fit power law. The particle diameter of the experimental flows is represented by the grey lines becoming lighter by increasing particle diameter from 2×10^{-3} , 4×10^{-3} , 8×10^{-3} m and poly-disperse mixture with a mean diameter of 4×10^{-3} m. 87
- 4.9 Series of side images showing the evolution of the flow after releasing 1 litre volume of mixed glass beads, 2×10^{-3} m (colourless), 4×10^{-3} m (black painted) to 8×10^{-3} m (white painted). These are mixed with glycerol to a solid volume fraction of 0.6, moving down a flume with an inclination angle of 27° over a roughness element diameter of 8×10^{-3} m. The dashed blue rectangle highlight the behaviour of the bottom layer of the flow, where particles seem to move relatively much slower than the flow front. 88

- 4.10 Time dependence of front position x_f (a-d) and height of the flow h (e-f). Rows are arranged by particle size, from mono-dispersed 2×10^{-3} m flows to mixtures of 2×10^{-3} , 4×10^{-3} and 8×10^{-3} m particles versus interstitial fluid (dry, water and glycerol). The 8×10^{-3} m roughness element is remained fixed. The flow heights and velocities front are considered within the pseudo-plug region. 90
- 4.11 Flow evolution from the arrival of the flow to the sensor located at 232×10^{-3} m from the gate of 2×10^{-3} m particle mixed in water with solid volume fraction (a-e) 0.6 and (f-j) 0.4 over 8×10^{-3} m roughness element. 92
- 4.12 Average velocity profiles within the region with low standard deviation ($\leq 150 \times 10^{-3}$ m s $^{-1}$) at 50% flow length from the front. Flows consist in mixtures with water to solid fraction of (a) 0.4, (b) 0.6 and mixtures with glycerol to solid fraction of (c) 0.4 and (d) 0.6. Black lines represents the fit velocity (Equation 4.1.5). The particle diameter of the experimental flows is represented by the grey lines becoming lighter by increasing particle diameter from 2×10^{-3} , 4×10^{-3} , 8×10^{-3} m and poly-disperse mixture with a mean diameter of 4×10^{-3} m. 93
- 4.13 Side view of flows in glycerol with solid volume fraction 0.4, moving down a flume with at inclination 27° and a roughness element diameter of 8×10^{-3} m. Mono-disperse mixtures consisting of (a) 2×10^{-3} m, (b) 4×10^{-3} m and (c) 8×10^{-3} m particles. (d) Mixed 2×10^{-3} m (colourless), 4×10^{-3} m (painted black) and 8×10^{-3} m (painted white) glass beads in glycerol. Small particles (i.e. 2×10^{-3} and 4×10^{-3} m) and mixed sizes (2×10^{-3} , 4×10^{-3} and 8×10^{-3} m) cases a fast moving layer of liquid forms at the top surface of the flow. For the mono-disperse flow of 8×10^{-3} m, a dry granular front is formed followed by a saturated tail, with no fluid layer formed. . . 95

- 4.14 Time dependence of front position x_f (a-d) and height of the flow h (e-f). Rows are arranged by particle size, from mono dispersed 2×10^{-3} m flows to mixtures of 2×10^{-3} , 4×10^{-3} and 8×10^{-3} m particles versus solid volume fraction with water and glycerol as interstitial fluids. The 8×10^{-3} m roughness element is remained fixed. The flow heights and velocities front are considered within the pseudo-plug region. 97
- 4.15 Ratio of shear stress τ and normal stress σ at 232×10^{-3} m from the gate of water flow mixtures with solid volume fraction 0.6 over 8×10^{-3} m roughness element diameter of (a) 2×10^{-3} m (b) 4×10^{-3} m (c) 8×10^{-3} m and (d) 2×10^{-3} , 4×10^{-3} and 8×10^{-3} m particles diameter. 99
- 4.16 Ratio of shear stress τ and normal stress σ at 232×10^{-3} m from the gate of flows consisting of 2×10^{-3} m particles diameter (a) dry and with solid volume fraction 0.6 (b) water and (c) glycerol as interstitial fluid over 8×10^{-3} m roughness element diameter. 99
- 4.17 Ratio of shear stress τ and normal stress σ at 232×10^{-3} m from the gate of 2×10^{-3} m particle mixed in water with solid volume fraction (a) 0.6 and (b) 0.4 over 8×10^{-3} m roughness element diameter. . . . 100
- 5.1 The geometry description of the chute $Z(X, Y)$ is given in a horizontal $X - Y$ coordinates system. The local surface coordinates system (x, y, z) with the directions x and y parallel to the flow slope with an angle of θ and z direction is perpendicular to the local $x - y$ plane. The gravitational acceleration and the depth average mean velocity components are $\mathbf{g} = (g_x, g_y, g_z)$ and $\mathbf{U} = (U_x, U_y, U_z)$ respectively. . . 103
- 5.2 Comparison between measured values of the experimental laboratory flow (black line) and the simulation with RAMMS model (grey line) of the evolution of a dry mixture of mono disperse 2×10^{-3} m particle size over 2×10^{-3} m roughness element diameter. (a) Average velocity, (b) height of the flow, (c) shear stress and (d) normal stress. 109

-
- 5.3 Colour map visualising flow height from the release zone along the flume channel to the tray run-out estimated by the model. The release zone shows remaining material approximately the 20×10^{-3} m (of the 110×10^{-3} m initial height) which has not been released. 110
- 5.4 Deposit of the laboratory flow consisting of dry mixture of mono disperse 2×10^{-3} m particle size over 2×10^{-3} m roughness element diameter. 110
- 5.5 Comparison between measured values of the experimental laboratory flow (black line) and the simulation with RAMMS model (grey line) of the evolution of a dry mixture of mono disperse 2×10^{-3} m particle size over 8×10^{-3} m roughness element diameter. (a) Average velocity, (b) height of the flow, (c) shear stress and (d) normal stress.. 112

List of Tables

1.1	Evaluation of flow regime according to dimensionless numbers. Savage & Hutter 1989, Iverson & Denlinger 2001, Bagnold 1954, Iverson 1997, Iverson & LaHusen 1993.	10
1.2	Estimation of dimensionless numbers to characterize the flow regime in well-documented flows.	10
2.1	Physical properties of the materials used in all set of experiments, where V is the total volume of mixture.	22
2.2	Estimation of Froude, Fr , and particle Reynold Re_p numbers for varying interstitial fluids, solid volume fraction, particle size varies and roughness element diameter.	24
4.1	Optimised fit parameters for power law velocity profiles (Equation 4.1.5) for different particle sizes and roughness element diameters.	82
4.2	Optimised fit parameters for theoretical velocity profiles (Equation 4.1.5) for different particle sizes and interstitial fluid with a roughness diameter element of 8×10^{-3} m.	89
4.3	Optimised fit parameters for theoretical velocity profiles (Equation 4.1.5) for different particle sizes, solid volume fraction and interstitial fluid with 8×10^{-3} m roughness element diameter.	94
5.1	Summary input parameters of the simulations.	108

Notation

C	cohesion
E	output electrical signal
\hat{E}	estimated output electrical signal
E_o	offset of electric signal
\bar{E}_o	mean value of the offset of electric signal
Fr	Froude number
G	driving forces
H	total height of the flow including intermittent collisional region
K	kinetic energy
K_{HB}	consistency parameter in the Herschel-Bulkely model
N_{BAG}	Bagnold number
N_{fric}	friction number
N_{SAV}	Savage number
P	pore fluid pressure
R	random kinetic energy
R	coefficient of determination
SD	standard deviation
Re_p	particle Reynolds number
R_o	activation energy
T	stress tensor
U	average mean velocity nomenclature only in Chapter 5
\hat{U}	total flow velocity
U_r	fluctuation velocity
V	total volume

d	depth of the water (calibration process)
d_p	particle diameter
d_r	roughness surface element diameter
g	gravity acceleration
h_Ψ	equivalent height of fluid pressure
h_{max}	maximum height within non-fluctuating region
h_p	upper layer when plug formation
h_s	lower layer when plug formation
k	voltage per unit of pressure
n_i	size sample
n	index in the Herschel-Bulkely model
u	down slope velocity
u_f	characteristic velocity of the flow
u_m	mean velocity
u_{max}	maximum velocity
u_{slip}	slip velocity
u_t	surface velocity
x	distance measured along main flow direction
x_f	flow front position
z	depth of the flow
α	production coefficient of the random kinetic energy
β_R	decay coefficient of the random kinetic energy
β	exponent of the power-law distribution
$\dot{\gamma}$	strain rate (velocity gradient)
ϵ	shallowness parameter
θ	angle slope
μ	effective friction coefficient
μ_o	static friction coefficient
ξ	turbulent friction coefficient
ξ_o	static friction coefficient
ρ_{af}	apparent fluid density
ρ_f	density of the fluid
ρ_p	density of the interstitial fluid

ρ_s	bulk density
σ	normal stress
φ	internal friction angle
μ_f	fluid dynamic viscosity
τ_0	yield stress
τ	shear stress
τ_B	Bingham fluid viscosity coefficient
τ_C	yield shear stress by Morh-Coulomb failure criteria
τ_e	estimated shear stress
τ_V	turbulent friction
ϕ	solid volume fraction

Chapter 1

Introduction

1.1 Background

Many different geophysical flows are gravity driven and have dynamics determined by the interaction between fluid and particles. Some examples are snow avalanches, debris flows, pyroclastic flows and rock avalanches [Campbell, 1990; Hutter, 2005; Iverson & Vallance, 2001; Savage, 1984; Simpson, 1997; Takahashi, 2001]. They have received wide attention due to their potentially significant socio-economic and environmental impact. In addition, knowledge of the mechanics and properties of particle laden flows is essential for the understanding and solution of a diverse range of industrial problems, such as the transportation and processing of particulate materials in the food, pharmaceuticals and mineral industries and the stability of refuse heaps [Armanini *et al.* , 2005; Balmforth *et al.* , 2007; Hunt, 2000; Koos *et al.* , 2012; Potapov *et al.* , 2001; Savage, 1979].

These natural and industrial flows share many common characteristics. They consist of grain-fluid mixtures with free upper surfaces occurring under the action of gravity. When sheared, the particles may either flow in a manner similar to a fluid, or resist the shearing like a solid. Two-way coupling between fluid flow and particles makes a full understanding of their physical behaviour and the underlying mechanisms difficult to achieve [Armanini *et al.* , 2005; Campbell, 1990; Iverson, 1997; Iverson *et al.* , 2010; Pouliquen *et al.* , 1997] .

1.2 Debris flow definition

Debris flows are natural phenomena that pose a threat to human life and which can cause considerable damage to property, infrastructure and the environment, in mountainous areas all over the world (Figure 1.1). Some of the worst catastrophes attributed to debris flow occurred in Venezuela 1999 and Columbia 1985, with more than twenty thousand people killed in each and in Taiwan 2001 with more than two hundred fatalities [Jakob & Hungr, 2005; Takahashi, 2007]. About one hundred lives a year are lost to debris flows in Japan and in China [Takahashi, 2007].



Figure 1.1. (a) Debris flow deposits from the December 1999 event in Carraballeda, coastal Venezuela. The debris flow front was estimated as 3.5 m in height, leaving 1 m boulders on second floor of a building. (b) House partially buried by the passage of a debris flow triggered by rapid snow melt in May 1983, in Slide Mountain, Nevada (USA). Both photographs by U.S. Geological Survey.

A debris flow is a rapidly moving mass of sediment, large particles, water and air that travels down a slope under the influence of gravity and can reach long run-out distance in channels with low slopes [Costa, 1984; Iverson, 1997; Johnson & Rodine, 1984]. They show a type of flow behaviour intermediate between dry rock avalanches and water floods [Iverson, 2005]. Water floods carry a relatively small sediment concentration where the main sediment movement mechanism is related with fluid mechanisms such as viscous drag, buoyancy and turbulence. Whereas, at the other end, dry rock avalanches are characterized by solid contacts. The properties of the flow depends on the water content, the sediment size distribution (from fine particles such as silts and clays to coarse particles such as sand, gravel and boulders) and

sorting [Costa, 1984].

Reports from field observations confirm that debris flow velocities depend on grain concentration and size, and on the channel's morphology and can vary from 0.5 to 20 m s⁻¹ [Takahashi, 1981]. Typical flows contain 50 to 70% solid particles by volume, with a total volume up to $\sim 10^9$ m³ [Iverson, 2009].

Interaction between particles and interaction between particles and pore fluid is considered vital to the flow evolution. Fluid particle interaction is a possible explanation for the long run-out distances and remarkable mobility sometimes seen in large debris flow events. The interstitial fluid can modify the dynamics of grain collision, facilitating the motion as a result of the reduction of the grain resistance to flow [Iverson, 1997; Iverson *et al.*, 2010; McArdell *et al.*, 2007; Takahashi, 2001].

1.3 Debris flow from initiation to deposition

A typical debris flow exhibits an initiation zone, a transportation zone and a deposition zone (Figure 1.2).

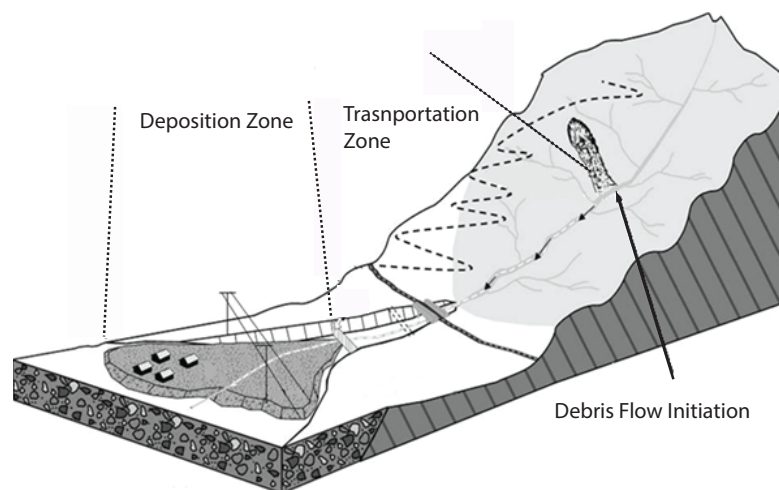


Figure 1.2. Idealized representation of a typical debris flow path (Schematic diagram from www.dnv.org).

1.3.1 Initiation

Debris flows generally form when unconsolidated sediment becomes saturated by a moisture source, in steep slopes with sparse vegetation [Ancy, 2009; Costa, 1984; Iverson, 1997]. Although vegetation generally contributes by limiting the run off and giving soil strength due to the penetrating roots of plants, debris flows have been observed in forested areas. The origin of the moisture is typically heavy rainfall. In some cases, snow melt and ice and to a lesser extent, lake outbursts or dam breaks can provide the trigger.

1.3.2 Transportation

A debris flow typically flows in pulses or surges and examples of the formation of successive waves have been observed in nature [Davies *et al.*, 1992; Jakob & Hungr, 2005; Johnson & Rodine, 1984; Takahashi, 2007], in laboratory studies on instability in suspension flow [Simpson, 1997] and in a large scale debris flow flume [Iverson, 1997; Iverson *et al.*, 2010] (Figure 1.3).



Figure 1.3. (a) Advancing surge of viscous debris flow in the Jiangjia Gully, China (Photography from Disaster Prevention Research Institute Kyoto University). Characteristic surge height $\sim 3\text{ m}$ and frontal velocity $\sim 10\text{ m s}^{-1}$. (b) Laboratory study on surge instability in custard power suspensions flowing down on 20° inclined plane.

The initial main surge is often followed by a series of smaller surges moving faster than the overall flow. The number of surges and their timing ranges from one to hundreds of successive waves with seconds to hours between them [Jakob & Hungr, 2005; Jakob *et al.*, 2005].

The formation of the surges can be the result of different mechanisms [Jakob & Hungr, 2005]. Surges characterized by boulder fronts and typically head-tail appearance can be attributed due to flow instability caused by the longitudinal sorting of debris flow material.

Another mechanics of surge appears in flows with relatively low boulder content or debris floods, where the main characteristic is the intermittency, with similar waves magnitude and time interval between surges [Takahashi, 2007]. Debris flows in the Jiangjia Gully (Figure 1.3a) in south-western China are an example of this behaviour. Similar flow instability were observed in laboratory experiments using *thixotropic* materials such as thick suspension of custard powder (Figure 1.3b), in which the fluids exhibits time dependence of the apparent viscosity (less viscous when agitated and a gelled structure over time when shear forces is not applied).

Other mechanisms for surge formation could be that the initiation of separate landslides within the same event, or a barrier obstructing the gully that collapses.

Each surge of a debris flow is characterized by three regions that evolve with time (Figure 1.4).

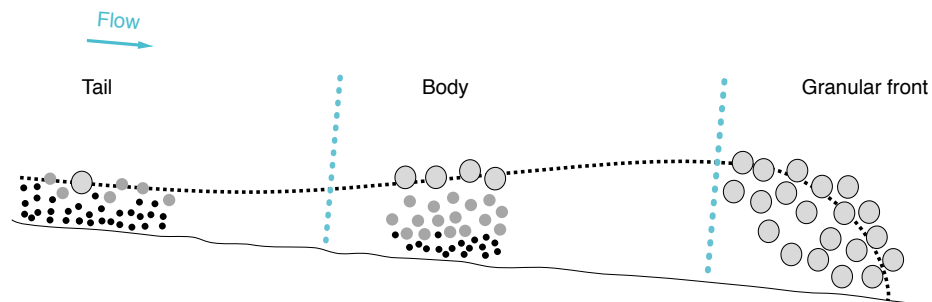


Figure 1.4. Schematic representation of the characteristic parts of a debris flow.

- *Granular front or snout.* The front of the debris flow typically contains the largest concentration of coarse boulders, pushed by the following debris suspension finer-grained material. The boulders can be up to more than 10 m in size [Takahashi, 2007], see Figure 1.5.



Figure 1.5. Large boulders were transported by the debris flows in Venezuela December 1999. Using the person standing on debris flow deposits as scale, the boulders are of order 4–5 m in diameter. Photographs by U.S. Geological Survey.

The formation of the snout is usually explained by a *size segregation* argument. Size segregation is where the large particles are pushed towards upper layers and to the front, whilst the fine grains accumulate at the bottom and in the rear part of the flow. The mechanism of size segregation, or *inverse grading*, has been frequently attributed to the dispersive pressure [Bagnold, 1954; Takahashi, 1981]. According to Bagnold [1954] theory, granular flows under shear deformation causes bulk dilation, where individual particles are moved apart of each other and pushed upwards. The exchange of momentum between the particles in neighboring layers, cause a dispersive pressure. Takahashi [1981], based on Bagnold’s theory, discussed the dependence of the dispersive forces as function of the particle size (dispersive pressure increases with the square of the particle diameter), where particles with larger diameters moves upwards faster than the smaller particles drifting downward and larger particles migrate preferentially to layers with low shear strain as the upper free surface of the flow, accumulating the larger particles in the snout.

In contrast, other literature suggest that the dispersive pressure mechanism is insufficient to explain the phenomenon of inverse grading, and considers other mechanisms as *kinematic sieving* [Branney & Kokelaar, 2002; Gray & Thornton, 2005; Iverson, 1997; Johnson *et al.* , 2012; Legros, 2002a; Middleton, 1970;

Pouliquen & Vallance, 1999]. Kinematic sieving, also known as the ‘Brazil-nut effect’, is the result of two mechanisms: percolation and squeeze expulsion. When granular materials are sheared smaller particles percolate down, falling between the large grains and squeezing the larger grains up to the free surface. The percolation phenomenon is size preferential, since small particles fall more easily and frequently between the gaps left by the big particles. Squeeze expulsion emerges from an imbalance of forces acting on individual particles, constraining movement to the vertical direction but acting on large and small particles indiscriminately, leading to size sorting of the flow through its depth. The velocities at the free surface are higher than the average flow velocity, causing that large particles migrate to the front of the flow.

Fronts dominated by big boulders have little water content due to the large void space through which the water drains to the base of the flow. The front experiences high friction due to the high concentration of big boulders. These less mobile boulders seem to hold up and store the flow core behind the snout, resulting in the boulders being pushed to the sides creating lateral levees that constrain the spreading of the flow and enhance the run-out distance [Ancey, 2012; Iverson, 1997; Johnson *et al.*, 2012; Takahashi, 2007].

- *Body*. Trailing behind the granular front or snout is the main body of the surge. The body constitutes finer liquefied debris (low-friction) that contains sand, silt and clay.
- *Tail*. The tail is a dilute turbulent flow with low solid volume fraction, similar to a muddy water flow.

1.3.3 Deposition

The time and distance to run-out depend not just on the rheologic properties of the flow but on the total volume, channel geometry and slope inclination [Ancey, 2009]. Deposition takes place along the transportation zone, in the form of lateral levees. Finally the flow spreads out at the *colluvial fan*, *debris fan* or *cone* as broad lobes. Deposition occurs as the flow decelerates due to a decrease in the slope angle,

or the flow thickness reaches a critical value as the flow spreads out by lack of confinement [Ancey, 2009; Jakob & Hungr, 2005].

1.4 Mechanical classification of debris flow

The mechanical characteristics of the flows and momentum transport processes depend on stresses due to particle-particle contact, fluid viscosity and fluid particle interactions. The particle concentration plays a crucial role in determining the momentum exchange process [Ancey *et al.*, 1999; Pudasaini & Hutter, 2007]. With a higher volume fraction of solids, the freedom of an individual particle to move through the bulk is inhibited. Deformation at high solid concentrations, where most of the particles are in direct contact, introduces a volume change due to geometrical constraints, termed dilatancy [Ancey *et al.*, 1999; Pudasaini & Hutter, 2007; Reynolds, 1885].

A simplified framework of predominant flow behaviour, from low to high solid volume fraction, distinguishes three regimes: collisional, viscous and frictional.

- (i) A *collisional regime* is characterized by high shear rates or large rapid deformations. It is referred to as the *grain-inertia regime* by Bagnold's classification [Bagnold, 1954]. At a local particle scale, instantaneous or brief contacts between particles are responsible for the major part of the momentum transport and pore fluid plays a minor role. Consequently, stresses become rate dependent. Bagnold's experiment, consisting of shearing a mixture of glycerol-water-alcohol solution and neutrally buoyant paraffin wax particles in an annular shear cell, demonstrated that for high shear rates, shear and normal stresses depend on the square of the shear rate ($\tau, \sigma \propto \dot{\gamma}^2$). In this regime, the highly agitated particles resemble the behaviour of dilute gases, described by kinetic theory [Ogawa, 1978]. The degree of agitation of the particles is measured by the ratio between kinetic energy related to the mean translational flow velocity, and the kinetic energy related to the fluctuating random velocity [Buser & Bartelt, 2009, 2011a; Campbell, 1990; Iverson, 1997; Takahashi, 2007].

- (ii) A *viscous regime* corresponds to low shear rates and low concentration of large particles where viscous effects of the interstitial fluid dominate. This behaviour is termed by Bagnold as the *macro-viscous regime*, and the shear and normal stress are linearly proportional to the shear rate ($\tau, \sigma \propto \dot{\gamma}$). The stress behaves like a Newtonian fluid with an effective viscosity.
- (iii) A *frictional regime* occurs at very high particle concentrations and low shear rates. It was considered by Savage [1984] as a *quasi-static regime*. In this type of flow the particles agglomerate and interlock moving in ‘rigid’ blocks of particles. The motion occurs slowly and particles maintain contact with near neighbours. The grain inertia forces and viscous effects are negligible. The particles endure long, sliding and rubbing contacts with surface friction and interlocking between particles the main mechanisms of momentum exchange. The shear and normal stress are rate-independent. The stress for such elastic-solid behaviour are described by Coulomb friction criterion often used in solid mechanics [Schofield & Wroth, 1968].

Three key dimensionless numbers evaluate the balances between these dissipation mechanisms collisional, frictional and viscous. These are the Savage number (the ratio of inertial grain collisions to grain contact friction stresses)

$$N_{\text{SAV}} = \frac{\dot{\gamma}^2 \rho_s d_p^2}{(\rho_s - \rho_f) g h \tan \varphi}, \quad (1.4.1)$$

the Bagnold number (the ratio of inertial grain collisions to viscous shear stress)

$$N_{\text{BAG}} = \frac{\phi}{1 - \phi} \frac{\dot{\gamma} \rho_s d_p^2}{\mu_f}, \quad (1.4.2)$$

and the friction number (the ratio of grain contact friction stresses to viscous forces)

$$N_{\text{fric}} = \frac{N_{\text{BAG}}}{N_{\text{SAV}}} = \frac{\phi}{1 - \phi} \frac{(\rho_s - \rho_f) g h \tan \varphi}{\dot{\gamma} \mu_f}, \quad (1.4.3)$$

where h is the characteristic flow height, $\dot{\gamma}$ is the shear rate estimated dividing the characteristic velocity by characteristic height ($\dot{\gamma} = u_f/h$), ρ_s the density

of the solid, ρ_f and μ_f the density and the viscosity of the interstitial fluid respectively, d_p is the particle diameter and ϕ the solid volume fraction and φ is the bulk friction angle.

Threshold values to estimate the regime are showed in Table 1.1 and examples of the parameters for different type of flows are included in Table 1.2.

Dimensionless Number	Threshold	Regime
N_{SAV}	$\gtrsim 0.1$	Collisional
	$\lesssim 0.1$	Frictional
N_{BAG}	$\gtrsim 200$	Collisional
	$\lesssim 20$	Viscous
N_{fric}	$\gtrsim 2000$	Frictional
	$\lesssim 2000$	Viscous

Table 1.1. Evaluation of flow regime according to dimensionless numbers. Savage & Hutter 1989, Iverson & Denlinger 2001, Bagnold 1954, Iverson 1997, Iverson & LaHusen 1993.

Symbol [Units]	Flow location and classification			
	USGS flume debris flow Iverson [1997]	Kamikamihorizawa debris flow Takahashi [1991]	Elm rock avalanche Hsü [1975]	Nottingham laboratory debris flow
h m	0.2	2	5	$[17-48] \times 10^{-3}$
ρ_s kg m^{-3}	2700	2700	2400	2600
ρ_f kg m^{-3}	1000	1000	2	[1.2, 1000, 1260]
ϕ	0.6	0.6	0.5	[1, 0.7, 0.6, 0.4]
d_p m	0.01	0.2	0.5	$[2, 4, 8] \times 10^{-3}$
$\dot{\gamma}$ s^{-1}	50	3	5	[1-72]
μ_f Pa s	0.01	0.1	2×10^{-5}	$[1.83 \times 10^{-5}, 8.9 \times 10^{-4}, 0.8]$
N_{SAV}	0.2	0.03	0.1	$[3 \times 10^{-4} - 1.9]$
N_{BAG}	6×10^3	1×10^4	4×10^8	$[0.1 - 2 \times 10^9]$
N_{fric}	3×10^4	3×10^5	4×10^9	$[0.1 - 9 \times 10^9]$

Physical parameters values from Iverson & Vallance [2001].

Table 1.2. Estimation of dimensionless numbers to characterize the flow regime in well-documented flows.

Field investigations and experimental laboratory work suggest that within a

single debris flow event regimes can coexist and transition from one regime to another is commonly seen between initiation and deposition. Thus flow rheology is a function of time and position. Understanding of debris flow behaviour from initiation to deposition is crucial to be able to predict potential debris flow activities for the development of hazard zonation mapping to protect life and infrastructure. These mechanisms can be better understood by modelling these phenomena mathematically or physically.

1.5 Mathematical modelling of debris flows

Numerical models are used to study the dynamics of debris flows and they are an essential tool in assessing hazard and designing mitigation measures against debris flow and related phenomena. The numerical models require to know the constitutive equation of the flow, which is estimated by assuming a type of rheology.

1.5.1 Continuum models

To date most of the mathematical numerical models are based on continuum conservation laws of mass and momentum.

The governing equations describing mass conservation for a debris flow mixture treated as a continuum (e.g. Gidaspow, 1994) can be expressed by

$$\frac{\partial \rho}{\partial t} + \nabla \cdot \rho \mathbf{u} = 0 \quad (1.5.4a)$$

$$\frac{1}{\rho} \frac{d\rho}{dt} + \nabla \cdot \mathbf{u} = 0, \quad (1.5.4b)$$

and the conservation of linear momentum can be written

$$\frac{\partial \rho \mathbf{u}}{\partial t} + \nabla \cdot \rho \mathbf{u} \mathbf{u} = -\nabla \cdot \mathbf{T} + \rho \mathbf{g} \quad (1.5.5a)$$

$$\frac{D\mathbf{u}}{Dt} = -\frac{1}{\rho} \nabla \cdot \mathbf{T} + \mathbf{g}, \quad (1.5.5b)$$

where ρ is the mass density, $\mathbf{u} = (u_x, u_y, u_z)$ the velocity vector ($\mathbf{u} \mathbf{u}$ is a dyadic product), \mathbf{T} the stress tensor and \mathbf{g} the gravitational acceleration. The material

derivative $D/Dt = \partial/\partial t + \mathbf{u} \cdot \nabla$ represents differentiation in a frame of reference which is moving with the flow velocity \mathbf{u} .

In debris flows typical thicknesses are small compared to the overall extent of the flow. The shallowness parameter ϵ defined as the ratio between characteristic height and length scales is small ($\epsilon \ll 1$). Therefore shallow flow approximations are generally used to derive tractable equations. A shallow flow approximation can be applied by depth averaging the equation of motion through the debris flow thickness from the base of the flow at $z = 0$ to the free surface at $z = H$. Neglecting erosion and deposition processes which implies that there is no mass entering or leaving at the free surface or at the base of the flow, the boundary conditions may be written as:

$$u_z(z = H) = \frac{DH}{Dt} = \frac{\partial H}{\partial t} + u_x(H) \frac{\partial H}{\partial x} + u_y(H) \frac{\partial H}{\partial y}, \quad (1.5.6)$$

$$u_z(H = 0) = 0, \quad (1.5.7)$$

where H is a function of x , y and t .

A constitutive relation which describe how the flow deforms under shear and closes the set of governing equations is still unclear.

One approach is to consider the fluid as homogeneous with an apparent Non-Newtonian rheological relation between the shear stress and strain rate. Fluid rheologies often encountered are:

(i) *Viscoplastic fluid*

The viscoplastic theoretical framework models the mixture with a finite yield strength. One of the most frequently used viscoplastic model is the *Bingham fluid* model [Johnson & Rodine, 1984; Johnson, 1965, 1970; Yano & Daido, 1965] which is both simple and can explain some debris flow features. For example, a Bingham rheology allows for the formation of a ‘plug’ (Figure 1.6) and captures the bulk flow behaviour for muddy slurry flows (i.e. well-sorted fine-grained matrix). A Bingham fluid moves as a plug up to a finite shear strength, τ_o , and once that critical yield strength is exceeded, the material flows as a Newtonian fluid.

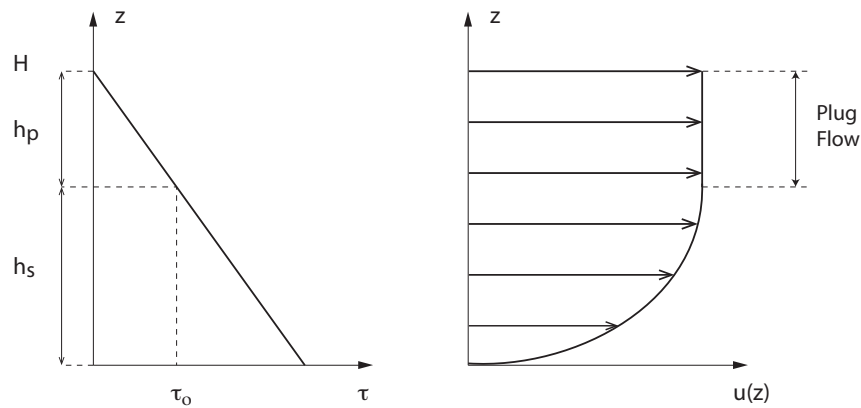


Figure 1.6. Formation of a ‘plug’ in the upper layer h_p , where the shear stress τ is smaller than the yield stress τ_o and the velocity is constant. In the lower layer h_s , the velocity increases with the height above the bed due to shearing.

The constitutive equation is given by

$$\tau = \tau_o + \mu_B \dot{\gamma}, \quad (1.5.8)$$

where τ is the applied shear, μ_B is the Bingham fluid viscosity coefficient and $\dot{\gamma} = du/dz$ the strain rate (velocity gradient).

In order to apply the Bingham-type fluid model the parameters τ_o (yield stress) and μ_B (Bingham viscosity) must be measured from samples collected from the field. However, the poor prior knowledge of a debris flow composition, particularly the relatively unknown effect of very large boulders, can make these measurements difficult [Takahashi, 2007].

The yield stress can be modelled by a Mohr-Coulomb failure criteria $\tau_C = \tan\varphi \sigma = \mu \sigma$ for the yielding shear strength [Johnson & Rodine, 1984; Johnson, 1970]

$$\tau = \mu \sigma + \mu_B \dot{\gamma}, \quad (1.5.9)$$

where φ is the internal friction angle, μ the effective friction coefficient φ is the bulk friction angle. It is referred to as the *Coulomb-viscous model*. At low stress the material remains ‘rigid’ (as an elastic solid) unless the stresses exceed the plastic yield strength (Coulomb friction dependence), and then the material flows like a viscous fluid with strain rate dependence.

The *Herschel-Bulkely model* captures the effects of yield stress and the apparent viscosity decrease with increasing shear rate, which occurs in water-clay-grain mixtures, termed as ‘shear thinning’ [Coussot, 1995; Coussot *et al.*, 1998; Major & Pierson, 1992] :

$$\tau = \tau_o + K_{HB} \dot{\gamma}^n, \quad n \leq 1 \quad (1.5.10)$$

with parameter K_{HB} , consistency, and n , index. If $n = 1$, the Bingham fluid case is recovered. If $n = 2 > 1$, the apparent viscosity increases with the shear rate, termed ‘shear thickening’, and ‘dilatant fluid’ model is obtained (discussed below).

The Herschel-Bulkey-type model is more general, but increases the number of parameters to be measured or calibrated, making predictive use more difficult.

Many investigators have treated and modelled debris flows by using viscoplastic rheological flows [Bisantino *et al.*, 2010; Costa, 1984; Coussot & Meunier, 1996; Johnson & Rodine, 1984; Kaitna *et al.*, 2007; Major & Pierson, 1992; Naef *et al.*, 2006; Phillips & Davies, 1991; Pudasaini, 2011; Rickenmann *et al.*, 2006].

The most significant limitations of the viscoplastic models is that particle-particle interactions remain unaccounted for.

(ii) *Dilatant-type fluid*

In contrast, Takahashi [1981] developed an inertial grain flow model of debris flows, where grain collisions dominate the flow behaviour. The inertial grain flow model, in which particle interactions are considered, is based on the work of Bagnold [1954], corresponding to the collisional regime described in Section 1.4. The proposed relation was $\tau \propto \dot{\gamma}^2$ (‘shear thickening’).

Realistic debris flow velocity profiles can be obtained by using Takahashi’s theory and the dispersive stress can explain snout formation and inverse grading of debris flow deposits, only for a type of debris, which exhibits a velocity profile with a concave upward shape [Iverson & Denlinger, 1987]. However, it

cannot explain the apparently ‘rigid’ plug formation. This theory describes only the solid phase assuming that grains are uniformly dispersed in the flow. Thus excess pressure in the pore fluid is ignored, contradicting field observations where fronts carry coarser boulders followed by fluid tails that support pore pressure [Iverson, 1997].

(iii) *Voellmy fluid*

Voellmy fluids are modelled using a Voellmy-Salm friction relation [Salm, 1993], which considers two friction parameters τ_C , a dry Coulomb-type contribution, and τ_V a turbulent (Chézy-type) contribution

$$\tau = \tau_C + \tau_V = \mu f(\sigma) + \frac{f(u^2)}{\xi}. \quad (1.5.11)$$

The dry-Coulomb parameter is a velocity-independent term, proportional to the basal normal stress (with friction coefficient μ). This term is dominant when the flow is slow and controls the run-out phase. Whereas the Chézy parameter is dependent on the square of the velocity (friction coefficient ξ) and dominates the flow when moving rapidly.

The Voellmy model has been used to simulate debris flows [Deubelbeiss & Graf, 2013; Graf & McArdell, 2009; Hürlimann *et al.*, 2003; Medina *et al.*, 2008; Naef *et al.*, 2006; Rickenmann *et al.*, 2006; Scheuner *et al.*, 2011], to reproduce flow paths and depositional patterns after being calibrated with data from previous events.

1.5.2 Multi-phase models

Multi-phase models account explicitly for solid and fluid interactions. Relatively new research has been done to develop two-phase models that reflect variation within the fluid-particle mixture composition, considering bulk properties and homogeneous distribution [Berzi & Jenkins, 2009; Iverson, 1997; Iverson & Denlinger, 2001; Pudasaini *et al.*, 2005] where the volume fraction was constant. Pitman & Le [2005] proposed a two-fluid model allowing the volume fraction to vary in the streamwise

direction, however the relative motion and interaction between fluid and particles was not considered.

These depth-averaged debris flow models miss some key physical aspects, concerning the vertical structure of the flow. The influence of the internal flow motion and vertical density stratification are not considered in the models. More recent work [Kowalski & McElwaine, 2013; Pudasaini, 2012] introduce a generalization of the theory by Savage & Hutter [1989] of two-phase model and an extension of the two-fluid debris flow model of Pitman & Le [2005], by accounting for vertical rearrangements of both components. In this way, the model can describe the variation of the debris flows dynamics from the formation of granular front to the fluidized tail.

Although pore fluid pressure is considered in the models, explanations for the pressure distribution remain a challenge. Further investigation is required to explain the mechanism responsible for the mobility of fluid-solid mixtures.

1.6 Physical modelling of debris flows

1.6.1 Field measurements and large-scale debris flows

Field measurements of debris flow are crucial for the validation and verification of models, since no scaling assumptions are necessary. However, measurements from debris flows in the field are scarce due to the lack of predictability and the difficult access to the event sites. They often strike without warning and field monitoring is difficult due to the harsh environmental conditions and the high velocity of the flow. In addition, field experiments are uncontrollable, so that material properties, initial and boundary conditions are difficult to define.

Despite these difficulties, two catchments have developed in Switzerland (Figure 1.7). Dorfbach Randa with two main stations which measure flow velocity and flow height (e.g. Deubelbeiss & Graf, 2013). Illgraben catchment is instrumented with devices to measure not only front velocity and flow depth, but also a force plate on the bed of the channel for normal and shear stress and pore fluid pressure (e.g. McArdell *et al.*, 2007).

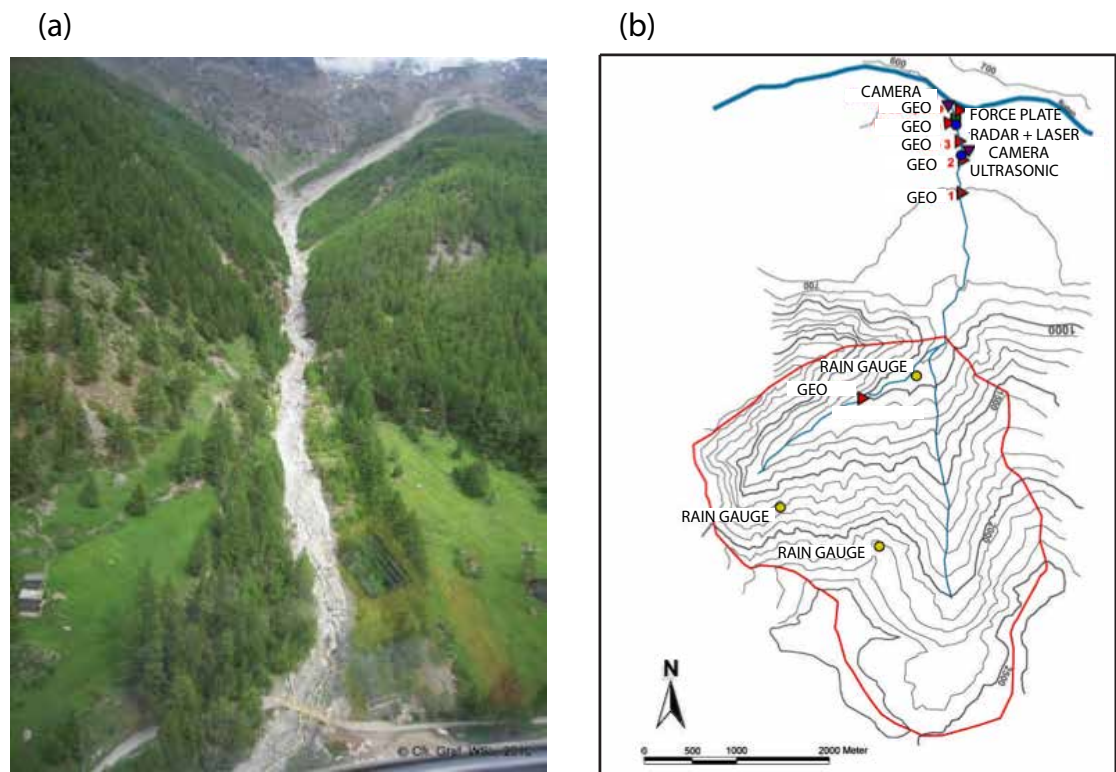


Figure 1.7. (a) Debris flow catchment at Dorbach Randa in the Matter Valley, Switzerland. (b) Topographical map of Illgraben showing the distribution of the instrument devices. Debris flows in a northerly direction in this catchment. Courtesy of WSL (Swiss Federal Institute for Forest, Snow and Landscape Research).

Controlled experiments on debris flows at large scale are conducted at the USGS debris flow flume (95 m long, 2 m wide, 1.2 m deep and 31° inclination, Figure 1.8) provide good dynamic similarity [Iverson *et al.*, 2010] (see Table 1.2). The flume design allows investigation of the whole the debris-flow process, from initiation through to deposition, with well controlled boundary and initial conditions. However, conducting the experiments and instrumenting the flume are highly cost-intensive and time consuming.



Figure 1.8. Debris flow descending the U.S. Geological Survey debris flume. Debris flow material of $\sim 10\text{ m}^3$ down a 95 m flume of 31° incline.

1.6.2 Small-scale debris flows

Despite the scaling conflicts in laboratory experiments [Iverson & Denlinger, 2001; Iverson *et al.*, 2010], they have significant advantage to understand the flow behaviour and provide repeatable data with well-defined boundary and initial conditions. Not only is this useful for validating and calibrating numerical debris flow models [Davies *et al.*, 2010; Hutter, 2005; Sanvitale, 2010], but by carefully selecting which similarity criteria to respect, a physical picture of the flow properties can be developed.

The main features of complex systems can be understood by analysing simpler systems. The individual parameters can be isolated to study the behaviour when modifying other controlled parameters [Dalziel, 2012].

Moving bed channels or re-circulating flumes allow fully developed flows to be generated within short channels. For these small volumes of mixtures are required and narrow channels due to the small effect of wall friction. Davies [1990] used a moving bed flume to study debris waves behaviour, finding qualitative similarities

between the field and laboratory results. Armanini *et al.* [2005] studied the rheological behaviour of high concentration granular-liquid mixtures with and without loose material at the base using a re-circulation flume. Kaitna & Rickenmann [2007] studied the rheologic flow behaviour of stationary surges of a diversity of mixtures using a vertically rotating drum.

Erosion and entrainment mechanisms in debris flows have been analysed using geotechnical centrifuges [Bowman *et al.* , 2010], altering gravitational acceleration to replicate the high shear rate processes within the flows.

1.7 Summary

The fast rate of tourism and housing development, accelerates the need to build in hazardous areas, such as colluvial fans. Along with landscape instability, as glaciers retreat and permafrost melts in response to general climate change [Davies *et al.* , 2010; Harris *et al.* , 2003; WGMS, 2013]. These factors are increasing debris flow hazards. Modelling such events accurately is timely as altering climatic conditions bring the applicability of historical data accounts to future event into question.

Different approaches have been applied and a wide variation of models have been developed. However, the debris flow process is still poorly understood and realistic predictive models remain incomplete [Ancy *et al.* , 1999; Armanini *et al.* , 2005; Iverson, 1997, 2012; Iverson *et al.* , 2010; Kaitna & Rickenmann, 2007; McArdell *et al.* , 2007; Pudasaini, 2012; Rondon *et al.* , 2011; Takahashi, 2007].

Fluid pore pressure is thought to be responsible for evolving rheological behaviours, from high grain-contact friction in unliquefied parts to low friction in liquefied portions. However, this mechanism is still relatively little explored.

An improved understanding of the factors that determine pore pressure is thus essential for significant progress in debris flow modelling. This work aims to address this need by undertaking laboratory experiments exploring this phenomenon.

1.8 Structure of the thesis

This thesis is divided in six chapters. Chapter 1 introduced the main characteristics and mechanical classification of debris flows and addressed the need for reliable models to estimate the hazardous areas and prediction of the dynamics of the debris flows. An introduction to the mathematical and physical model approaches was presented. Chapter 2 provides a detailed description of the design of the flume, experimental set up and selection of the materials. The measurement methods and data analysis such as image analysis and PIV are outlined. The characteristic front flow position and flow height are defined. Chapter 3 presents the morphological characteristics of the present laboratory-scale debris flows under the influence of particle size, roughness element diameter, interstitial fluid viscosity and solid volume fraction. Definition of non-fluctuating region and the intermittent collisional region are provided. In Chapter 4 the main dynamic characteristics of the laboratory-scale debris such as pressure, normal and shear stress measurements at the basal surface and velocity profiles through the flow depth from nose to tail were discussed. Chapter 5, a numerical simulation model RAMMS (RAPid Mass Movements Simulation) is presented. The validation of the prediction of the model is applied for dry laboratory-scale mixtures. Finally, Chapter 6 includes the conclusion of the present work.

Chapter 2

Flume experiments

The aim of this work is to visualize the dynamic morphology of fluid-particle mixtures and measure key flow parameters. This chapter introduces an experiment designed to do this investigating flows both dry glass beads and mixtures with water or glycerol, released from behind a lock gate to flow down an inclined flume.

The design of the experiment, the measurements methods and data analysis techniques are introduced in this chapter.

2.1 Laboratory modelling design

The purpose of the present laboratory experiments is to gain a better understanding of how fluid-particle interaction leads to morphological features, such as snout-body architecture, deposition and particle segregation effects, and to study the role of fluid pore pressure and basal stresses in determining rheology.

This simplified laboratory model design seeks to study the flow morphology and dynamics by isolating and controlling parameters such as the particle sizes, the roughness element diameter, the viscosity of the interstitial fluid and the solid volume fraction. In contrast with previous experiments, we ignore the finest particles found in debris flows, and simulate their effect by changing the viscosity of the interstitial fluid. The particles we use are large enough to maintain a relatively high particle Reynolds numbers (discussed below) to replicate the fluid-particle interaction of large-scale flows. The physical properties of the materials are summarized in

Table 2.1.

Parameter	Symbol	Values	[units]
Solid: glass beads			
Density	ρ_p	2600	kg m ⁻³
Diameter	$[d_{p1}, d_{p2}, d_{p3}]$	$[2, 4, 8] \times 10^{-3}$	m
Internal friction angle ^a	$[\varphi_1, \varphi_2, \varphi_3]$	$[23^\circ, 24^\circ, 22^\circ]$	
Fluid: air, water, glycerol			
Density	$[\rho_{f1}, \rho_{f2}, \rho_{f3}]$	$[1.2, 1000, 1260]$	kg m ⁻³
Viscosity	$[\mu_{f1}, \mu_{f2}, \mu_{f3}]$	$[1.83 \times 10^{-5}, 8.9 \times 10^{-4}, 0.8]$	Pa s
Mixture			
Solid volume fraction	$[\phi_1, \phi_2, \phi_3, \phi_4]$	$[1, 0.7, 0.6, 0.4]$	
Volume of solids	$\phi_i V, i=[1,2,3,4]$	1×10^{-3}	m ³
Fluid volume	$(1 - \phi_i) V, i=[1,2,3,4]$	$[0.43, 0.67, 1.5] \times 10^{-3}$	m ³
Roughness surface			
Element diameter	$[d_{r1}, d_{r2}, d_{r3}, d_{r4}]$	$[0, 2, 4, 8] \times 10^{-3}$	m

Table 2.1. Physical properties of the materials used in all set of experiments, where V is the total volume of mixture.

^aThe internal friction angle measures the strength of the bulk granular material due to the friction between individual particles and the geometrical interlock of the particles [Daerr, 2001; Schaaf & Carrasco-Núñez, 2010]. The angle of internal friction was measured by the angle of repose, by pouring the dry glass beads of each size into a conical pile and measuring the maximum angle that allow the pile to remain stable.

Field debris flows also exhibit erosion and deposition of particles, contributing to the evolution in time and space of the vertical distribution of the mixture components. However in this work, erosion and deposition processes will not be addressed, providing boundary conditions that are well defined and well controlled.

The model design is based on Froude and particle Reynolds number scaling similarity to achieve dynamic similarity with full-scale debris flows.

The Froude number

$$\text{Fr} = \frac{v_f}{\sqrt{gh \cos \theta}}, \quad (2.1.1)$$

is the ratio of inertial and gravitational forces of the flow where u_f and h are the characteristics front surge velocity and fluid depth of the non-fluctuating region (see Section 2.4) respectively, g the acceleration due to gravity, and θ the slope angle. Equality in Froude number in the laboratory experiments and full-scale will ensure

that gravity forces are correctly scaled. Field estimations and measurements of debris flows showed that the majority have Froude numbers $Fr < 3$ [Hübl *et al.* , 2009]. Despite the large number of control parameters tested in the present work, the flows achieved Froude number in the range $0 < Fr < 3.5$ (Table 2.2), complying with field debris flows similarity. Flows with $Fr > 1$ are super-critical. While flows with $Fr < 1$ are sub-critical, corresponding to flows with high volume fraction and high viscosity interstitial fluid (i.e. 0.7 and glycerol respectively).

The particle Reynolds numbers Re_p is defined as

$$Re_p = \frac{\rho_f u d_p}{\mu_f}, \quad (2.1.2)$$

the ratio of the form drag and viscous forces of a particle of diameter d_p , moving with a speed u through a fluid of density ρ_f and dynamic viscosity μ_f . A very low $Re_p \ll 10$ indicates that the drag force exerted on the particles by the interstitial fluid is dominated by viscous forces. With $Re_p \gtrsim 10^3$ viscous drag forces have relatively minor importance compared to the form drag of the particle, and the fluid-particle interaction can be described as turbulent.

The particle size was chosen to obtain a sufficiently high Re_p , to achieve as turbulent interaction as possible. Equality in particle Reynolds number in the laboratory and full scale will ensure that viscous forces are correctly scaled. Flows consisting of particles mixed in water with solid volume fraction 0.4 and 0.6 (Table 2.2) achieve $Re_p > 1000$ and therefore the viscous forces should play minor role. However, when flow mixtures contains glycerol or air as interstitial fluid the Re_p are lower than ≈ 500 . Therefore, for these flows viscous forces between particles and the interstitial fluid become increasingly important. A typical particle Reynolds number range of field measurements is $2 \times 10^2 < Re_p < 10^4$ (values calculated from Iverson [1997] data).

Interstitial fluid	Roughness $d_r \times 10^{-3}$ [m]	Particle size $d_p \times 10^{-3}$ [m]	Solids vol. fraction ϕ	Fr	Re _p
Dry	8	2	1	2.2	150
Dry	8	4	1	2.0	290
Dry	8	8	1	1.8	560
Dry	8	[2,4,8]	1	2.1	270
Water	8	2	0.4	2.0	2400
Water	8	4	0.4	2.2	5400
Water	8	8	0.4	2.0	11000
Water	8	[2,4,8]	0.4	1.9	4900
Water	8	2	0.6	1.3	1600
Water	8	4	0.6	1.9	4300
Water	8	8	0.6	1.8	9300
Water	8	[2,4,8]	0.6	1.9	4700
Water	4	2	0.6	1.3	1400
Water	4	4	0.6	2.2	4700
Water	4	8	0.6	2.3	11000
Water	4	[2,4,8]	0.6	1.9	4400
Water	2	2	0.6	2.5	2300
Water	2	4	0.6	2.6	5000
Water	2	8	0.6	2.5	12000
Water	2	[2,4,8]	0.6	2.7	5300
Water	0	2	0.6	3.1	2700
Water	0	4	0.6	2.9	5600
Water	0	8	0.6	2.3	10000
Water	0	[2,4,8]	0.6	3.3	6100
Water	8	2	0.7	0.2	220
Water	8	4	0.7	1.5	3600
Glycerol	8	2	0.4	1.6	3
Glycerol	8	4	0.4	1.4	5
Glycerol	8	8	0.4	1.7	13
Glycerol	8	[2,4,8]	0.4	1.8	7
Glycerol	8	2	0.6	0.2	0.4
Glycerol	8	4	0.6	0.5	2
Glycerol	8	8	0.6	1.7	12
Glycerol	8	[2,4,8]	0.6	0.5	2
Glycerol	8	2	0.7	0.1	0.2
Glycerol	8	4	0.7	0.1	0.3

Table 2.2. Estimation of Froude, Fr, and particle Reynold Re_p numbers for varying interstitial fluids, solid volume fraction, particle size varies and roughness element diameter.

2.2 Experimental set up

The laboratory experiments were conducted in a flume 156×10^{-3} m wide and 230×10^{-3} m deep, with a flow travel distance of 700×10^{-3} m over a fixed bed of variable roughness on an angle inclined plane of 27° to the horizontal (Figure 2.1). The appropriate working section in the flume of length 700×10^{-3} m was adopted to ensure that all flows reached the sensor location. The flume slope of 27° was chosen to study the flow of realistic debris flows, since most of the debris flows require a steep slope greater than 15° – 20° [Costa, 1984] with typical slope angles between 20° – 45° [Hung *et al.*, 2001], and steep enough for the mixtures to flow.

The end of the flume was connected via a curved fillet to a smooth, horizontal run-out tray.

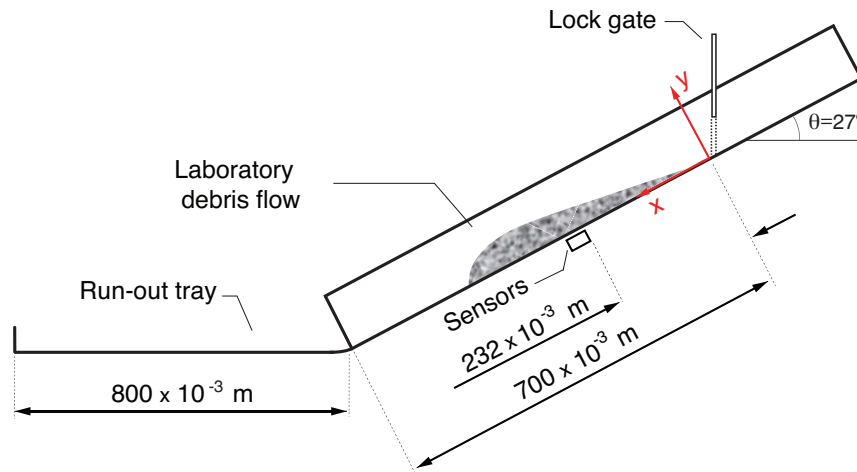


Figure 2.1. Schematic illustration of the flume with a lock gate and run-out tray.

The top part of the flume was fitted with a vertical lock gate which contained the mixture in a wedge-shaped space, as shown Figure 2.2. The gate was originally designed to be removed in a direction perpendicular to the inclined base of the flume. However, when the flow initially slumped after release, it created a wave roll trapping a considerable amount of air. This issue was eliminated with a vertical lock gate. The lock gate trap could be rapidly opened manually to release the mixture. In all the experiments, the mixtures were released from rest, with initially loose packing. The outward facing walls of the flow flume are made of clear glass to allow the observation of the propagation of the flow using a high-speed camera operating

at 700 Hz.

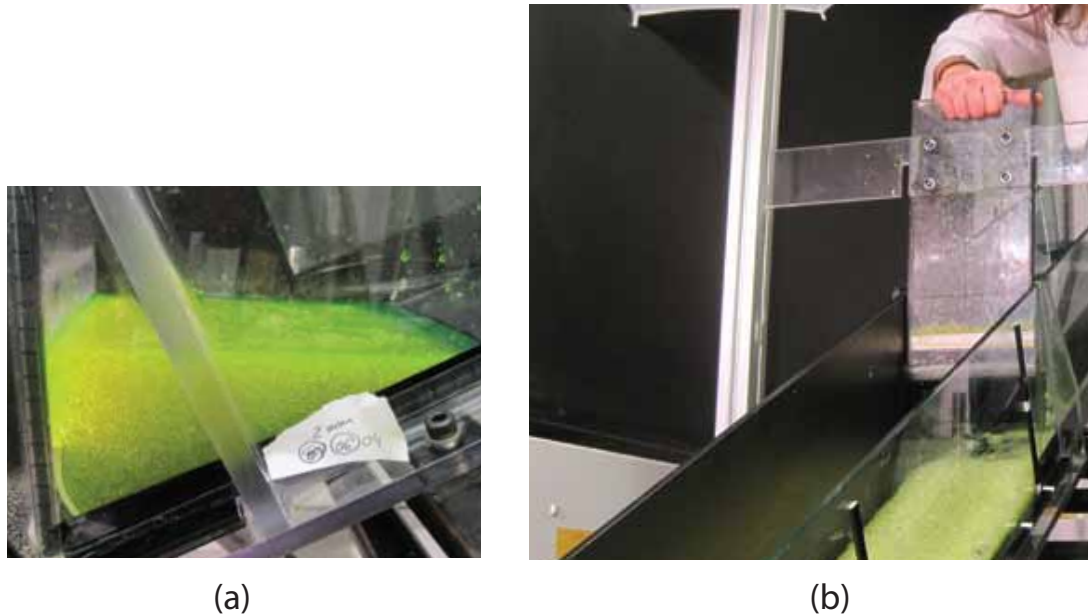


Figure 2.2. Photographs of the lock gate (a) before release of a mixture of glass beads of 2×10^{-3} m in water with a solid volume fractions 0.6 and (b) after releasing the mixture.

The flume bed had a changeable surface with varying roughness generated by gluing glass beads to the surface and painted black. The roughness element diameter varied from $d_r = 0$ (smooth surface with no adhered beads), 2×10^{-3} , 4×10^{-3} and 8×10^{-3} m (Figure 2.3). The bottom of the flume was designed with an opening at the location of an assembly of sensors for easy access and mounting (Figure 2.4).

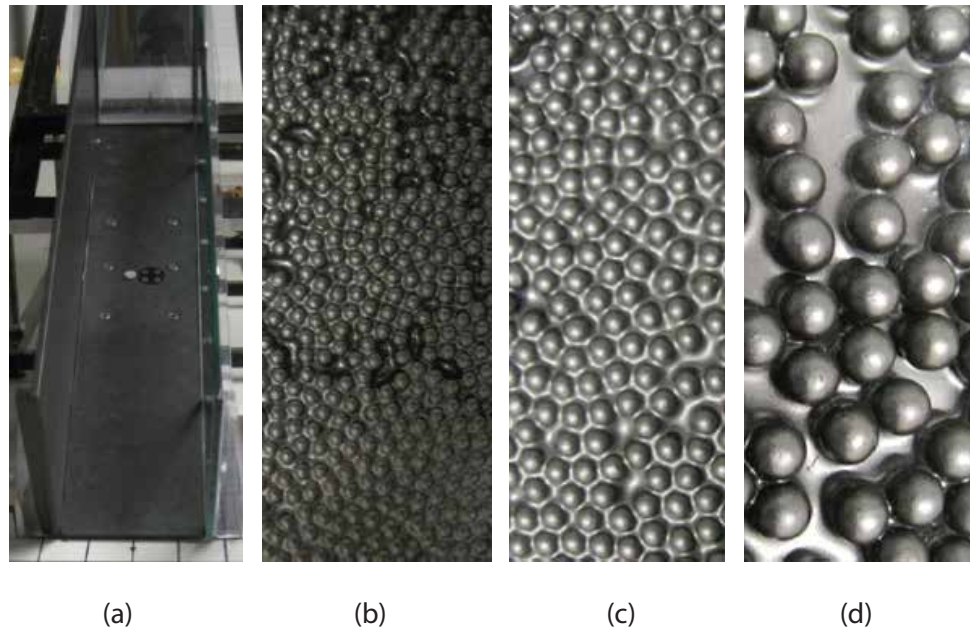


Figure 2.3. Flume bed surface with different roughness element diameter (a) $d_{r1} = 0$ m, (b) $d_{r2} = 2 \times 10^{-3}$ m, (c) $d_{r3} = 4 \times 10^{-3}$ m and (d) $d_{r4} = 8 \times 10^{-3}$ m.

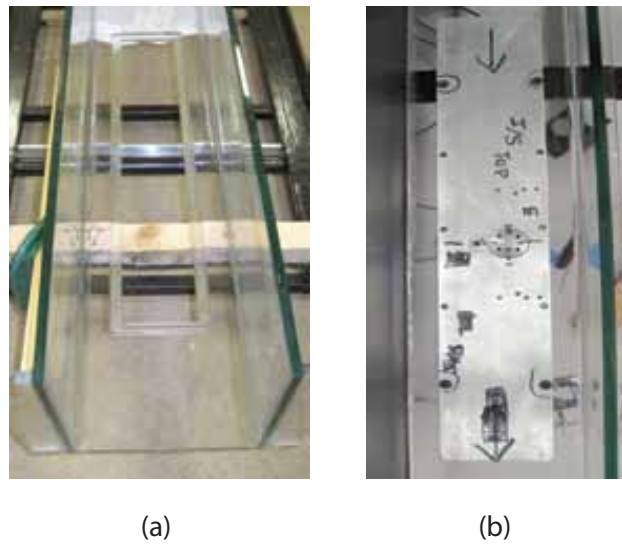


Figure 2.4. (a) Opening in the base of the flume to locate the metal plate which holds the sensors for easy assembly. (b) Metal plate with the sensors..

2.2.1 Flow mixtures

The granular material used to generate the laboratory debris flows were spherical glass beads made of soda lime glass supplied by Worf Glaskuglen. The part numbers are 1020102, 1060102 and 1130102 for 2×10^{-3} , 4×10^{-3} and 8×10^{-3} m respectively. In this way the properties of the granular material such as particle size, composition, sphericity and mechanical properties are well defined compared with natural granular material such as mixtures of sand or gravel. The total solid volume of $1 \times 10^{-3} \text{ m}^3$ was held constant in all tests, varying the solid volume fraction by adding fluid (water or glycerol).

chemical composition

The mixtures were manually mixed, which could lead to the formation of bubbles, especially flows with glycerol. After mixing, the mixture was poured behind the lock-gate where it was left for 2-3 minutes to settle the particles and allow the air bubbles to escape.

2.3 Measurements Methods

2.3.1 Sensors

Temporal evolution of normal and shear stresses and pore fluid pressure at the base of the flow were measured. The sensors were mounted in the base of the flume at 232×10^{-3} m from the lock gate (Figure 2.1) away from the flume walls (Figure 2.5). Sensor location was fixed for all tests, meaning that while most of the flows were fully developed at their location, some (glycerol-based) flows were already depositing and decelerating at the sensors position.

Basal pore fluid pressure was measured with a Validyne (Model DP15) wet/dry differential pressure transducer with a range of 0 to 2.2 kPa ($\pm 5.5 \times 10^{-3}$ kPa accuracy, including effects of non-linearity, hysteresis and non-repeatability) and rigid mounted with the diaphragm in the vertical plane. The transducer was used for a gauge pressure measurement with one port open to the atmosphere and the other port connected to a tube of 8×10^{-3} m diameter mounted in the flume base.

This part was covered with a metal grid preventing particles from entering (Figures 2.5a and 2.5b,c). The connection length to the base of the flume was minimised ($\approx 30 \times 10^{-3} \text{ m}$) to achieve the fastest possible frequency response of the transducers. This tube was refilled each test with same interstitial fluid as in the tested mixture to maintain the pore fluid a level at initiation. The transducer was also bled to release entrapped air before each test.

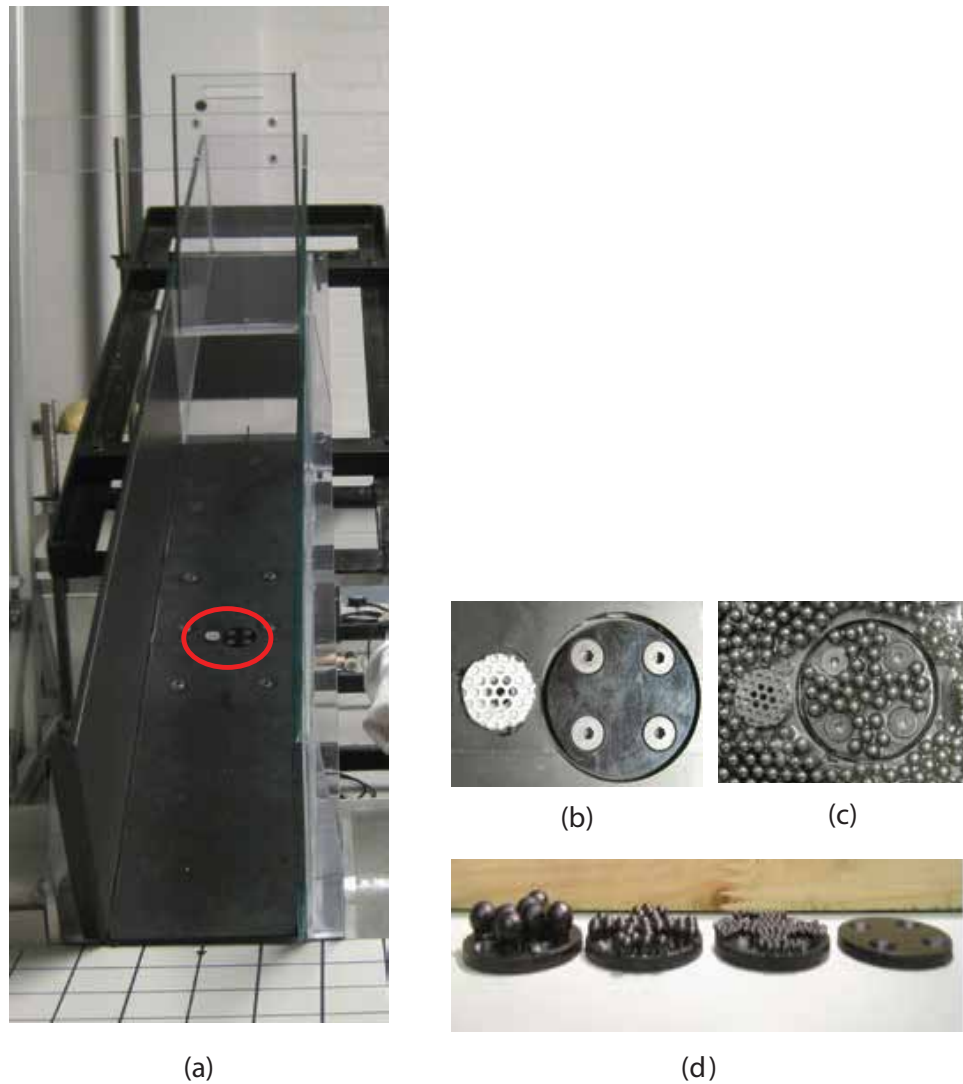


Figure 2.5. (a) Top front view of the flume showing the sensor location (highlighted with a circle) with a 0 m roughness element surface. (b) Zoom in of the pore pressure sensor (left) covered with a metal grid and the force plate (right) with a 0 m and (c) $4 \times 10^{-3} \text{ m}$ roughness element diameter cover. (d) Interchangeable circular plates to cover the force plate to match the corresponding roughness element diameter of the base; from left to right 8×10^{-3} , 4×10^{-3} , 2×10^{-3} and 0 m roughness element diameter.

The differential pressure transducer was calibrated using hydrostatic water pressures. The output electrical signal E of an applied pressure P may be modelled as:

$$E = E_o + kP, \quad (2.3.3)$$

where E_o is the offset and k provides the voltage per unit of pressure. The calibrations showed both linearity (a linear best fit line correlated with the data with $R^2 > 0.997$ for a total number of $n_1 = 39$ observations) and reproducibility (Figure 2.6). The *coefficient of determination* R^2 , which measures the adequacy of the fitted line, was calculated

$$R^2 = 1 - \frac{\sum_{i=1}^{n_1} (E_i - \hat{E}_i)^2}{\sum_{i=1}^{n_1} (E_i - \bar{E})^2}, \quad (2.3.4)$$

where E_i is the individual electrical signal response at observation i , \bar{E} the mean value of E_i of n_1 observations and \hat{E}_i the value of E estimated from the model for observation i . The coefficient R^2 varies $0 \leq R^2 \leq 1$, where $R^2 = 1$ is a perfect fit and $R^2=0$ means there is not linear relationship, (e.g. Mason *et al.*, 2003; Reddy, 2011).

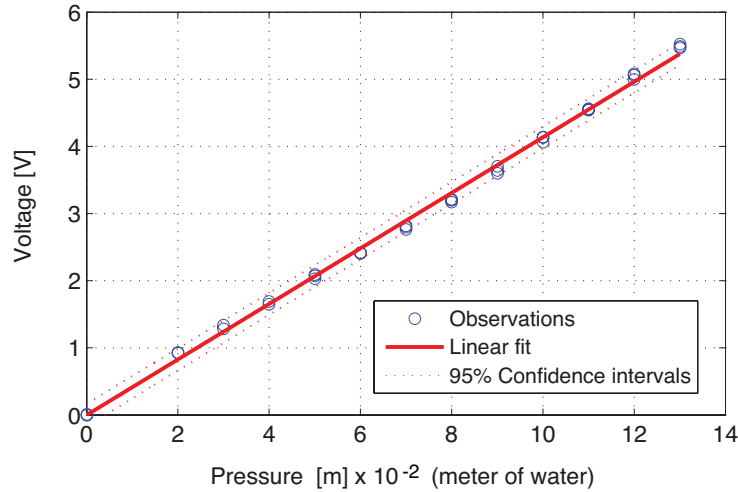


Figure 2.6. Calibration curve of the differential pressure transducer. The voltage output from the sensor is converted to pressure using linear regression with a coefficient of determination $R^2 > 0.997$. The dashed lines delineate the 95% confidence intervals.

The pressure transducer did not show coefficients of offset drift during the calibration with a value $0.01 \pm 50\%$, being 50% the normalised standard error of the

mean zero offset. The total amount of observations were $n_2 = 3$. The normalised standard error of the mean was calculated as

$$\left(\frac{SD}{\sqrt{n_2}} \right) \frac{1}{\bar{E}_o}, \quad (2.3.5)$$

where SD is the population standard deviation

$$SD = \left(\frac{\sum_i^{n_2} (E_{oi} - \bar{E}_o)^2}{n_2 - 1} \right)^{1/2}, \quad (2.3.6)$$

E_{oi} the individual reading and \bar{E}_o the mean value of E_{oi} of the set of n_2 values.

During the experiments, the zero offset was determined by using the recorded measurements before the flow reaches the pore fluid sensor.

Basal normal and shear stress measurements were made with a Klister 3-component force plate (Model 9317B). The sensor measures compression and tensile forces in a range -1000 – 1000 N for shear force component and -2000 – 2000 N for the normal force. The force plate was sealed with a gasket consisting of a watertight membrane to avoid fluid leakage into the sensor (Figure 2.7). $36 \times 10^{-6} \text{ m}^2$ circular plate with the same roughness element diameter as that for the flume surface (Figure 2.5b-d) was mounted on the force plate. The gap between the circular plate and the flume base was minimised ($< 2 \times 10^{-3} \text{ m}$) to avoid small particles becoming jammed. However, it was found in some tests that fragments of broken glass beads jammed the gap preventing the force plate from operating correctly.

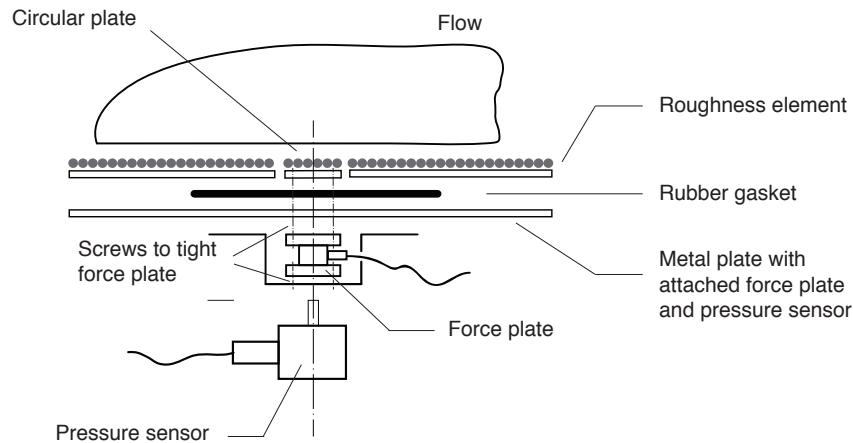


Figure 2.7. Assembly view sketch of the sensors located beneath the flume.

The force plate was calibrated using static calibrated weights, with the flume in both horizontal (only normal force) and 27° angle (normal and shear force). This required a system by which the weights were hold in place when the chute was inclined. It consisted of a peg fixed to a circle base which was fitted to the force plate. Calibrated doughnut weights were mounted on the peg (Figure 2.8).

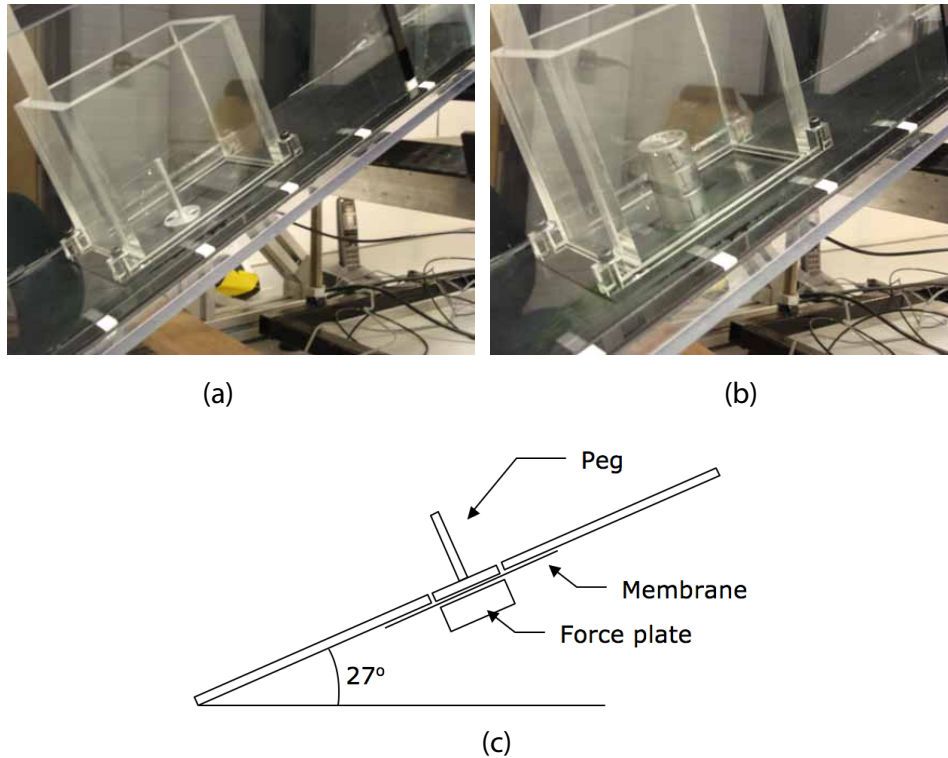


Figure 2.8. Calibration system (a) without weights and (b) with the calibrated weights. (c) Sketch of the calibration arrangement.

In horizontal position ($\theta = 0^\circ$) with static weights, the normal force calibration, showed good linearity (*coefficient of determination* $R^2 > 0.999$ for a total number of $n_1 = 24$ observations) and repeatability ($0.02 \pm 14.2\%$, being 14.2% the normalised standard error of the mean zero offset) and the total amount of observations were $n_2 = 6$. The obtained calibration values were in agreement with the calibration data from the manufacturer. The calibration with static weights in horizontal position does not allow to calibrate the shear forces, since the normal force is equal to the weight.

In the flume with 27° angle the coefficients, although linear (*coefficient of determination* $R^2 > 0.997$ and $R^2 > 0.999$ for normal and shear forces respectively

with a total number of $n_1 = 24$ observations) and repeatable. The normal and shear forces measurements did not show offset drift during the calibration with the values $0.01 \pm 31\%$ and $-0.02 \pm 45\%$, being 31% and 45%, the normalised standard errors of the mean zero offset corresponding to the normal and shear force respectively. The values from the calibration were different than the calibration from the manufacturer. In the case of the normal force, the estimated scale values was $1 \text{ V} = 22 \text{ N}$ being 10 % higher than the manufacture calibration (i.e. $1 \text{ V} = 20 \text{ N}$). The shear force was estimated $1 \text{ V} = 12.5 \text{ N}$ being 25 % higher than the manufacture calibration (i.e. $1 \text{ V} = 10 \text{ N}$). The calibration curves for normal and shear forces are showed in Figure 2.9.

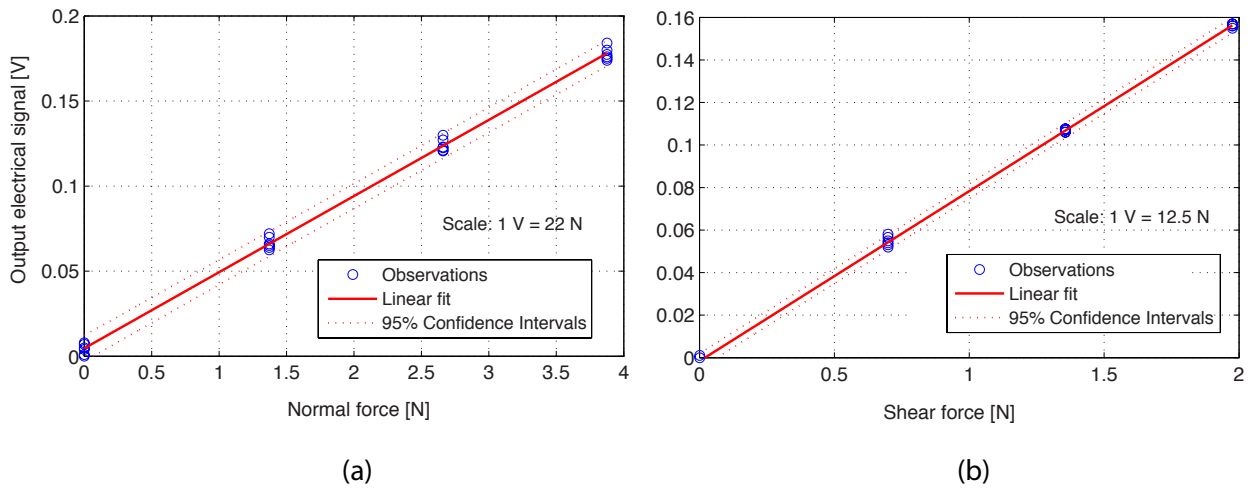


Figure 2.9. Calibration curves for the (a) normal and (b) shear forces. The voltage output from the sensor is converted to pressure using linear regression with a coefficient of determination $R^2 > 0.997$ and $R^2 > 0.999$ for normal and shear forces respectively. The dashed lines delineate the 95% confidence intervals.

The force plate calibration variation could be explained by the high sensibility of the small-scale force plates towards gradients in the local flow field where the force plate is located. When the force plate is fitted on to the base of the flume, small variation in the elevation could result in large differences in the measurement of the force plate.

The rubber gasket design with a watertight membrane covering the force plate could significantly change the stiffness under a dynamic applied load. Therefore, the normal and shear stress was calibrated with moving weights to ensure that

the sensitivity of the slope angle coefficients and any possible damping through the membrane was well defined. The moving weight was generated by releasing from behind the lock gate 10^{-3} m^3 of water. The normal force was calibrated by comparing the maximum value of the normal force and the maximum value of the pore pressure reading (Figure 2.10), however, the maximum values could not be totally representative due to the spatial and temporal pressure variations on the plate. The resultant applied factor was 0.74.

The shear stress was calibrated by using the shear force per unit area exerted by a “block” of water on the force plate by using the depth-slope product (e.g. Mueller *et al.* , 2005) as

$$\tau_e = \rho g d \tan \theta, \quad (2.3.7)$$

where τ_e is the estimated shear stress, ρ the density of the water, g the gravitational acceleration, d depth of the water and θ is the slope of the flume. The depth of the water was calculated by measuring the height of the flow at the force plate position. The height measurement showed scatter values as a consequence of the splashes and the drops on the side wall. Using the same calibration factor as for the normal stress gave fairly good accordance results (Figure 2.10).

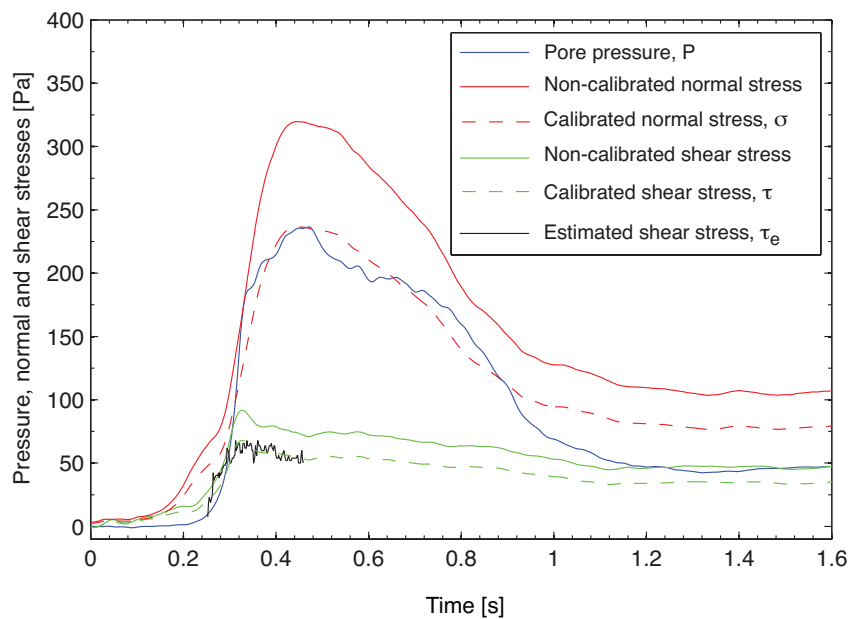


Figure 2.10. Calibration curves for the normal and shear forces under a dynamic applied load by realising 10^{-3} m^3 of water from behind the lock gate of the flume.

2.3.2 Data acquisition and processing

The sensor outputs were amplified by a Validyne demodulator (model MC1-CD18) and a Kistler amplifier (type 5011B) for the differential pressure transducer and the force plate respectively. The signals were amplified to ± 10 Vdc and recorded in Labview [Blume, 2007] via a Data Acquisition Card (National Instruments M-Series USB-6212). The Nyquist-Schannon's sampling theorem states that best reconstruction of a signal is possible when the sampling frequency is greater than double the system natural frequency (e.g. Ao & Gelman, 2010; Essick, 2012). The highest natural frequency for the sensor is for the Kistler force plate at 21 kHz in the normal force direction, being 5 kHz for the shear force direction, as specified by the manufacturer. The acquisition sampling rate was selected at a low frequencies to avoid including intrinsic noise and reduce the size of the recorded data. Therefore, the data for the present experiments was acquired at 1000 Hz leading to under sampling, especially in the faster flows. To sufficiently resolve the under sampling issue, the acquisition sampling rate should have been selected at a frequency higher than, or at least, 42 kHz.

The output data was filtered to remove noise using a smoothing spline fit method [Unser, 1999]. Time zero was established as the time when the gate was opened. Data sampling and recorded high speed (700 Hz) imaging were started before the gate was opened. The images were time zeroed visually.

These were synchronised with the pressure and stress data by identifying the front arrival time at the sensors. The front arrival was estimated using the first derivative of the basal normal stress. The uncertainty over the arrival time may be a result of the soft membrane used between the roughness element base and the force plate. Therefore, the time arrival was estimated when the measured basal normal stress reaches a threshold (i.e. 25%) of its total maximum value.

There is a time lag between the flow reaching the force plate and the pore pressure sensor due to the along-flume displacement of the pore pressure sensor compared to the force plate location (Figure 2.11). The time lag has been calculated tracking the flow edge with the front view camera. The maximum lag time range is from 0.05 to 0.3 seconds for mixtures with water or glycerol respectively. In particular for water

mixed flows, this is small compared with the response lag, indicating the presence of a dry snout (Section 3.3).

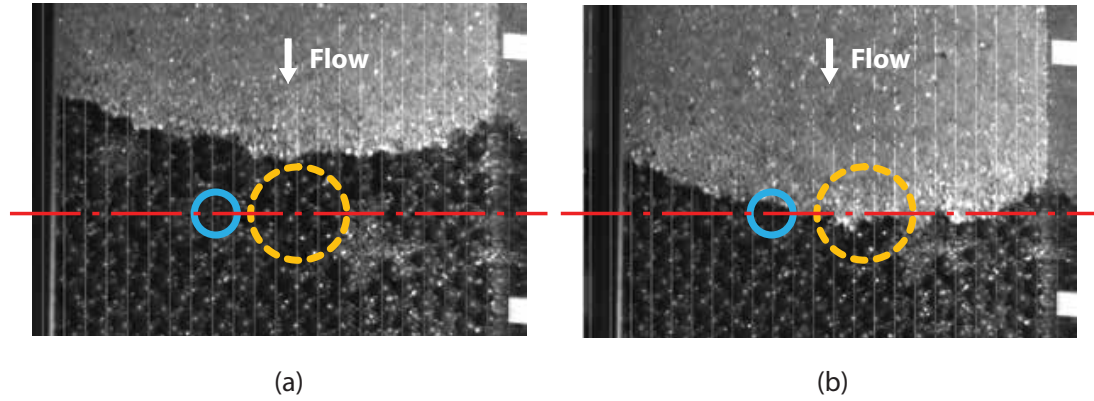


Figure 2.11. (a) Front view of the flow approaching the sensors. The centre line of the sensors is shown. The circles with solid and dashed lines delineate the pore pressure sensor and the force plate respectively. (b) The flow edge passes the centre line of the force plate sensor before reaching the pore pressure sensor due to their relative streamwise location.

2.3.3 Image acquisition

For the image acquisition high speed cameras, Dantec Dynamics NanoSense MK III, were used to capture the side view and front view at 700 frames per second, 1 M pixel resolution, with a NIKOMN 60 mm lenses. Figure 2.12 shows the cameras and light set up for the experiments. The selection of the image resolution, the image acquisition rate and the illumination require an optimum relationship within these parameters. The image resolution is adjusted to record only the region of interest. The image acquisition rate was chosen considering the fastest flows and those ones which exhibit a cloud of collisional and saltating particles on the front, in order to be able to track the particles with a good resolution, avoiding blurred images. Higher acquisition rate promise better tracking but drastically reduce the shutter time, leading to darker and noiser images. Both high speed cameras were synchronised with each other and connected to the computer via USB, recording the images using Motion Studio software (IDT). The side camera was positioned facing the glass side wall and angled to achieve maximum pixel resolution in the dominant direction of motion.

The deposits of the flow were recorded using a single lens reflex camera .

The calibration of the cameras to convert the pixels into millimetres was made by using white marks at 0.1 m intervals along the flume (x direction) and perpendicular to the flume (z direction).

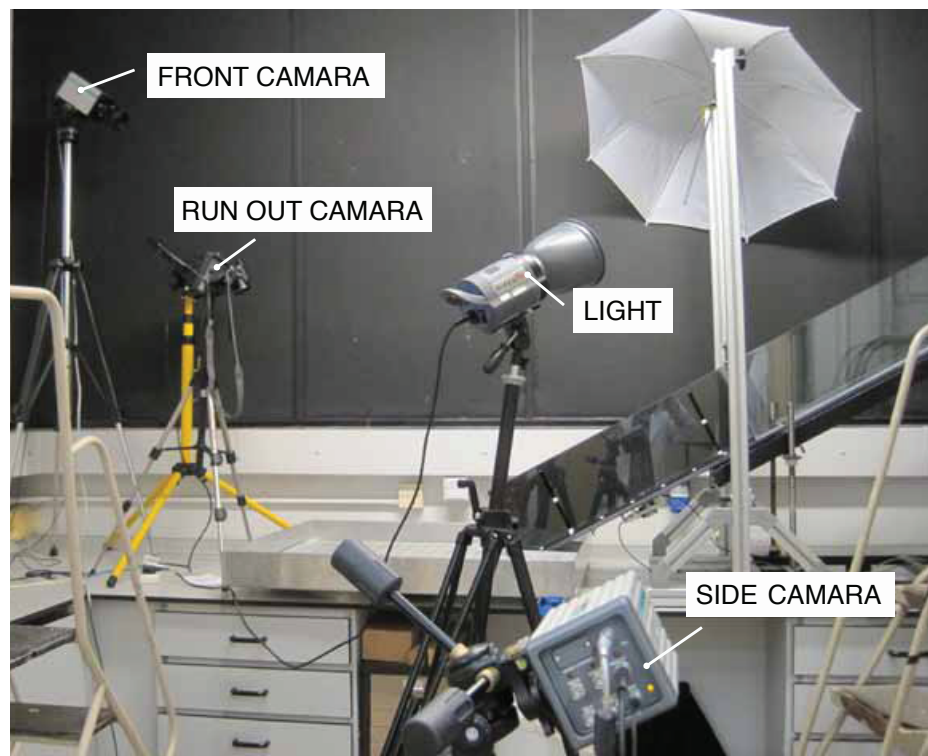


Figure 2.12. Illustration of the flume with a built-in lock gate and adjacent run-out tray.

2.4 Data Analysis

The evolution of the internal flow structure was determined using a Particle Image Velocimetry (PIV) image processing technique applied to the recorded image sequences.

2.4.1 Particle Image Velocimetry technique

Image velocimetry techniques are optical methods which resolve flow velocity fields from a sequence of images [Adrian, 1991].

In the present experiments, Particle Image Velocimetry (PIV) is used rather than Particle Tracking Velocimetry (PTV). The main reason for not applying PTV is that this technique requires high frame rates. To use PTV a frame rate is required that allows the particles to move a distance of approximately half their diameter with each frame. For particle diameter of 2×10^{-3} m moving at 1.5 m s^{-1} the minimum frame rate required would be $2 \times 1.5 / (2 \times 10^{-3}) = 1.5 \text{ kHz}$. Ideally the frame rate would be bigger.

The PIV method is based on pattern matching in an Eulerian way by calculating the mean displacement of particles in an interrogation window in the plane of the image (i.e. viewing direction). The principle is to divide the image plane into smaller regions or sub-windows, referred usually as ‘interrogation windows’, and uses cross-correlation algorithms between two consecutive frames to define the most probable spatial displacement of the particles (and hence velocity) in the interrogation window. The total region of interest is analysed by computing the correlation between overlapped interrogation windows. For optimum resolution, a homogeneous distribution of the particles and an optimised window size are required [Raffel, 2007]. The minimum window size is limited by the particle size (it must be larger than the particle diameter) and the packing of particles. Assuming a homogeneous particle distribution, and after several assessment tests, the size of the window was defined as $2d_{p3}$ corresponding to 40 pixels. Since the PIV technique operates on the image texture, for simplicity this selected resolution was used for all the different particle diameters. Nevertheless, for the small particles, a smaller size of the window could have been selected, especially if the interest had been to resolve internal details, such as rotation of the particles, however, this was not the case. The overlapping or spacing of the window (i.e. half d_{p3}) was chosen. Smaller spacing of the window would have lead to excessive time consumption to complete the PIV process.

This image processing set up was implemented within Digiflow image processing software [Dalziel, 2000-2012].

The PIV method was applied to the particles in contact with the side walls assuming that the flow is homogeneous in the transverse direction. This estimation is subject to error since variation in the flow across the channel was observed due to the

side wall effect which affecting to the velocity values. Similar experimental evidences have been documented [Ancey, 2001; Armanini *et al.*, 2005; Zanuttigh *et al.*, 2002].

2.4.2 Image processing

The recorded images had a 488×1280 pixel resolution, with a grey scale intensity assigned by an integer varying between 0 (black) and 255 (white).

The images showed varying background light intensities due to the flare from the fluid, and the splashes hitting the side walls. To reduce this noise, and to improve the efficiency of the PIV analysis, whilst still preserving the structural properties of the flow, the images were segmented to distinguish the foreground (the flow) from the background with the background being mask with zero value grey scale allowing a more efficient PIV analysis. The image segmentation was produced by using the algorithms in MATLAB's Image Processing Toolbox.

There are different methods to performance image segmentation, the most known being based on thresholding method, colour-based segmentation, transform methods, or texture methods. (e.g. Gonzalez *et al.* 2004; Shapiro & Stockman 2001; Srinivasan & Shobha 2007).

The thresholding method is proposed here due to its simplicity and suitability for the recorded images which have a background and foreground with different grey scale levels. With the thresholding method the pixels are partitioned depending on their intensity values, therefore, the contrast of the images was enhanced using the adaptive histogram equalization technique CLAHE [Zuiderveld, 1994]. Figure 2.13a shows the original dark image with very low contrast. The corresponding histogram (Figure 2.13b) shows most of the pixel values clustered in a small area with the values corresponding to the low intensity level. The CLAHE processed image in Figure 2.14a shows a higher contrast. The histogram (Figure 2.14b) has values more evenly distributed than the original histogram, and the intensity level has been slightly increased.

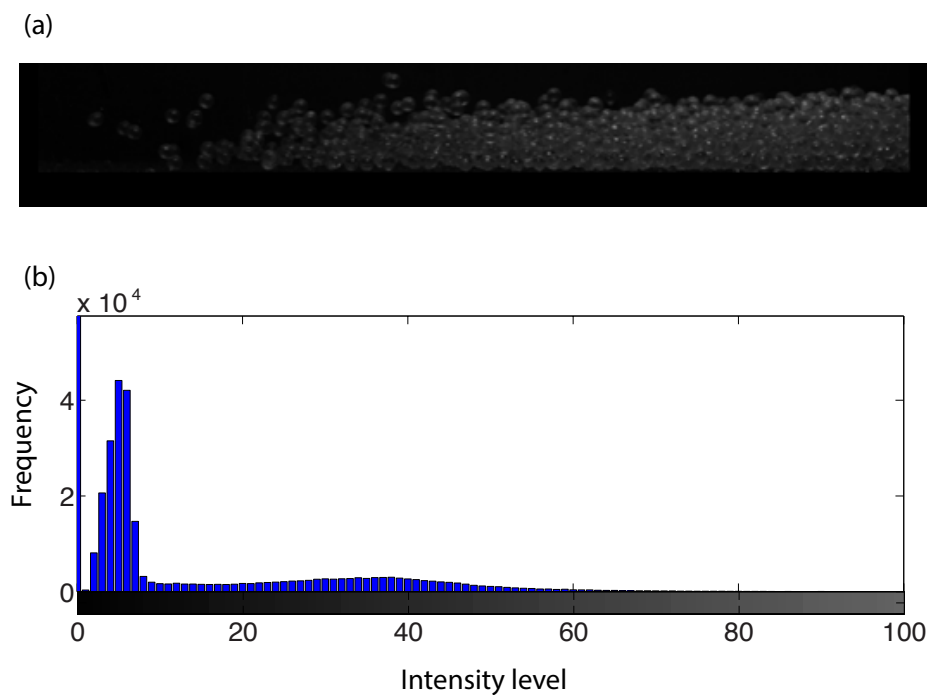


Figure 2.13. (a) Original image before being processed and (b) the corresponding histogram of the pixel intensity values. Intensity level of the histogram should be cover from 0 to 255, however it only shows relevant data which occurs until 100 intensity level.

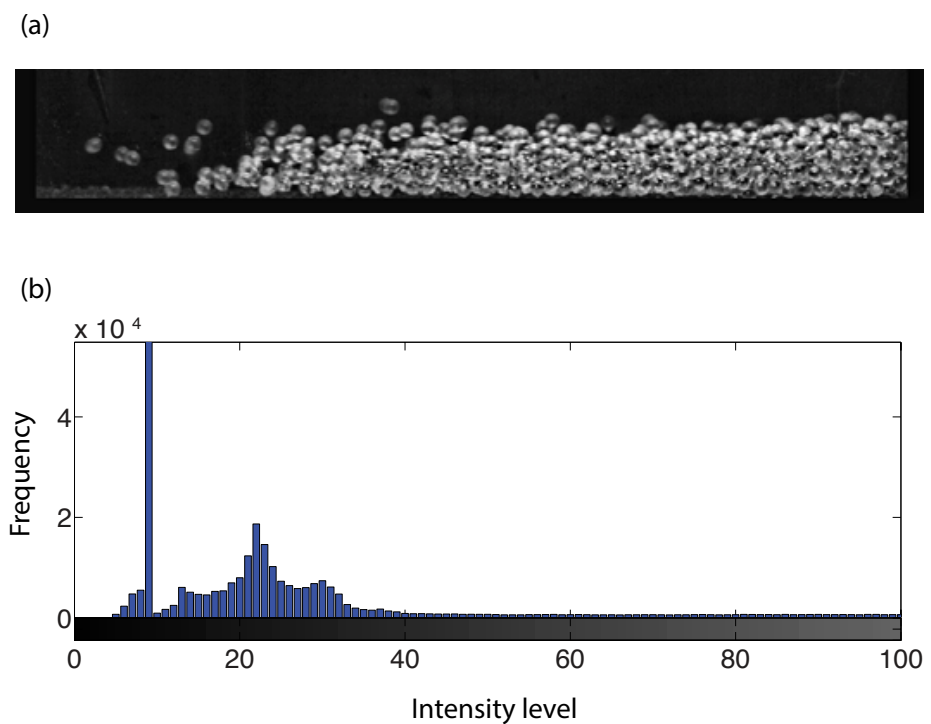


Figure 2.14. (a) Enhanced contrast of the grey scale image. (b) Histogram of the pixel intensity. Intensity level of the histogram should be cover from 0 to 255, however it only shows relevant data which occurs until 100 intensity level.

After enhancing the contrast of the image with the adaptive histogram equalization technique CLAHE, the grey level threshold was obtained using Otsu's method [Otsu, 1975], turning the grey scale images (Figure 2.14a with intensity range from '0' to '255') into a binary images (Figure 2.15a with only '0' and '1' intensity levels). The resulting binary image presented gaps within the foreground. This is, the foreground which corresponds to regions with '1' intensity level pixels showed small regions with unintended '0' intensity level, which was removed by dilating the binary image and infilling the holes resulting as in Figure 2.15b. The dilating and infilling processes were obtained using *imdilate* and *imfill* commands from MATLAB.

The perimeter boundaries of the flow are defined by the boundary between binary regions of 0 and 1. This will give the index position of the flow, which it is used to distinguish the flow from the background in the grey scale images. There also are different edge detection algorithms available in MATLAB (e.g. Canny method to find local maxima of the gradient of the pixel intensity, e.g. Gonzalez *et al.* , 2004).

In the region between the base of the flow and the roughness element surface, small regions could suffer from unintended removal during the segmentation processes. To include this as part of the foreground, a polygon was created (Figure 2.15c) which moves with the region of the maximum area of the flow defined with *regionprops* properties tool in MATLAB (Figure 2.15c dashed line box). The polygon index values were then added to the foreground region. At this point the foreground (the flow) and the background are well defined allowing the background to be masked. The Figure 2.15d shows the grey scale image with a masked background.

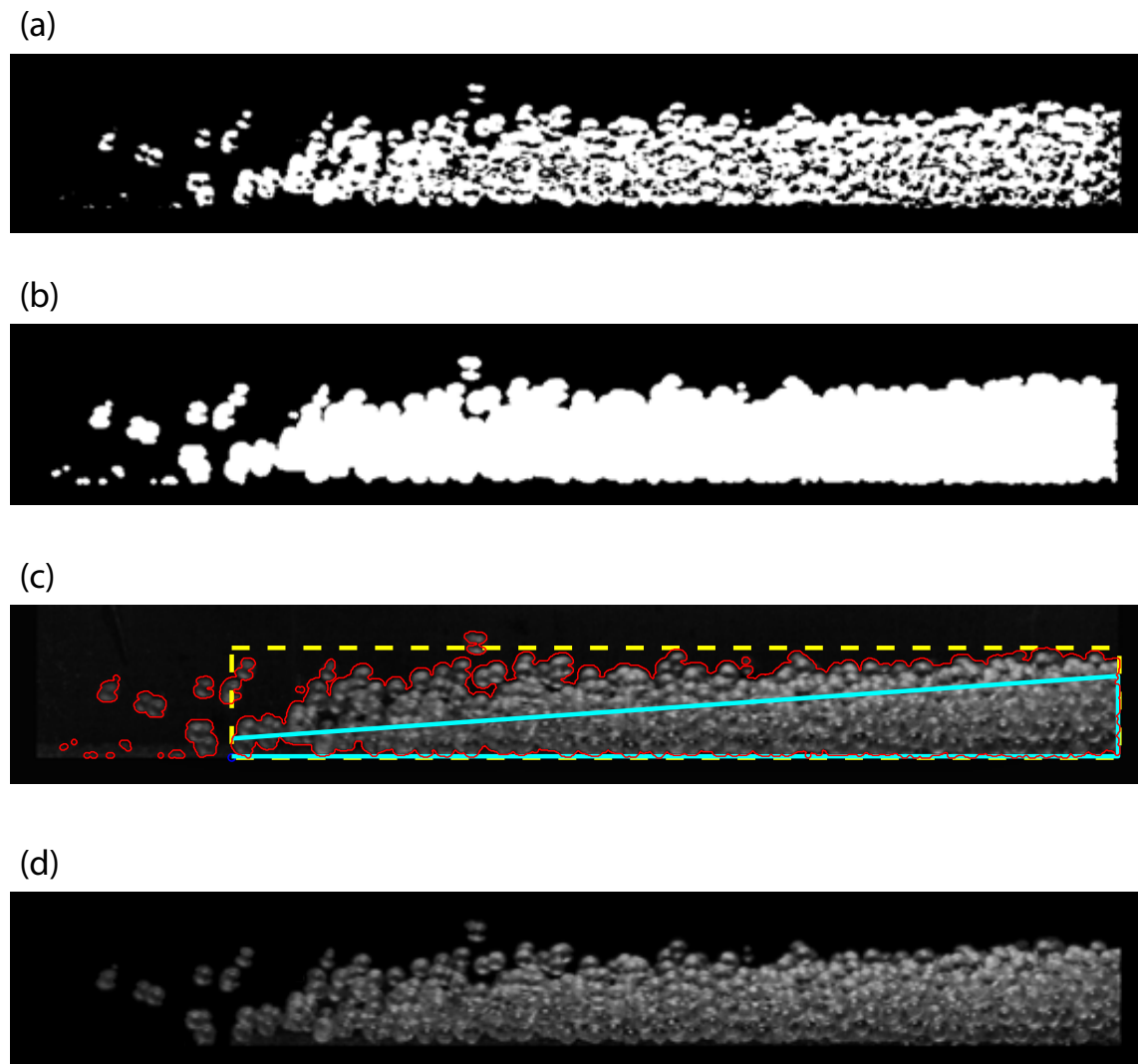


Figure 2.15. (a) The binary image obtained by grey level thresholding Otsu's method and (b) after dilation with filled holes. (c) The grey scale image before masking the background. The edge of the flow is highlighted with a line around the flow, which corresponds to the perimeter of the above image. The dashed line box marks the maxima region of the flow, which delimits the solid line polygon size. The index defined by the polygon were added as part of the foreground region. (d) The grey scale image after masking the background of the foreground.

2.4.3 Characteristic front flow position and flow height

The variability of the experimental flows makes it challenging to define the front flow position and the flow height. Some of the flows move in a lumpy way leading to a straight front flow in the cross-flow direction, while other flows show particles saltating at the front and top of the flow, making it difficult to define the edge of the front [Pouliquen, 1999] and flow height. In order to systematically obtain data a statistical method is used based on velocity profiles obtained with PIV technique. The standard deviation of the velocities from the local averages are calculated over a time window of 0.02 s (corresponding to 14 frame blocks). Once fully developed, variations of the flow mean velocity are small within this interval of time. However the standard deviation from this mean depends particularly on the type of regime. Figure 2.16a illustrates the standard deviation of the local averages of the velocities calculated over 14 frames block. The sharp transition from low ($< 150 \times 10^{-3} \text{ m s}^{-1}$) to high ($\geq 150 \times 10^{-3} \text{ m s}^{-1}$) standard deviation from the local mean determines *non-fluctuating* and *intermittent collisional* behaviours (further definition of these regions is discussed in Chapter 3). Figure 2.16b shows the edges of the two coexisting regions determined by the selected threshold standard deviation.

Separating these two regions allows clearer definition of the bulk properties of the flow. The *non-fluctuating* region, with low deviation from the local mean (i.e. $< 150 \times 10^{-3} \text{ m s}^{-1}$), determine the characteristic front flow position $x_f(t)$ and flow height $h(x, t)$. In order to estimate the characteristic front position of the flow, the convex hull [Barber *et al.*, 1996] of the set of points which define the edge of the non-fluctuating region is estimated using the *convhull* MATLAB function. The intersection of the non-fluctuating edge with the flume determines the front position of the flow (Figure 2.16c). The characteristic height $h(x, t)$ is defined by the boundary of the region with low standard deviation ($< 150 \times 10^{-3} \text{ m s}^{-1}$) which corresponds to the maximum flow depth along this region (Figure 2.17). The total flow height $H(x, t)$ includes the intermittent collisional region with high standard deviation ($\geq 150 \times 10^{-3} \text{ m s}^{-1}$), corresponding to the total flow depth (Figure 2.17).

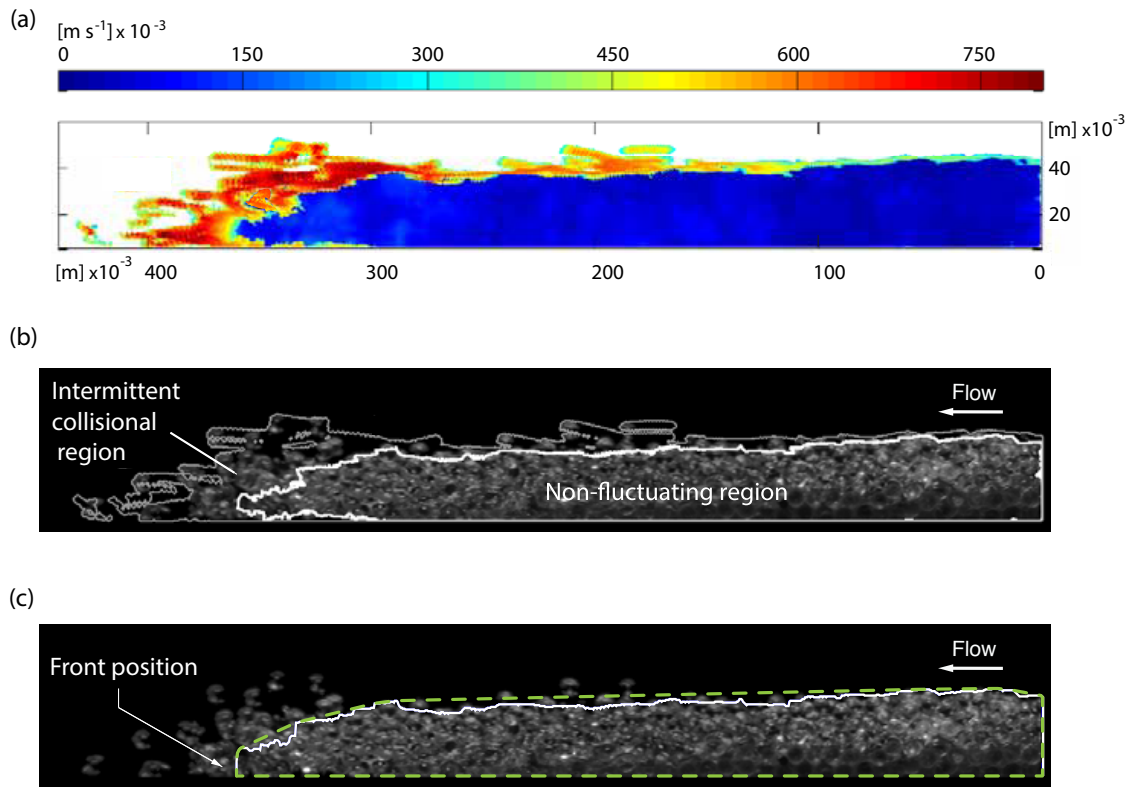


Figure 2.16. (a) Colour map visualising the standard deviation of the velocities from the local 14 frame average, of a mixture with 8×10^{-3} m particle diameter mixed in water with solid volume fraction 0.6 over a 8×10^{-3} m roughness element diameter. Colour bar represents the standard deviation in $m s^{-1}$ from blue (low standard deviation) to red (high standard deviation). (b) The edges correspond to the standard deviations, with white and grey line corresponding to the non-fluctuating region with low standard deviation ($< 150 \times 10^{-3} m s^{-1}$) and intermittent collisional region with high standard deviation ($\geq 150 \times 10^{-3} m s^{-1}$) respectively. The edge of the two regions are superimposed with the 14th frame of the corresponding block. (c) The convex hull of the non-fluctuating edge values corresponds to the dashed line. The front position is highlighted with a small circle.

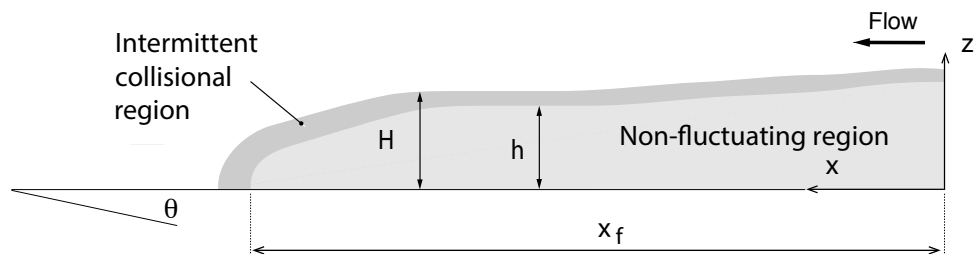


Figure 2.17. Schematic of the flow moving down a flume with an inclination angle of $\theta = 27^\circ$. The flow is divided in two regions. Pseudo-plug region, with the low standard deviation from the local average, shaded light grey and intermittent collisional region with high standard deviation is shaded dark grey. The characteristic height of the flow and front flow position are defined by the non-fluctuating region as h and x_f respectively. The total flow height H includes the intermittent collisional region.

2.5 Conclusions

These experiments allow the systematic testing of different variables that influence the behaviour of fluid-particle mixtures, accomplishing a better understanding of the underpinning physics of debris flow behaviour.

Flow depth, front position and velocity distribution were obtained by image processing of recorded high speed images and using a Particle Image Velocimetry (PIV) technique. Pore fluid pressure and basal normal and shear stress measurement at the base of the flume, along with velocity distributions provide an extensive data set for assessing the influence individual variables (i.e. particle diameter, interstitial fluid, solid volume fraction and roughness element diameter).

The characteristic front position and flow height are systematically determined using a statistical method based on the standard deviation from the local average velocities obtained using the PIV data.

Chapter 3

Morphological characteristics of laboratory debris flow

In this chapter morphological characteristics of debris flow are discussed based on data from the laboratory experiments described in Chapter 2.

The inhomogeneous architecture of the debris flow, with high friction granular snouts and liquefied tails, has been previously attributed as the result of grain size segregation, due to mixture agitation and changes in pore fluid pressure as consequence of the presence of fine sediments such as clay and silt [Iverson, 1997, 2003; Iverson *et al.*, 2010; McArdell *et al.*, 2007]. These conjectures rise a crucial question: should it not be expected the formation of granular snout and liquefied tails in mono-disperse mixtures that do not contain any fine sediments? How do particles interact with the fluid to get head-body architectures? How does the fluid pore pressure evolves in space and time in mono-disperse mixtures?

Flows testing the influence of particle size, roughness element diameter, interstitial fluid viscosity and solid volume fraction, exhibited similar morphological characteristics to full-scale debris flow, such as deposition and particle segregation effects. Experiments with mono- and poly-disperse components mixed with liquids without fine sediments, reveal a head and body structure and appearance similar to the classic anatomy of real debris flows [Iverson, 1997; Iverson *et al.*, 2010; Johnson *et al.*, 2012; McArdell *et al.*, 2007; Takahashi, 2007].

Laboratory debris flows consisting of 1 litre of dry glass beads, or mixed with water or glycerol, were released behind the lock gate, descended by a surge on an inclined flume with different element diameter roughness and deposited on an horizontal run-out tray.

The front part of the surge, exhibits the higher solid volume concentration of large particles (referred as granular front or snout), unsaturated with little fluid content followed by a gradually tapering flow (body), ending in a thinner part (tail) with a decreased solid volume concentration (Figure 3.1).

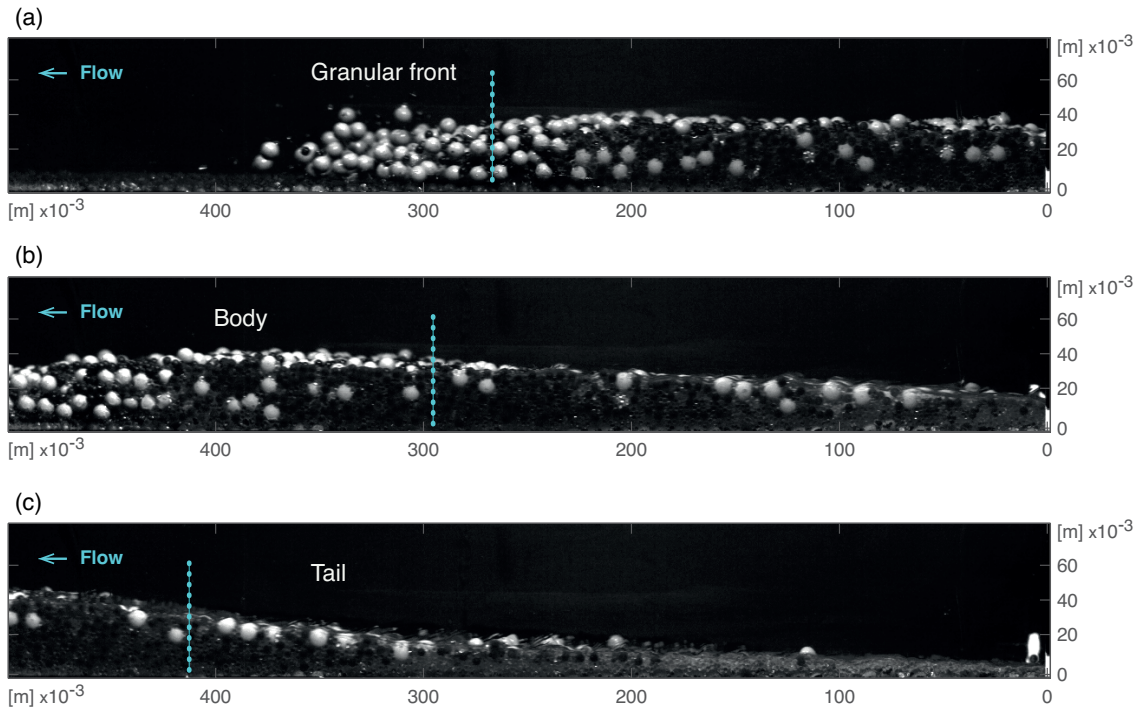


Figure 3.1. Side view of a laboratory experimental flow demonstrating reproducible key feature of natural debris flows. The release of $1 \times 10^{-3} \text{ m}^3$ volume of a mixture of particles from $2 \times 10^{-3} \text{ m}$ (colourless), $4 \times 10^{-3} \text{ m}$ (black) to $8 \times 10^{-3} \text{ m}$ (white) to solid volume fraction of 0.6 in water over a roughness element of $8 \times 10^{-3} \text{ m}$, moving down a flume with an inclination angle of 27° . The percentage of the release volumes were 50 %, 30 % and 20 % of 2×10^{-3} , 4×10^{-3} and $8 \times 10^{-3} \text{ m}$ particle diameters respectively. (a) A granular front characterized by low fluid content and by the accumulation of large particles, follow by (b) the non-fluctuating region or core of the flow, and (c) the tail mostly liquefied with some scattered big particles.

The laboratory debris flows, consisting of uniformly round particles, form stable fronts and no fingering instability was observed [Pouliquen & Vallance, 1999; Pouliquen *et al.*, 1997]. The evolution in time of the front of the flows indicates a quasi 2-dimensional flow (Figure 3.2).

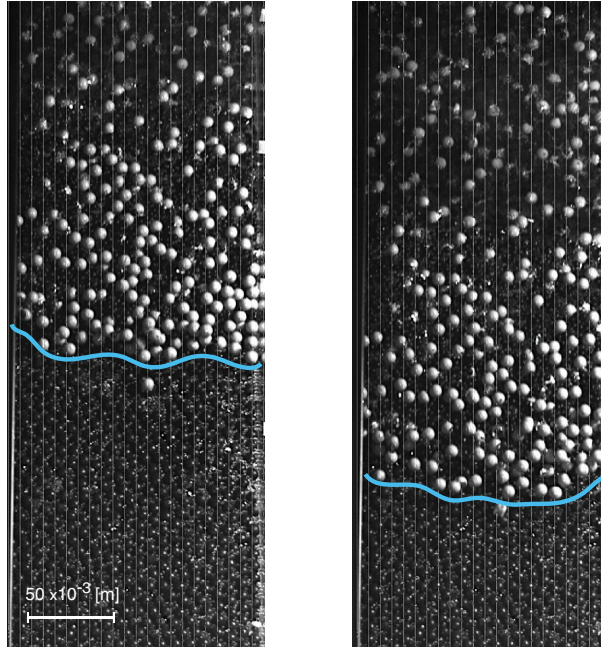


Figure 3.2. Front flow evolution of poly-disperse mixture of solid volume fraction 0.6 with water at $t = 0.39$ s and 0.46 s since gate opening. The blue line depicts edge of the front flow.

In this chapter the non-fluctuating region and the intermittent granular cloud region are defined. The extent of these regions is related to flow properties. Further architectural characteristics of the laboratory flows are discussed, such as particle size segregation effects and the formation of a dry granular snout. Finally, the patterns of the flow deposits are presented.

3.1 The structure of laboratory debris flows

The flows move in an open channel with a free boundary at the top of the flow and as the flow shears, particles can not only translate at the average flow speed, but also exhibit fluctuations about that speed. Distinct regions are characterized by either particles moving with almost the same velocity as the local average velocity

of the flow or agitated particles moving more freely with a velocity which differs significantly from the local average velocity.

Here, variation from the average velocity are visualized in Figures 3.3, 3.7 and 3.9. Colour maps depict the standard deviation of the velocities from the local averages, estimated from the means velocities over 14 frame blocks (see Section 2.4). The two dimensional local velocity average profiles show the evolution of the shear stress vary through the flow depth at positions 10%, 50% and 90% distance from the nose of the flow.

These colour maps show the clear definition of the coexisting regions.

- *Intermittent collisional region:*

These are regions dominated by particle collision are characterized by large rapid deformations with ubiquitous raised granular temperature. Flow in this region has velocities that markedly differs from the local average velocity of the flow. High standard deviation can also be the consequence of the intermittency of the flow at a location. Regions which are identified with standard deviation of mean velocities higher than $150 \times 10^{-3} \text{ m s}^{-1}$ are referred, in the present work, as *intermittent collisional region* due to the physical resemble of the term ‘intermittency’ used in turbulent fluid flows [Pope, 2000].

- *Non-fluctuating region:*

This is the relatively compact layer of particles with low deviations from the local mean velocity (i.e. standard deviation lower than $150 \times 10^{-3} \text{ m s}^{-1}$).

Evolution of flow behaviour with variations of roughness element diameters, different interstitial fluids and solid volume fractions, are illustrated in the Figures 3.3, 3.7, and 3.9 respectively and discussed in the following. The non-fluctuating regions ($\leq 150 \times 10^{-3} \text{ m s}^{-1}$), and the intermittent collisional regions ($> 150 \times 10^{-3} \text{ m s}^{-1}$) are represented by the light and dark grey patches respectively. The transition between two regions is well defined by the selected threshold of standard deviation of $150 \times 10^{-3} \text{ m s}^{-1}$, which denote the maximum detectable change. The threshold value of $150 \times 10^{-3} \text{ m s}^{-1}$ was chosen because to this value seems to clearly define the transition between the two regions. The extent of the intermittent collisional region is

unaffected by the selected threshold value since this region is dominated by very high standard deviation in comparison with the selected threshold of $150 \times 10^{-3} \text{ m s}^{-1}$.

3.1.1 Effect of particle and roughness element diameters on structure

The dependence of the extent of regions of non-fluctuating and intermittent collisional behaviour on the particle and roughness element diameter is analysed. Mixtures with 0.6 particle volume fraction, with mono-disperse particles from 2×10^{-3} 4×10^{-3} and 8×10^{-3} m and poly-disperse with mean particle size of 4×10^{-3} m, showed unambiguous transitions between regions (Figure 3.3).

More intermittent collisional behaviour is observed near the free surface of the flow and at the front. Regions of high particle activity seem to be more extended with increasing particle diameter in the flow mixture. Small particle diameters exhibit little intermittent granular behaviour (Figure 3.3a, 3.3e and 3.3f), when compared with larger particles (Figure 3.3b, 3.3f and 3.3j with 4×10^{-3} m diameter and 3.3c, 3.3g and 3.3k with 8×10^{-3} m diameter).

With smaller particle sizes little interstitial fluid escapes from the bulk flow making the whole flow moves *en masse*. In flows of water with bigger particles, fluid is not constrained within the particle matrix.

Extended regions of high standard deviation on the free surface and near the front of the flow are also noted with mixed particle sizes (Figure 3.3d, 3.3h and 3.3l). Size segregation is observed in these poly-disperse flows (Figure 3.1), where large particles rise to the top free surface and migrate to the front [Ancey, 2012; Iverson, 1997; Iverson *et al.*, 2010; Johnson *et al.*, 2012; McArdell *et al.*, 2007; Pouliquen & Vallance, 1999; Takahashi, 2007]. The extent of the intermittent collisional region appears consistent with that in mono-disperse flows with the mean particle diameter of the mixture.

The influence of the roughness element diameter on flow behaviour is significant. Within the non-fluctuating region (the light grey regions in Figure 3.3), the smoother base surface (i.e. 2×10^{-3} m roughness element diameter) favoured a sliding motion, while increasing the roughness element diameter the local velocities

average increased rapidly with the height above the flume base surface as a result of the frictional resistance. Larger diameters of the roughness element cause more granular agitation at the base surface, leading to higher standard deviation regions. This is more evident when looking in detail at the non-fluctuating regions as in Figure 3.4. Within the non-fluctuating region, the standard deviation increases as the roughness element diameter, this is particularly notable near the base of the flow, and at the front of the flow.

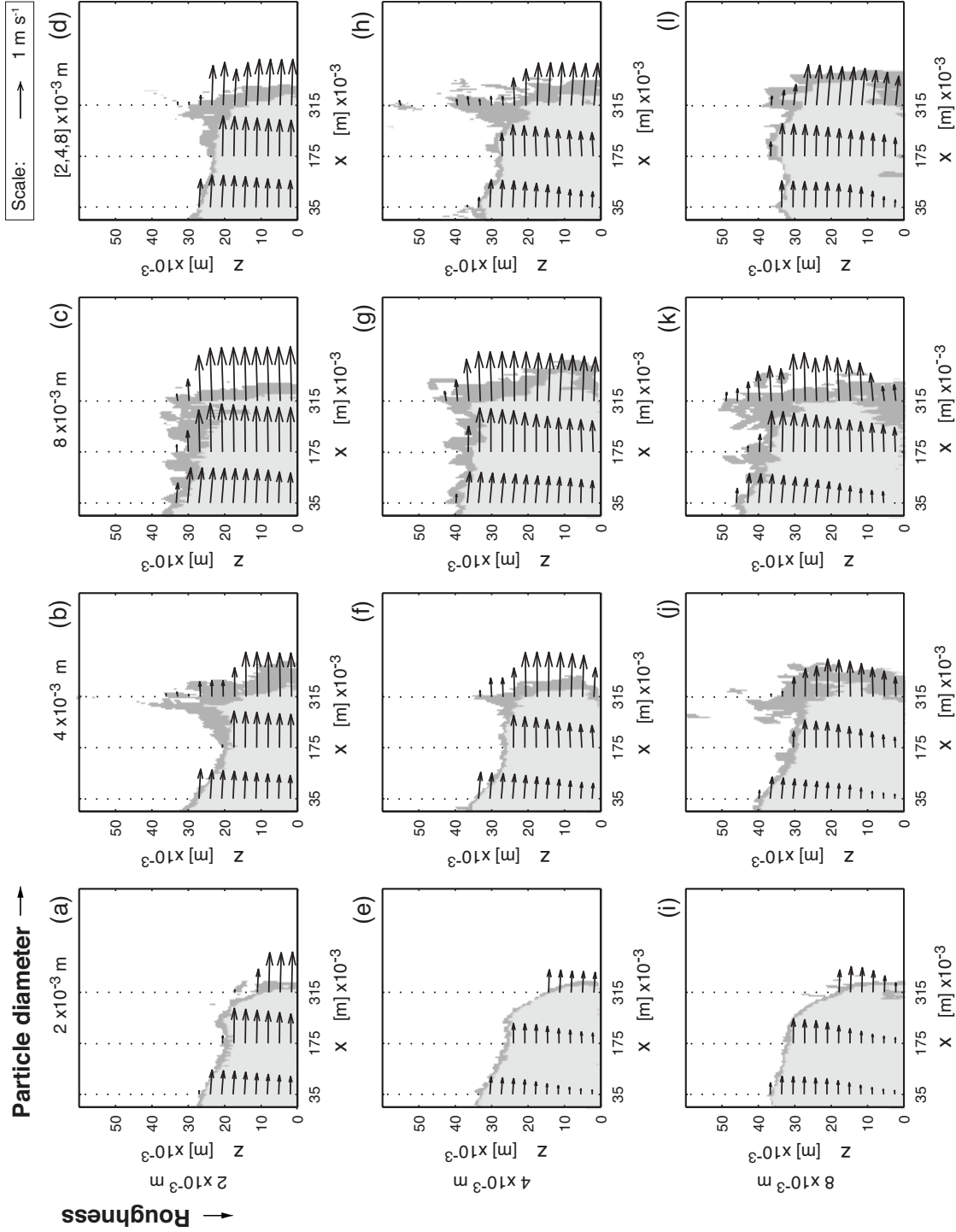


Figure 3.3. Colour map visualising regions of non-fluctuating (light grey corresponding to standard deviation $\leq 150 \times 10^{-3} \text{ m s}^{-1}$) and intermittent collisional behaviour (dark grey corresponding to standard deviation $> 150 \times 10^{-3} \text{ m s}^{-1}$) through the flow depth z along the length of the flume x , at the flow front position $x_f = 350 \times 10^{-3} \text{ m}$. Columns are arranged by particle size, from mono-disperse $2 \times 10^{-3} \text{ m}$ flows to mixtures of 2×10^{-3} , 4×10^{-3} and $8 \times 10^{-3} \text{ m}$ particles. Rows are arranged by roughness element diameter from 2×10^{-3} , 4×10^{-3} to $8 \times 10^{-3} \text{ m}$. Flows consist in particles mixed in water to a solid volume fraction of 0.6. Quiver plots of local velocity average at positions 10%, 50% and 90% distance from the nose of the flow, scaled accordingly to the legend.

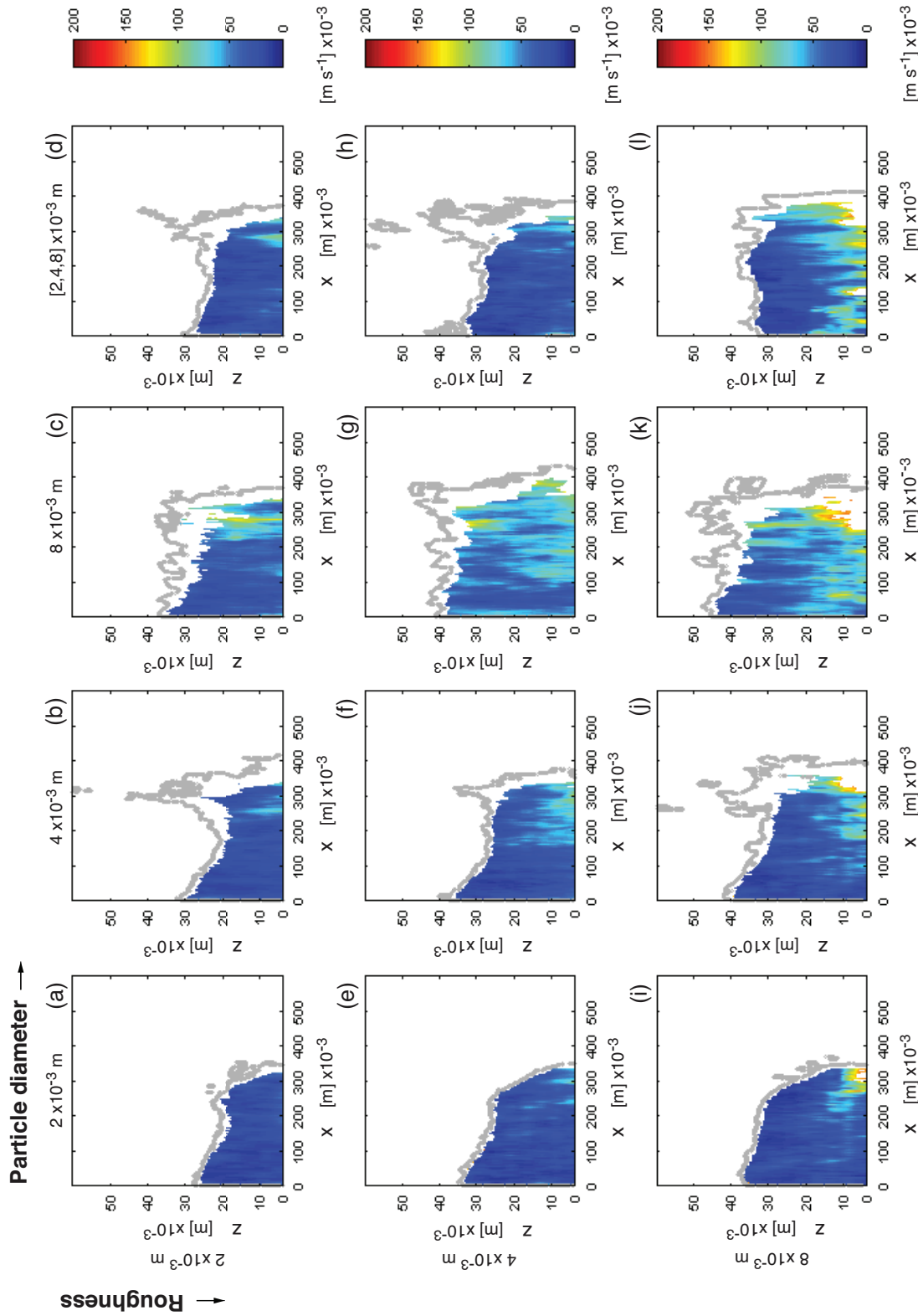


Figure 3.4. Colour map visualising regions of non-fluctuating behaviour through the flow depth z along the length of the flume x , at the flow front position $x_f = 350 \times 10^{-3}$ m. Intermittent collisional behaviour is not shown. The flow boundary depicted with a grey line. Columns are arranged by particle size, from mono-disperse 2×10^{-3} m to mixtures of 2×10^{-3} , 4×10^{-3} and 8×10^{-3} m particles. Rows are arranged by roughness element diameter from 2×10^{-3} , 4×10^{-3} to 8×10^{-3} m. Flows consist in particles mixed in water to a solid volume fraction of 0.6. Colour bar represents standard deviation from 14 frame average velocities in m s^{-1} , from blue (zero standard deviation) to orange ($150 \times 10^{-3} \text{ m s}^{-1}$ standard deviation) with same scale for the all the flows.

Front shape

The variation in the front shape of water-particle flows with a solid volume fraction of 0.6 over different roughness element diameter is examined (Figure 3.5). The shape and the height of the flow head varies significantly with the basal boundary conditions. Frontal shape, when the flow travels on a smooth basal surface exhibits triangular wedge shape, as shown in Figure 3.5a, 3.5c, 3.5e and 3.5g. Velocity profiles (Figure 3.3) also show that over smoother surfaces, the flow slides with very low shear (e.g. Figure 3.3a-d).

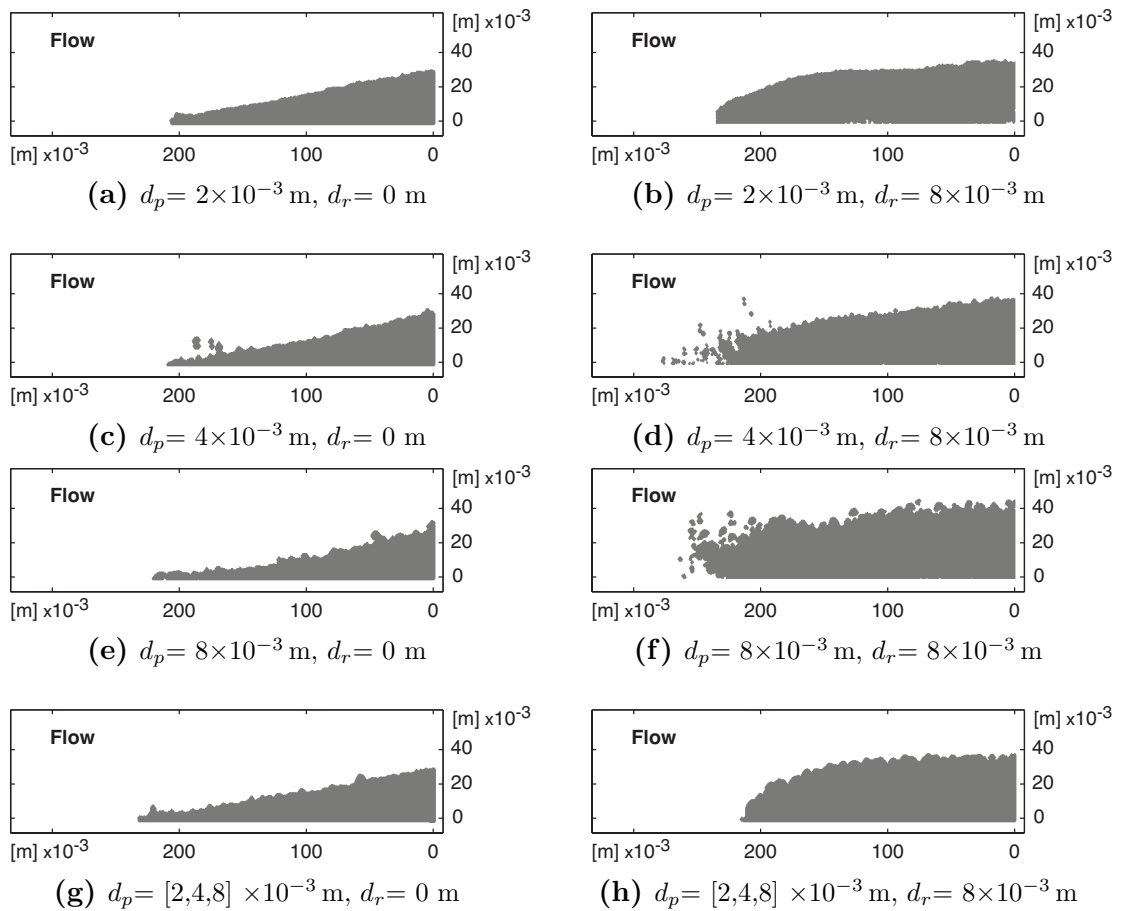


Figure 3.5. Influence of roughness element on the flow head. Left and right column for 0 and 8×10^{-3} m roughness element diameter respectively. Rows are arranged by particle size, from mono-disperse 2×10^{-3} m flows to mixtures of 2×10^{-3} , 4×10^{-3} and 8×10^{-3} m particles. Flows consist of particle mixed with water to a solid volume fraction of 0.6.

With a rougher basal surface, round snouts are observed due to the increased friction at the bottom that also increases shear through the flow and granular agitation (Figures 3.5b, 3.5d, 3.5f, 3.5h). The agitation at the base of the flow, due to the collision of the particles with the rough surface, propagates into the upper layers of the flow, creating a slight flow dilation. At the front of the flow, particles bounce in all directions, creating a dispersal blast of particles with the subsequent density variations [Bartelt *et al.* , 2012, 2006; Buser & Bartelt, 2011b]. Similar flow behaviour has been observed for powder avalanches at Swiss Vallée de la Sionne test side, especially with dry snow avalanches which exhibits “explosives eruptions of ice-dust plumes” [Bartelt *et al.* , 2014].

The tendency of the front of the presented laboratory debris flows to create this dilute granular front increases with the particle diameter (Figures 3.5b, 3.5d and 3.5f with 2×10^{-3} , 4×10^{-3} and 8×10^{-3} m respectively).

For the water mixture with mono-disperse 2×10^{-3} m particle, the front is well defined and particles seems to move in a more ‘rigid’ front (Figure 3.5b). The presence of small particles in the mixture makes a conspicuous change in the flow behaviour making the structure more cohesive. At earlier times, the flow does not exhibit saltating particles at the front.

The effect of bed roughness on the front shape was also studied for the cases where the particle diameter of the flows were the same as the roughness element diameter (Figure 3.6). Rounds snouts were observed, increasing slightly the total height of the flow with the increase in particle diameter.

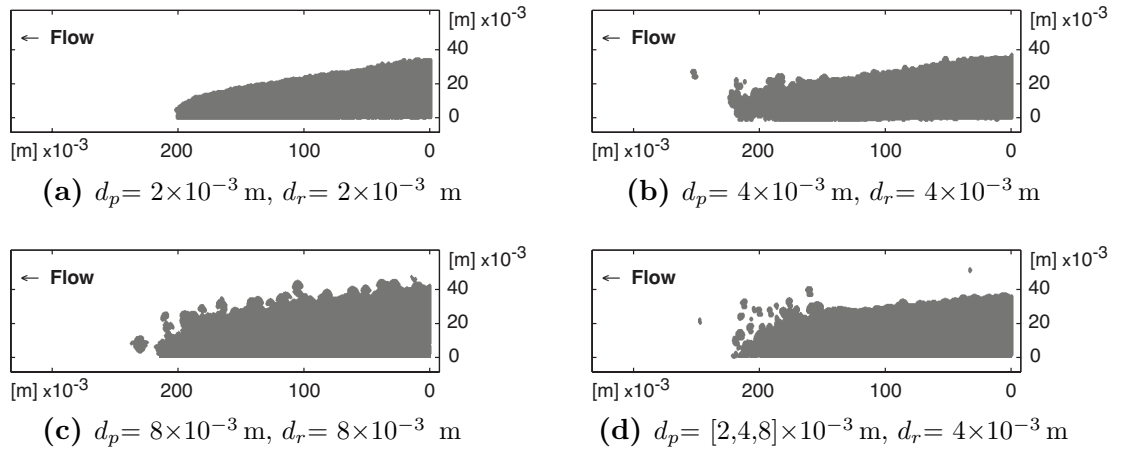


Figure 3.6. Influence of roughness element on the flow head where $d_p = d_r$. Flows consist of particle mixed with water to a solid volume fraction of 0.6.

3.1.2 Effect of interstitial fluid on structure

The behaviour of different flow mixtures is analysed based on the type of interstitial fluid. Dry granular flows, where interstitial fluid plays a negligible role, are compared with flows of particles in water or glycerol to a solid volume fraction of 0.6 (Figure 3.7).

Mixtures of mono-disperse particles from 2×10^{-3} , 4×10^{-3} and 8×10^{-3} m and poly-disperse with mean particle size of 4×10^{-3} m, with the same roughness element (i.e. 8×10^{-3} m diameter), exhibit more extended intermittent granular areas with dry conditions (Figure 3.7a-3.7d). These regions are located on the top surface of the surge and specially near the front. The elevation of the granular temperature related to this high active region is accompanied by an increase of the bulk volume.

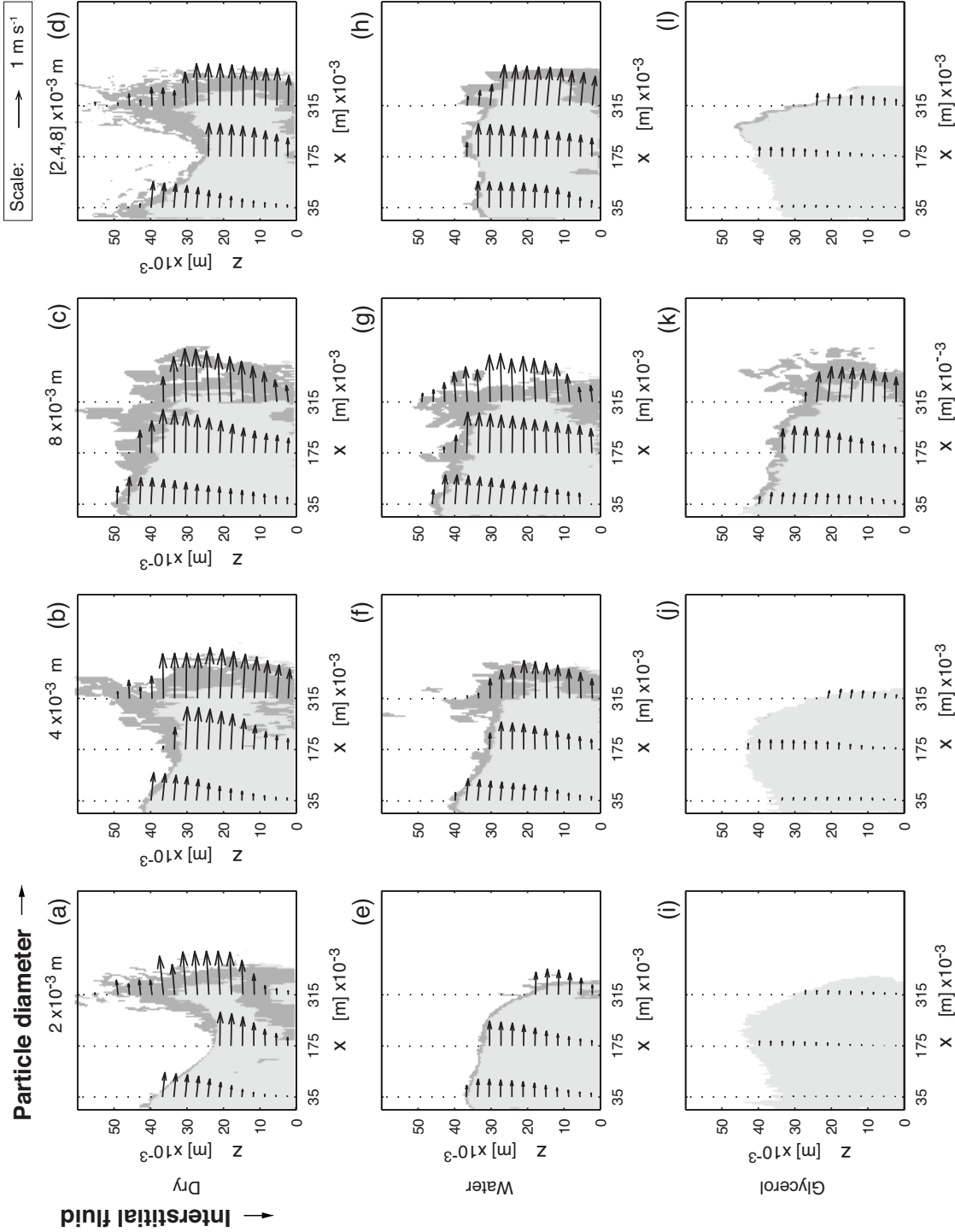


Figure 3.7. Colour map visualising regions of non-fluctuating (light grey corresponding to standard deviation $\leq 150 \times 10^{-3} \text{ m s}^{-1}$) and intermittent collisional behaviour (dark grey corresponding to standard deviation $> 150 \times 10^{-3} \text{ m s}^{-1}$) through the flow depth y along the length of the flume x , at the flow front position $x_f = 350 \times 10^{-3} \text{ m}$. Columns are arranged by particle size, from mono-disperse $2 \times 10^{-3} \text{ m}$ to mixtures of 2×10^{-3} , 4×10^{-3} and $8 \times 10^{-3} \text{ m}$ particles. Rows are arranged by interstitial fluids; dry, water, glycerol. All flows have roughness element diameter of $8 \times 10^{-3} \text{ m}$ and solid volume fraction of 0.6. Quiver plots of local velocity average at positions 10%, 50% and 90% distance from the nose of the flow, scaled accordingly to the legend.

The presence, and varying quantity, of interstitial fluid affects significantly the dynamic characteristics of the flow, and more particularly that of the small particle diameter. For the same solid volume fraction of 0.6 (high solid concentration) when mixed with water, only 2×10^{-3} m particles move with low deviations from the local mean velocity (Figure 3.7e). With increasing particle diameter, the intermittent collisional behaviour is more widespread. Since the action of the interstitial fluid passing through the space between particles depends on the pore space, the smaller pore space, the slower the fluid passes through. Therefore, small particles (less permeability) better retain the interstitial fluid than larger particles.

The non-fluctuating region appears to be controlled by viscous effects. When changing the pore fluid from water to pure glycerol (Figure 3.7i-3.7k), the whole flow moved at very low speeds, excepting the highest particle diameter used in the experiments of 8×10^{-3} m, (Figure 3.7k) which still showed some intermittent granular regime at the front of the surge.

Front shape

Dry flows exhibit abrupt dilated fronts formed by a cloud of collisional and saltating particles (Figures 3.11a, 3.11c, 3.11e, 3.11g). Whereas in the wet flows fluid restrains the particles to form a well defined and relatively highly packed round shape (Figures 3.11b, 3.11d, 3.11f, 3.11h).

3.1.3 Effect of solid volume fraction on structure

In this section, the effect of varying the solid volume fraction (0.4 and 0.6) is studied for the case of water and glycerol as interstitial fluids (Figure 3.9).

With small solid volume fractions the flows become saturated, changing the flow behaviour. In flows of small particles (i.e. 2×10^{-3} and 4×10^{-3} m diameter) and a mixture of particles, a fluid layer forms at the top surface (e.g. mixture of particles in glycerol with solid volume fraction 0.4 in Figure 3.10). Flows which present this characteristic are termed ‘immature flows’ in the debris flow literature [Takahashi, 1991]. The particles behave as an impermeable block inhibiting draining of the fluid through the flow.

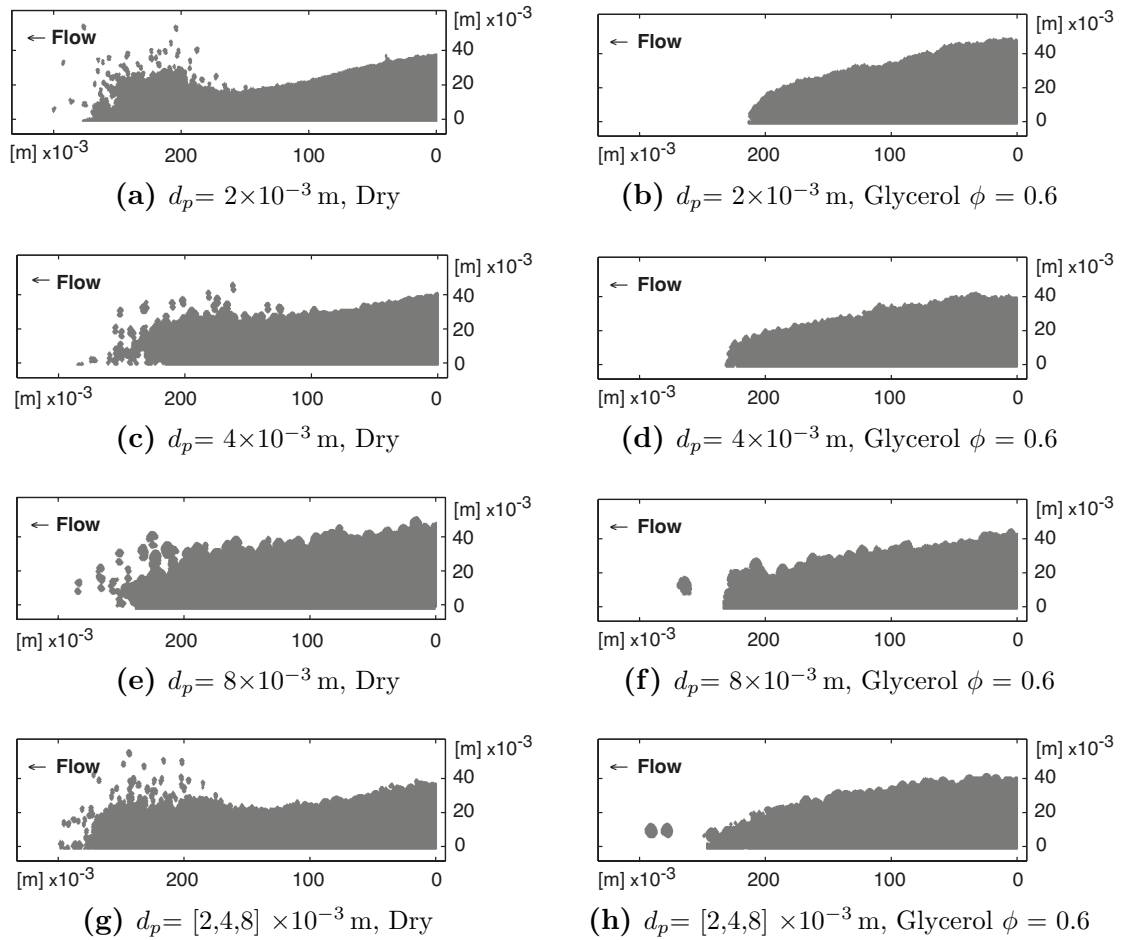


Figure 3.8. Effect produced on the flow head when adding glycerol as interstitial fluid. Columns are arranged by dry flows on the left and glycerol mixtures with solid volume fraction 0.6 on the right. Rows are sorted by particle size, from mono-disperse 2×10^{-3} m flows to mixtures of 2×10^{-3} , 4×10^{-3} and 8×10^{-3} m particles. The roughness element diameter of 8×10^{-3} m remained fixed.

The high standard deviations seen in the upper regions of the low solid volume fraction flows are suspected to arise from intermittency in this fluid layer (Figure 3.9a-b, 3.9d, 3.9i-j and 3.9l). The different optical texture of the fluid only flow may also lead to uncertainty in the PIV analysis of this region which is optimised for particle-laden areas.

By contrast, particles of 8×10^{-3} m, do not exhibit this fluid layer on top of the particle-laden flow. Even with a relatively high proportion of fluid present, these larger particles break through the surface to form a dry snout with a fully saturated tail (Figure 3.10).

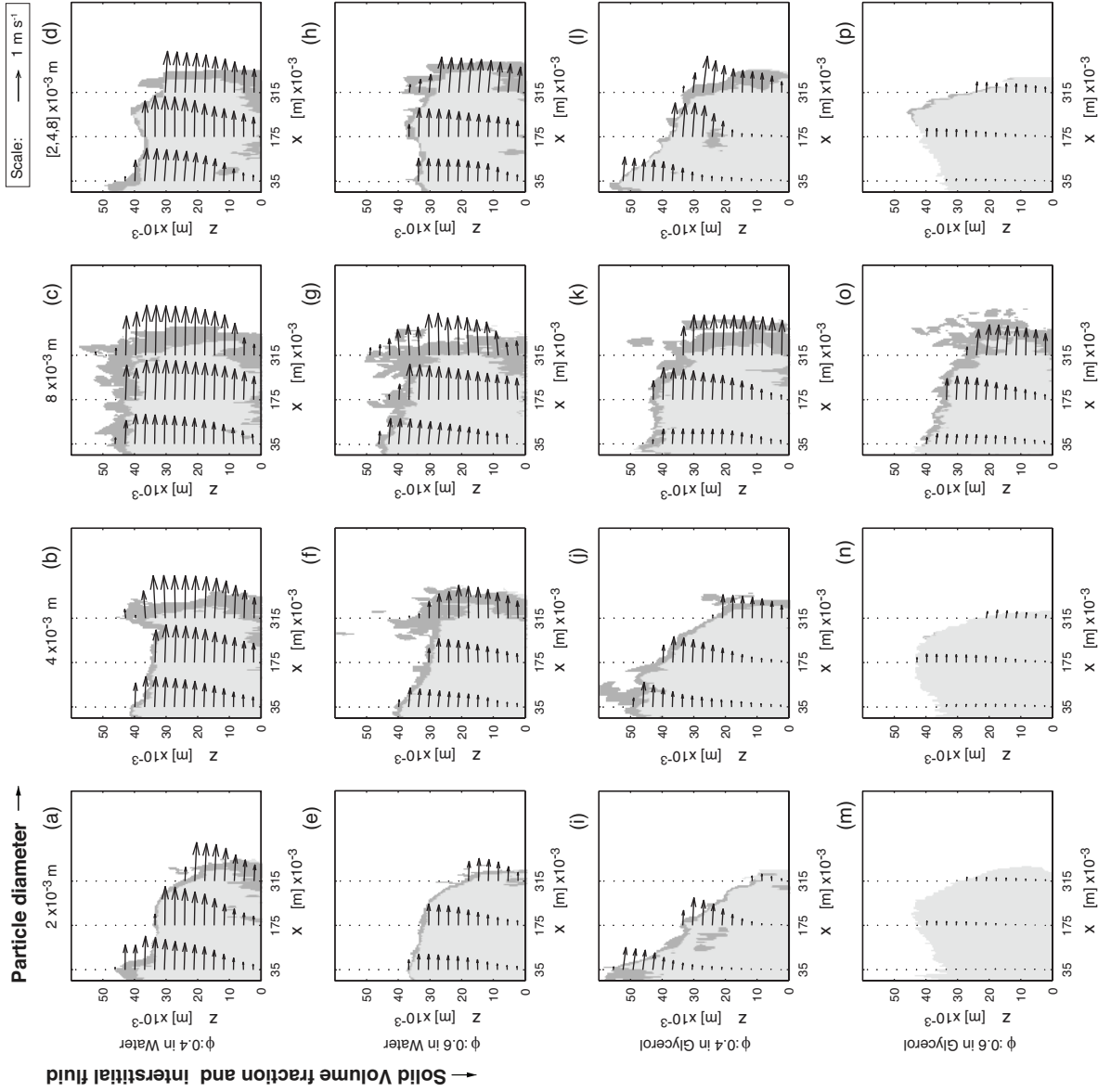


Figure 3.9. Colour map visualising regions of non-fluctuating and intermittent collisional behaviour through the flow depth y along the length of the flume x , at the flow front position $x_f = 350 \times 10^{-3}$ m with roughness element diameter 8×10^{-3} m. Columns are arranged by particle size, from mono-disperse 2×10^{-3} m to mixtures of 2×10^{-3} , 4×10^{-3} and 8×10^{-3} m particles. Rows are arranged by interstitial fluids (water and glycerol) and by solid volume fraction (0.4 and 0.6). Colour bar represents standard deviation from 14 frame average velocities in m s^{-1} , from blue (low standard deviation) to red (high standard deviation) with the same scale for the all flows. Dark blue represents non-fluctuating region of low granular temperature (standard deviation $\leq 150 \times 10^{-3} \text{ m s}^{-1}$). Colours from cyan, yellow, orange to red define the intermittent collisional behaviour (standard deviation $> 150 \times 10^{-3} \text{ m s}^{-1}$).

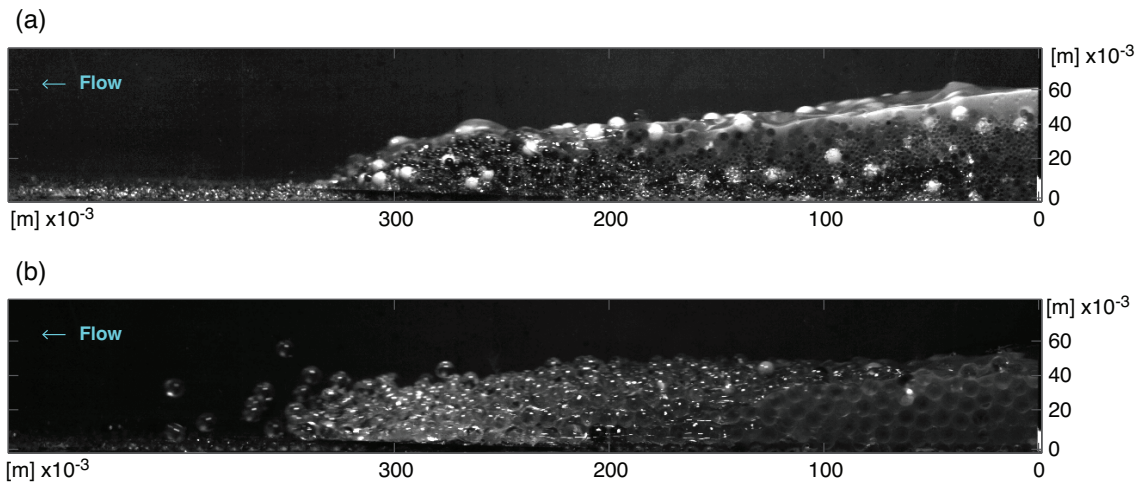


Figure 3.10. Side view of flows with solid volume fraction of 0.4, moving down a flume with at inclination 27° and a roughness element diameter of 8×10^{-3} m, consisting of 1 litre (a) mixed 2×10^{-3} (colourless), 4×10^{-3} (black) and 8×10^{-3} m (white) glass beads in glycerol. (b) 8×10^{-3} m glass beads in glycerol. In the poly-disperse case a fast moving layer of liquid forms at the top surface of the flow. For the mono-disperse flow, a dry granular front is formed followed by a saturated tail, with no fluid layer formed.

Front shape

Figure 3.11 illustrates the influence of solid volume fraction 0.4 and 0.6 with glycerol mixtures of the front shape. At first glance, the segmented images of the flows do not reveal contrasting behaviour. However, with 2×10^{-3} m particles with a solid volume fraction 0.4 (3.11a) the top of the flow shows a wave, resulting from the fluid layer trying to overpass the flow. This effect is observed with flows where small particles are present (e.g. Figure 3.11g) and is less clear in flows with 4×10^{-3} or 8×10^{-3} m particles only (Figure 3.11c and 3.11e).

3.2 Segregation

In the experimental flows which contain mixture of particles with different sizes (2×10^{-3} , 4×10^{-3} and 8×10^{-3} m), the larger particles accumulate at the front and on the top of the body of the flow as a result of size segregation (Figure 3.1). Deformation and dilation of the flow when moving down the flume under the action

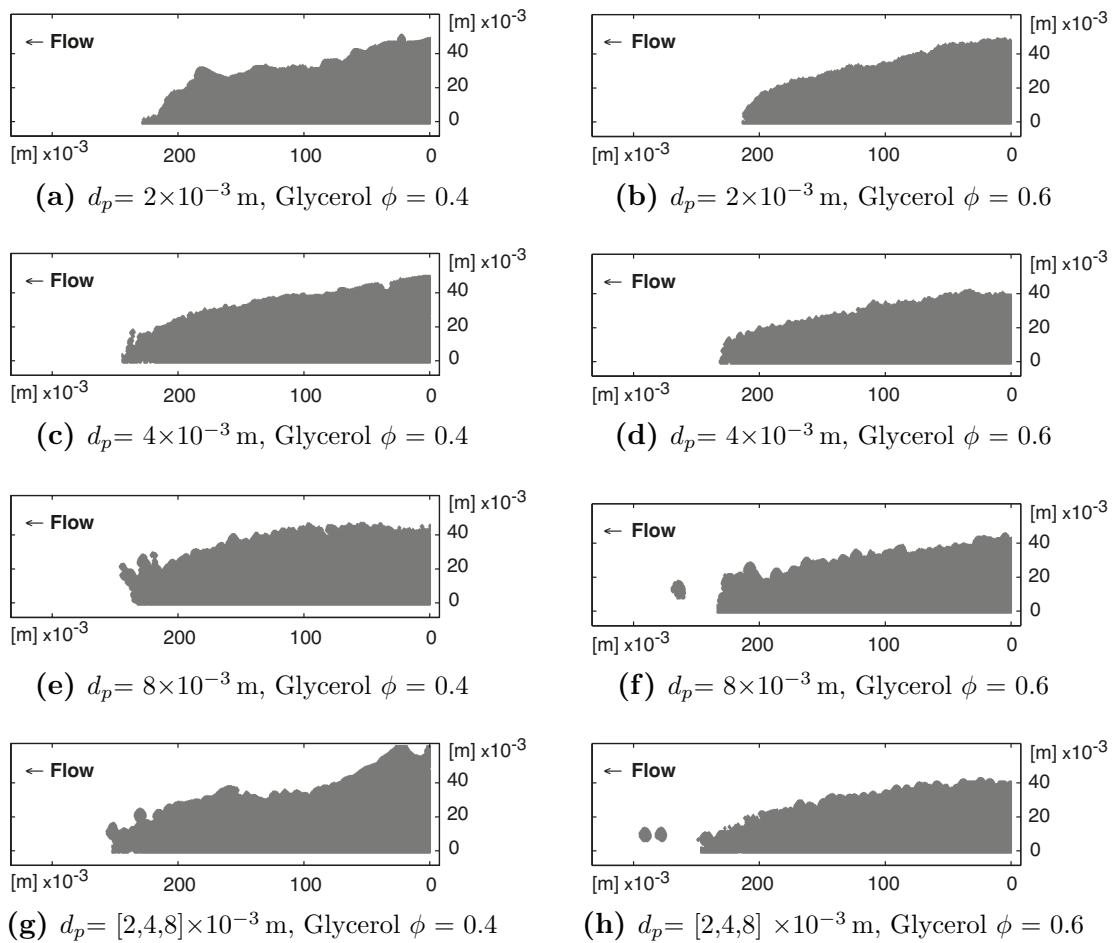


Figure 3.11. Shape of flow head in glycerol mixtures to different solid volume fractions. Columns are arranged by solid volume fraction 0.4 on the left and 0.6 on the right. Rows are sorted by particle size, from mono-disperse 2×10^{-3} m flows to mixtures of 2×10^{-3} , 4×10^{-3} and 8×10^{-3} m particles. The roughness element diameter of 8×10^{-3} m remained fixed.

of gravity, emerges from the fact that the particles must past one over another in order to shear.

Increases in granular temperature occurring particularly with high roughness element diameters, enhance the random fluctuations that constantly open up voids within the flowing mass. Under the action of gravity, this facilitates more the percolation of the smaller particles rather than the larger ones. Large particles are pushed upward near the flow surface and to the front of the flow [Ancy, 2012; Gray & Thornton, 2005; Iverson, 1997; Johnson *et al.*, 2012; Pouliquen & Vallance, 1999; Takahashi, 2007].

The measured velocity profiles (Chapter 4) show that velocity increases with

height in the flow. Thus, the top layers where the larger particles reside migrate to the front leading to a high concentration of large particles in the dry snout.

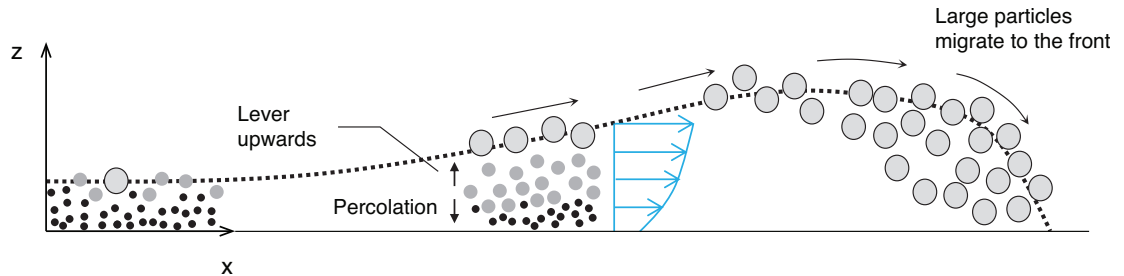


Figure 3.12. Schematic of particle size segregation in an experimental debris flows with mixtures of particles moving down an inclined flume. Small particles percolate into the random space to the base of the flume, surpassing larger particles in the upper layers. The velocity distribution shows the faster layers on the top. The large particles near the free surface, tend to migrate to the front of the flow.

Consequently, poly-disperse flows exhibit variation in particle concentration by size both vertically and along the flow. Segregation has been observed to varying degrees in all experiments with poly-disperse composition.

Roughness element diameter appears to play an important role, with segregation promoted with a decrease in the relative size of the particles and roughness element diameter (d_p/d_r). Increased roughness leads to enhanced particle fluctuations and reduced slip velocity at the bed, leading to a more marked velocity gradient (minimum at the bottom and maximum to the free surface) favouring the particle segregation mechanism.

The interstitial fluid of the mixtures noticeably influences the segregation mechanism. In the case of dry flows over very rough beds (i.e. $d_r = 8 \times 10^{-3}$ m), the segregation is very evident. However, for these dry poly-disperse flows a cloud of the small particles cohabits with larger particles in the front of the flow. As the flow moves down the flume, the front part seems to separate from the body, with the flow body slowing to a stop within the flume (see Figure 3.13).

Size segregation also occurs for the mixtures with water or glycerol. However, the presence of glycerol in the mixtures retards the segregation process, due to the

viscous forces.

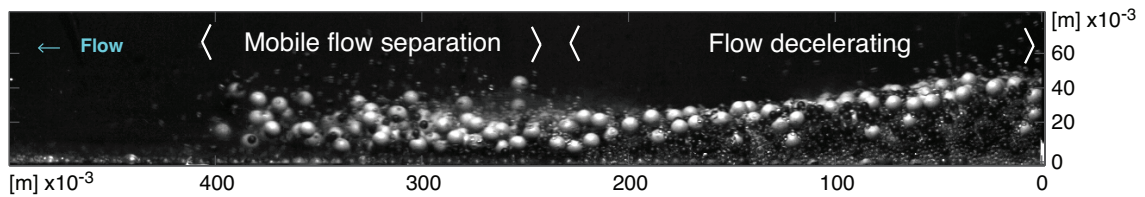


Figure 3.13. Particle size segregation in experimental flow of a dry mixture of particles from 2×10^{-3} (colourless), 4×10^{-3} (black) to 8×10^{-3} m (white) moving down a flume with a roughness element diameter of 8×10^{-3} m. Front of the flow, which contains high concentration of larger particles accompanied by a small particles cloud, separates from the body. The flow body decelerates to eventually stops within the flume.

3.3 Unsaturated flow front

A distinctive feature of the laboratory debris flows, regardless of particle size dispersion is that the front of the flow remained dry or unsaturated with zero or low pore pressure.

Figures 3.14 and 3.15 show the evolution in time of height (H), pore fluid pressure (P), normal (σ) and shear (τ) stresses corresponding to mono-disperse 2×10^{-3} m particles and a poly-disperse mixture respectively, at the sensor position (232×10^{-3} m from the gate). The flow height measurements show an abrupt front at the arrival of the flow at the sensor location. The normal stress readings¹ shows a simultaneous increase as the flow height¹. Both type of flows shows a lag in the pore fluid pressure, denoting an unsaturated flow front. Behind this relative dry front, the pore pressure increases asynchronously relative to the total normal stresses on the basal surface, until in the tail the flow is approximately hydrostatic ($P = \sigma$).

Large-scale debris flow experiments also exhibit the lag of the pore fluid pressure at the front flows [Iverson, 1997; Iverson *et al.*, 2010]. Similar to the present laboratory flows, the USGS large flume data reveal an heterogeneous architecture of the debris flow, where coarser particles are accumulated at the front of the flow, as

¹Note that the design of the gasket, with a watertight membrane covering, means that there is some uncertainty over the precise response time of the force plate to the flow front action.

consequence of size segregation, characterising the front with close to zero pore fluid pressure at the base. Size segregation has been suggested as the main mechanism leading to unsaturated flow fronts. However, crucially mono-disperse flows exhibit in our experiments the lag in pore fluid pressure, where size segregation plays no role (Figure 3.14). This striking characteristic found in mono-disperse flows will be discussed further in Section 4.1.1.

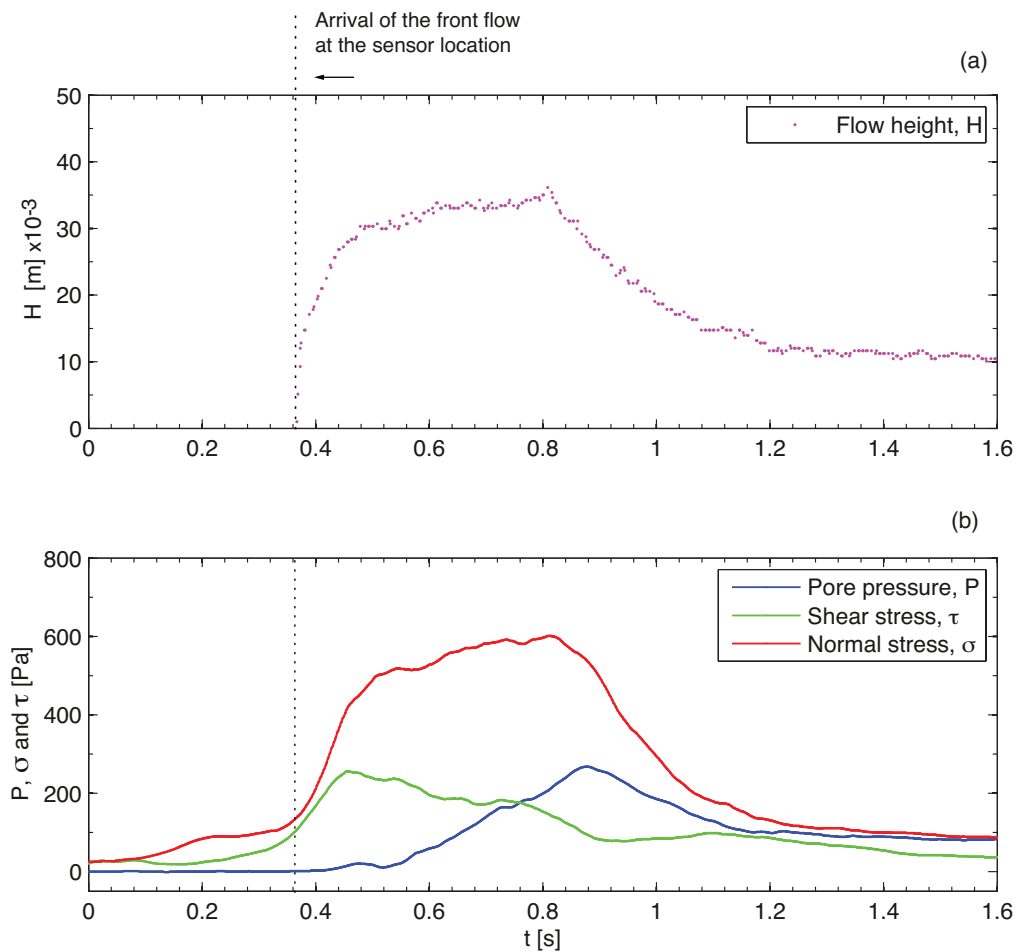


Figure 3.14. Time evolution of the (a) flow height H , and (b) pore pressure, normal and shear stresses at the sensor location, 232×10^{-3} m from the gate of the flume. The flow consists of 2×10^{-3} m particles with solid volume fraction 0.6 over 8×10^{-3} m rough element diameter. Arrival of the flow at $t = 0.37$ s.

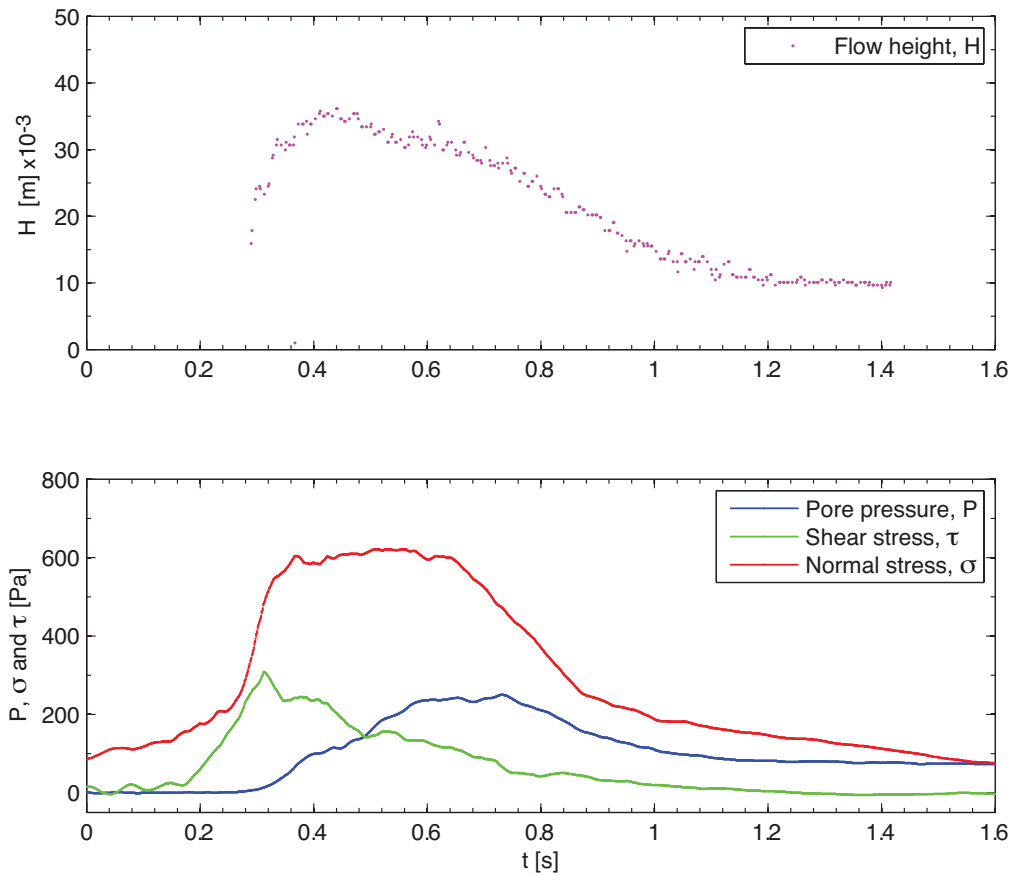


Figure 3.15. Time evolution of the (a) flow height H , and (b) pore pressure, normal and shear stresses at the sensor location, 232×10^{-3} m from the gate of the flume. The flow consists of mixed particles of 2×10^{-3} , 4×10^{-3} and 8×10^{-3} m with solid volume fraction 0.6 over 8×10^{-3} m rough element diameter. Arrival of the flow at $t = 0.28$ s.

3.4 Deposition

Deposition is the process by which particles leave the flow coming to a standstill to form distinctive solid patterns [Ancy, 2012; Gray & Thornton, 2005; Iverson, 1997; Iverson *et al.*, 2010; Johnson *et al.*, 2012; Pouliquen & Vallance, 1999; Takahashi, 2007]. It has been observed in the experimental flows that the deposition could occur (i) within the sloping flume without reaching the run-out tray, (ii) at the run-out tray, or (iii) as a combination of both, where only part of the flow reaches the run-out tray and the remaining flow remains in the flume channel.

The run-out area, when not laterally confined in the flume channel, the deposits formed peripheral boundary (levees) with generally a bulbous shape at the front (Figure 3.16). Formation of the lateral levees has been explained as a consequence of the size segregation process, where large particles migrate upwards and are transported to the flow front, pushed by nearly liquefied core and shouldered aside producing lateral levees [Iverson, 1997; Iverson *et al.*, 2010; Johnson *et al.*, 2012].

As the flow spreads in the run-out tray, the levees formed are some combination of lateral levees and depositing snout. However, levee have been observed, even with mono-disperse particles flows in the present work. Therefore an alternative mechanism to size segregation appears to be at work in the formation of lateral levees. Formation of levees in tests with round equal size particles flows have also observed [Félix & Thomas, 2004].

Field and large-scale laboratory experiments exhibited a dewatering process (e.g. Takahashi, 2007) during deposition, which is also observed in the present laboratory flows.

Variation in morphological characteristics of the deposit with roughness element diameter (Figure 3.17), interstitial fluid (Figures 3.18 and 3.19) and solid volume fraction (Figures 3.19 and 3.20) are discussed.

It has not been possible to measure all the run-outs of each experiment: extremely long trays would be required to be able to cover the parameter range tested (e.g. flows running over very smooth surface or high liquid content).

Roughness element seems notably to influence the shape and total length of the deposit (e.g. 2×10^{-3} m particles mixtures 3.17a-d). Fixing the solid volume fraction of 0.6 and the interstitial fluid as water, when flows are running over smooth surface (0 m roughness, 3.17a) the deposit has an elongated shape with a rounded front. As the roughness element diameter increases, the deposit length is reduced to become a horseshoe shape (Figure 3.17b). With high roughness element diameter (4×10^{-3} and 8×10^{-3} m, 3.17c-d respectively), sideways spreading is enhanced, leaving a semicircular pattern. This result contradicts Iverson *et al.* [2010], where bed roughness reduce the flow front speeds but not total run-out distances during deposition. However, when flows contain a mixture of particle sizes, the run-out seems

not to increase with the roughness element diameter (Figure 3.17m-p).

The role of interstitial fluid is conspicuous in the shapes and run-out distance of the deposits (Figure 3.18). When the laboratory flows pass over a 8×10^{-3} m roughness element diameter, the dry flows have elongated shape and long run-out distance, stopping only at the end of the tray. Adding fluid to the flows, the shape becomes more rounded and decreases the run-out distance (e.g Figures 3.18a-c.). Increasing the viscosity of the fluid (i.e. dry-water-glycerol), shapes become more rounded and shorter run-out distance are observed.

Increasing the proportion of fluid in the flow enhances flow mobility, reaching longer run-out distances (Figure 3.19) even with glycerol (Figure 3.20). Note that the flows all contain the same volume of solids (1 litre) and the solid volume fraction varies from 0.7 to 0.4. Thus adding more fluid to the mixture, increases the total volume of the flow for which, longer run-out distances can be expected [Legros, 2002b].

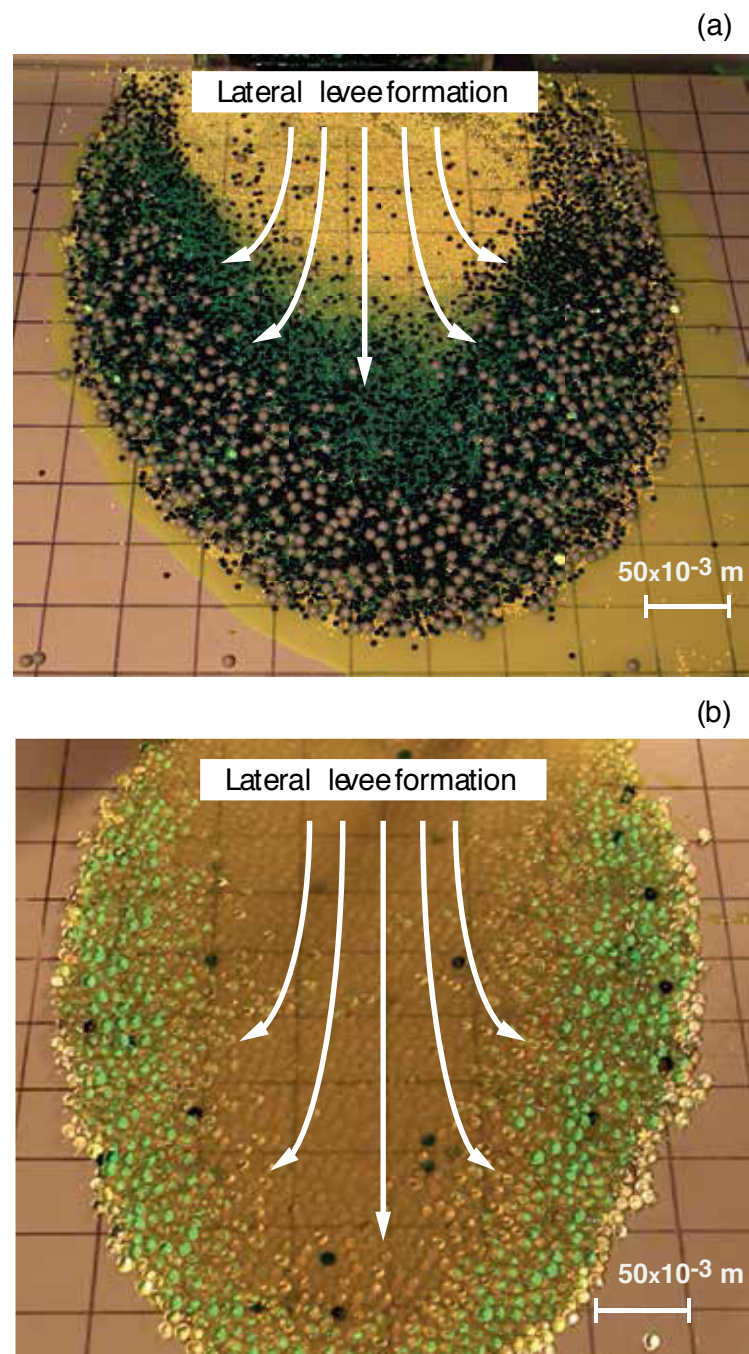


Figure 3.16. Front camera images of the experimental flows run-out showing formation of lateral levees (a) with poly-disperse particles from 2×10^{-3} , 4×10^{-3} to 8×10^{-3} m to solid volume fraction 0.6 with water and (b) with mono-disperse of 8×10^{-3} m particles, to solid volume fraction 0.4 with glycerol. Liquefied core material is observed in the central region and accreted particles around the perimeter of the flow. Roughness element fixed to 8×10^{-3} m at the flume. Smooth run-out tray surface.

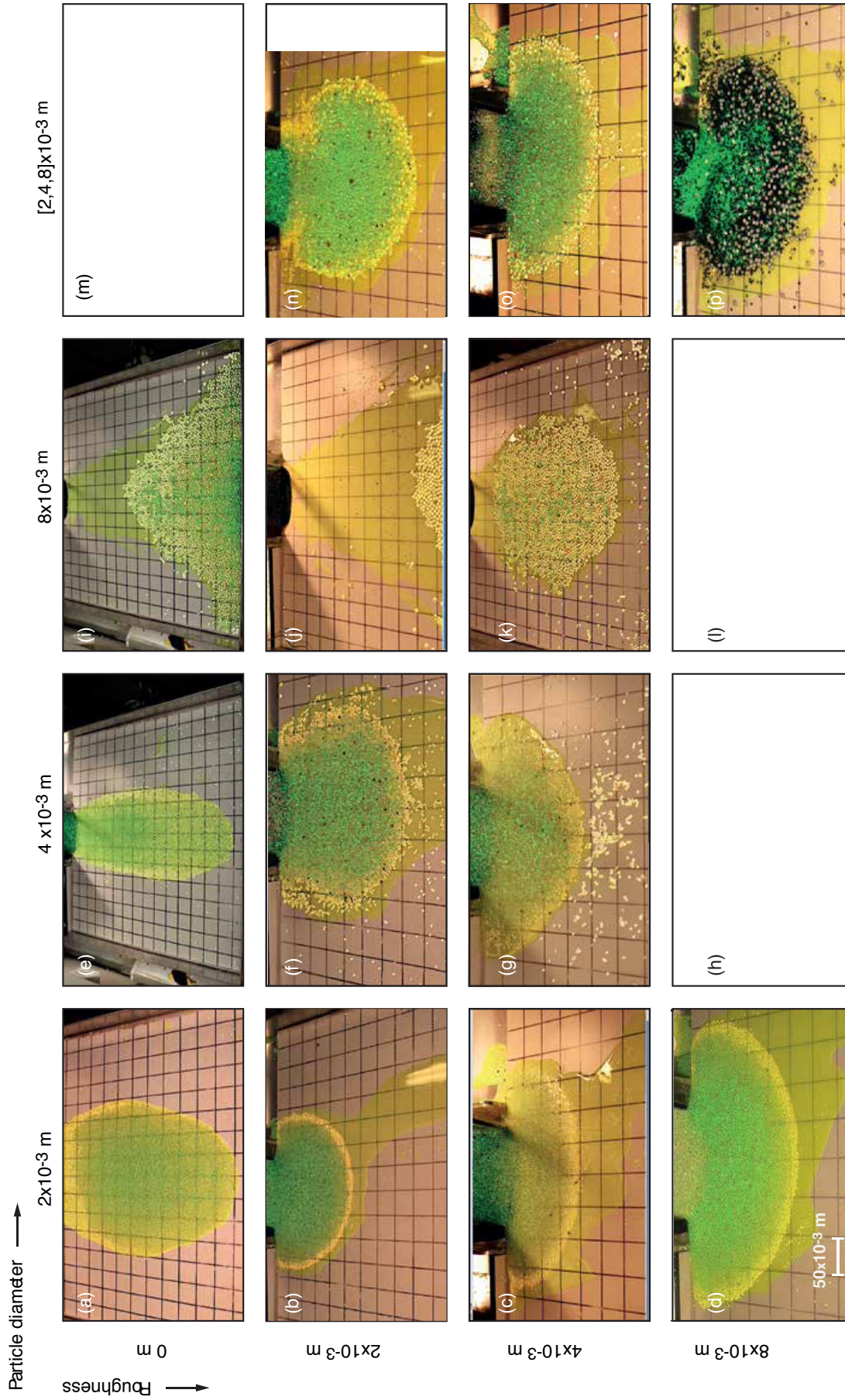


Figure 3.17. Deposits of laboratory debris flows showing variations with roughness element diameter and particle size in the flows. Columns are arranged by particle size, from mono-disperse $2 \times 10^{-3} \text{ m}$ flows to mixtures of 2×10^{-3} , 4×10^{-3} and $8 \times 10^{-3} \text{ m}$ particles. Rows are arranged by roughness element diameter of 0 , 2×10^{-3} , 4×10^{-3} and $8 \times 10^{-3} \text{ m}$. Flows consist of particles mixed in water with solid volume fraction 0.6 and with a smooth run-out tray surface.

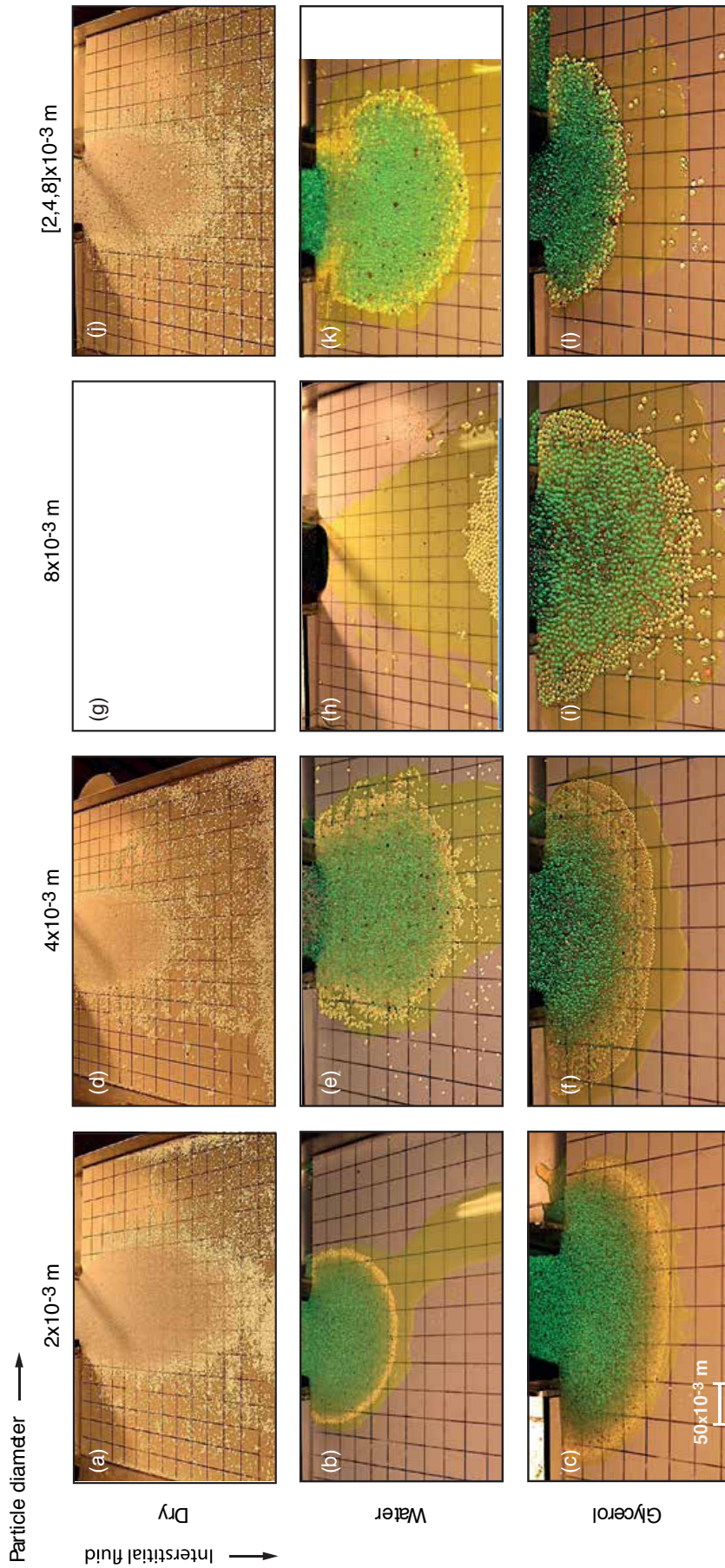


Figure 3.18. Deposits of laboratory debris flows varying with interstitial fluid. Columns are arranged by particle size from mono-disperse 2×10^{-3} m flows to mixtures of 2×10^{-3} , 4×10^{-3} and 8×10^{-3} m particles. Rows are arranged by type of interstitial fluid: dry, water or glycerol. The roughness element diameter of 2×10^{-3} m, volume fraction 0.6 and smooth run-out tray surface are the same for all flows.

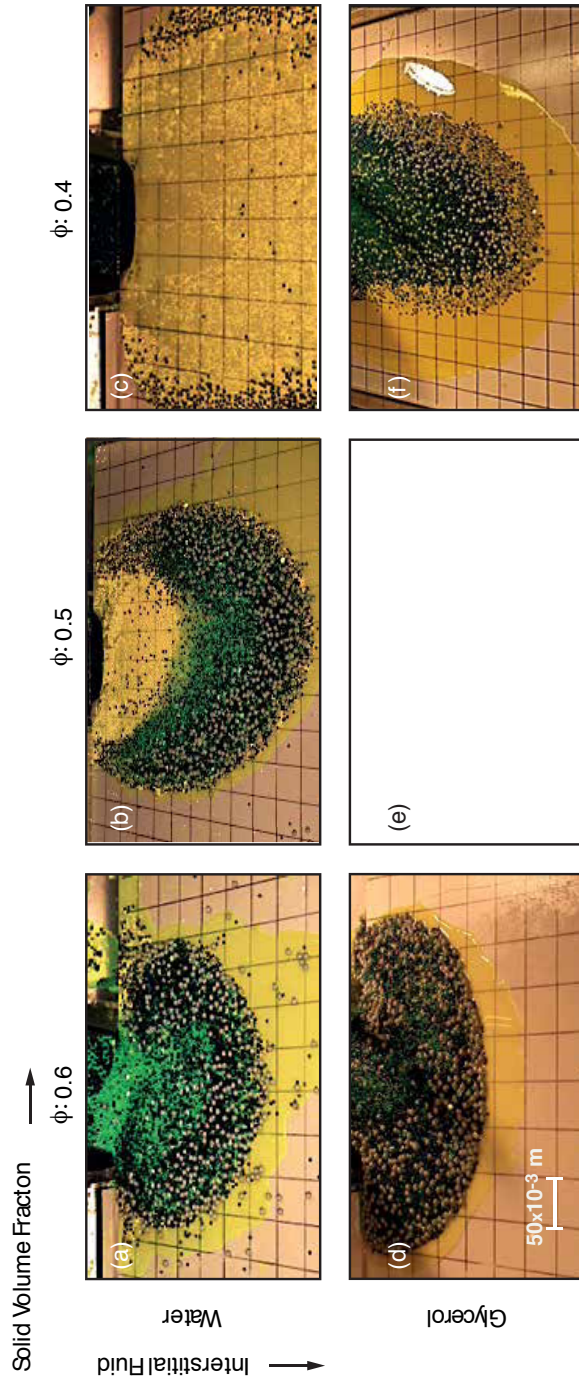


Figure 3.19. Deposits of laboratory debris flows consisting of 1 litre of mixed 2×10^{-3} (colourless), 4×10^{-3} (black) and 8×10^{-3} m (white) particles. Columns are arranged by particle solid volume fraction: 0.4 (maximum fluid content), 0.5 and 0.6 (minimum fluid content). Rows are arranged by type of interstitial fluid, water or glycerol. The roughness element diameter of 2×10^{-3} m and smooth run-out tray surface are the same for all flows.

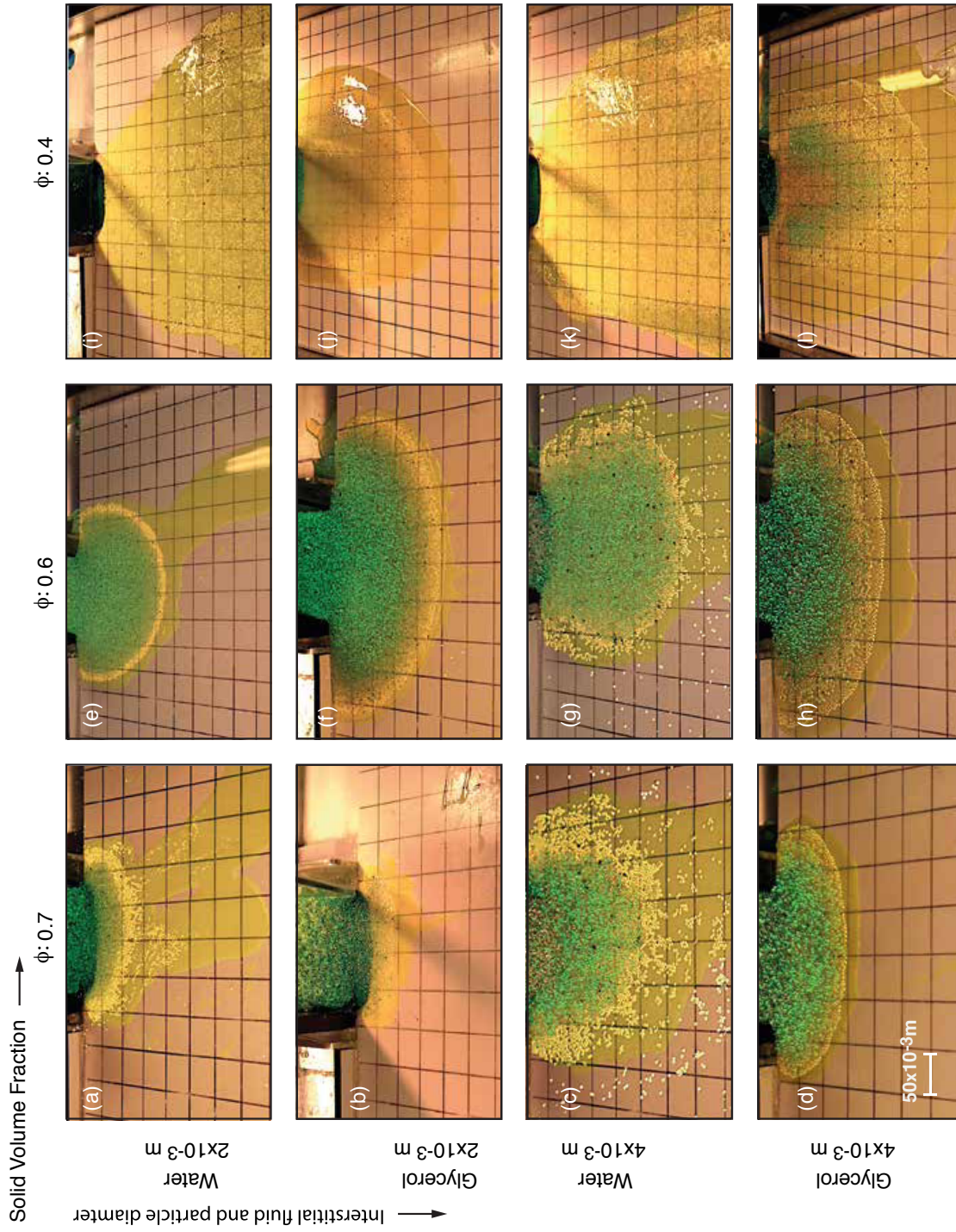


Figure 3.20. Deposits of laboratory debris flows consisting of 1 litre of mixed of particles. Columns are arranged by solid volume fraction, 0.7, 0.6 and 0.4. Rows are arranged by particles with 2×10^{-3} or 4×10^{-3} m diameter and interstitial fluid water or glycerol. The roughness element diameter of 2×10^{-3} m and smooth run-out tray surface are the same for all flows.

3.5 Conclusions

Laboratory debris flow showed two coexisting regions, based on the standard deviation of the velocities from the local averages. The extended regions of non-fluctuating and intermittent collisional behaviour and flow form are mediated by the flow composition and the roughness element diameter, with the subsequent influence on flow velocities, heights, run-out distance and deposition patterns.

Results from small scale laboratory debris revealed morphological characteristics similar to full-scale debris flows, providing systematic data for validating and calibrating new constitutive models of debris flows.

Chapter 4

Experimental results

Debris flow models require a constitutive law to accurately deal with evolving rheologies (in space and time) within the same event, to be able to predict flow height, velocity profiles and run-out distances and shapes [Ancey, 2012; Bartelt *et al.*, 2012; Buser & Bartelt, 2009; Iverson, 1997, 2012; Iverson *et al.*, 2010; Kaitna & Rickenmann, 2007; Pudasaini, 2012; Takahashi, 2007]. The evolution of the laboratory debris flows described in Chapter 2 and 3 are analysed here to understand how flow composition and surface roughness influence the key dynamic parameters. The evolution of the flow was captured with high speed video, and PIV analysis provided velocity profiles through the flow depth, from nose to tail. Shear stress and normal stress and fluid pore pressure were measured at the basal surface.

On opening the gate an unsteady, deforming flow surges down the rough inclined flume, with flow heights in the range 0.025–0.045 m and front velocities 0.5–1.5 m s⁻¹.

4.1 Flow evolution

The evolution of the flow time as it passes the sensor location (Figure 4.1) was investigated, and the influence of particle size (Figures 4.2 and 4.3) interstitial fluid (Figure 4.7) and solid volume fraction (Figure 4.11) assessed.

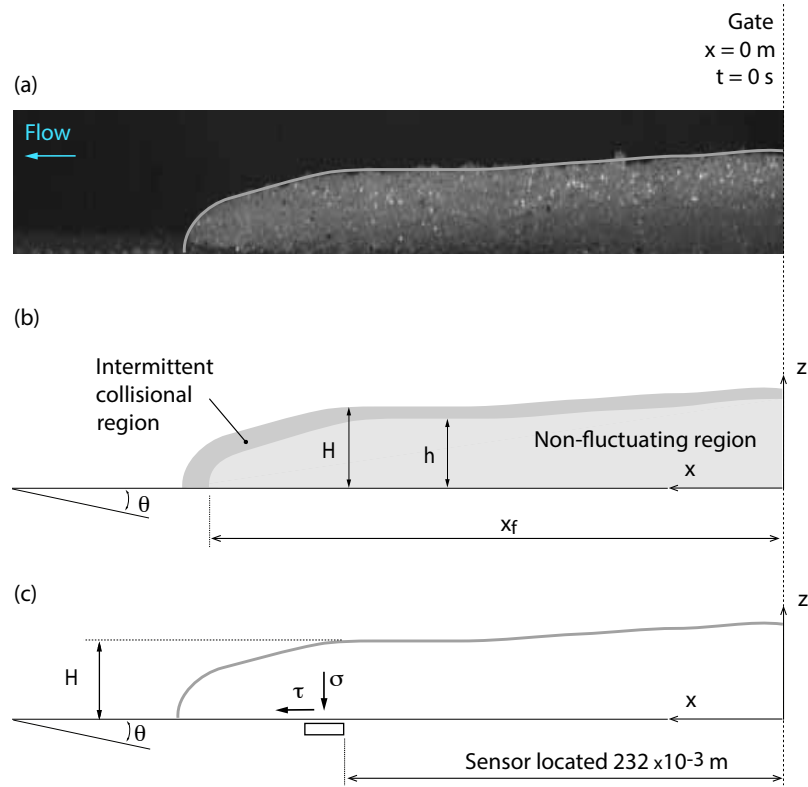


Figure 4.1. (a) Edge of the flow superimposed on the side view of a laboratory experimental flow. On the right of the image the gate is located corresponding to $x = 0$ m and $t = 0$ s. (b) Schematic of the flow showing the the pseudo-plug and intermittent collisional regions, shaded light and dark grey respectively. The characteristic flow height and front flow position are defined by the pseudo-plug region as h and x_f respectively. The total flow height H includes the extend of the intermittent collisional region. (c) Sensor position and σ normal stress and τ shear stress.

A two-component force plate (x, z) and a pore pressure sensor, located 232×10^{-3} m from the gate, measured σ basal normal and τ shear stress and pore fluid pressure P (Figures 4.2b,g, 4.3b,g, 4.7b,g,l and 4.11b,g).

Image analysis and PIV processing (see Section 2.4) provided two-dimensional velocity profiles $u(x, z, t)$ from the front of the flow to the tail, the total flow height $H(x, t)$ which refers to the flow height including the intermittent collisional region and $h(x, t)$ the characteristic flow height corresponding to the flow within the pseudo-plug region (Figure 4.1).

Total flow height $H(x, t)$ and the equivalent height of fluid pressure $h_\Psi(x, t)$

defined as

$$h_{\Psi} = \frac{P}{g\rho_{fi} \cos \theta}, \quad (4.1.1)$$

where g is the gravity acceleration, and ρ_{fi} is the density of the interstitial fluid with $i = (1, 2)$ for water and glycerol respectively, are illustrated in Figures 4.2a,f 4.3a,f, 4.7a,f,k and 4.11a,f.

The slip velocity u_{slip} and free surface velocity u_t were calculated from the slope normal profile velocities. The mean velocity u_m was estimated using the depth-average velocity defined as

$$u_m = \frac{1}{H} \int_0^H u(z) dz, \quad (4.1.2)$$

the time evolution of which is shown in Figures 4.2c,h, 4.3c,h, 4.7c,h,m and 4.11c,h.

The variation of shear to normal stress ratio in time is shown in Figures 4.2d,i, 4.3d,i, 4.7d,i,n and 4.11d,i.

Bulk density ρ_s was estimated from the ratio of normal stress σ to the total flow height H [Iverson, 1997; McArdell *et al.*, 2007] as

$$\rho_s = \frac{\sigma}{gH \cos \theta}. \quad (4.1.3)$$

The apparent average mass density of the fluid phase ρ_{af} was calculated assuming that the height of the fluid phase is the same as the total flow height [McArdell *et al.*, 2007] as

$$\rho_{af} = \frac{P}{gH \cos \theta}. \quad (4.1.4)$$

Figures 4.2e,j, 4.3e,j 4.7e,j,o and 4.11e,j showed the calculated bulk mass densities.

4.1.1 Effect of particle and roughness element diameters

To assess the influence of particle size, the dynamic flow data sets are shown for mono-disperse 2×10^{-3} , 4×10^{-3} m and 8×10^{-3} m and poly-disperse $[2,4,8] \times 10^{-3}$ m flows,

in water to a solid volume fraction 0.6 over 8×10^{-3} m roughness diameter element in Figures 4.2a-j and 4.3a-j.

The height and normal stress ¹ measurements of the flow shows a synchronous evolution; an abrupt flow arrival is followed by a gradually decreased height of the flow. The correlation coefficient of these two variables reflects the strong positive correlation with values ranging from 0.71 to 0.99. However, the pore fluid pressure responds with a lag compared with the stress measurements. The lack of pore fluid pressure at the front of the flow occurs as a consequence of the unsaturated flow which was observed in both mono-disperse and poly-disperse mixtures (Section 3.3). As the flows saturate, pore fluid pressure gradually increases, tending to the normal stress values $\sigma \approx P$ (Figures 4.2a-b,f-g and 4.3a-b,f-g).

Nonetheless, the shear stress changes asynchronously to the pore fluid pressure. It appears that the pore fluid has a strong influence on the friction. As soon as the pore fluid pressure emerges the shear stress starts to decrease. Subsequently, the basal effective friction coefficient $\mu = \tau/\sigma$ is reduced too (Figures 4.2d,i and 4.3d,i).

In addition, pore fluid pressure appears to influence the flow velocity. The time series of the velocities sometimes reveal a delay in the process of deceleration, or even a slight increase, in the flow velocity as the pore fluid pressure peaks (Figures 4.2c,h and 4.3c,h), enhancing flow mobility as found by other researchers [Iverson, 1997; Iverson *et al.*, 2010; McArdell *et al.*, 2007].

Figures 4.2e,j and 4.3e,j show flow regime transition and variations of the bulk density. The bulk density seems to drop at the edge of the flow front as a consequence of a volume expansion due to the particle fluctuations and subsequently granular agitation.

The evolution of the flow velocities reveal at the edge of front $u_t = u_m = u_{slip}$ with the highest velocities, decreasing rapidly until the pore fluid is presented in the flow (indicated by the pore fluid pressure) and then reaches a constant velocity (Figure 4.2c) or decreases less rapidly (Figure 4.2h and 4.3c), or even increases (Figure 4.3h) before decreasing towards a plug-like at the tail of the flow ($u_t \simeq u_{slip}$).

¹Note that the design of the gasket, with a watertight membrane covering, means that there is some uncertainty over the precise response time of the force plate to the flow front action.

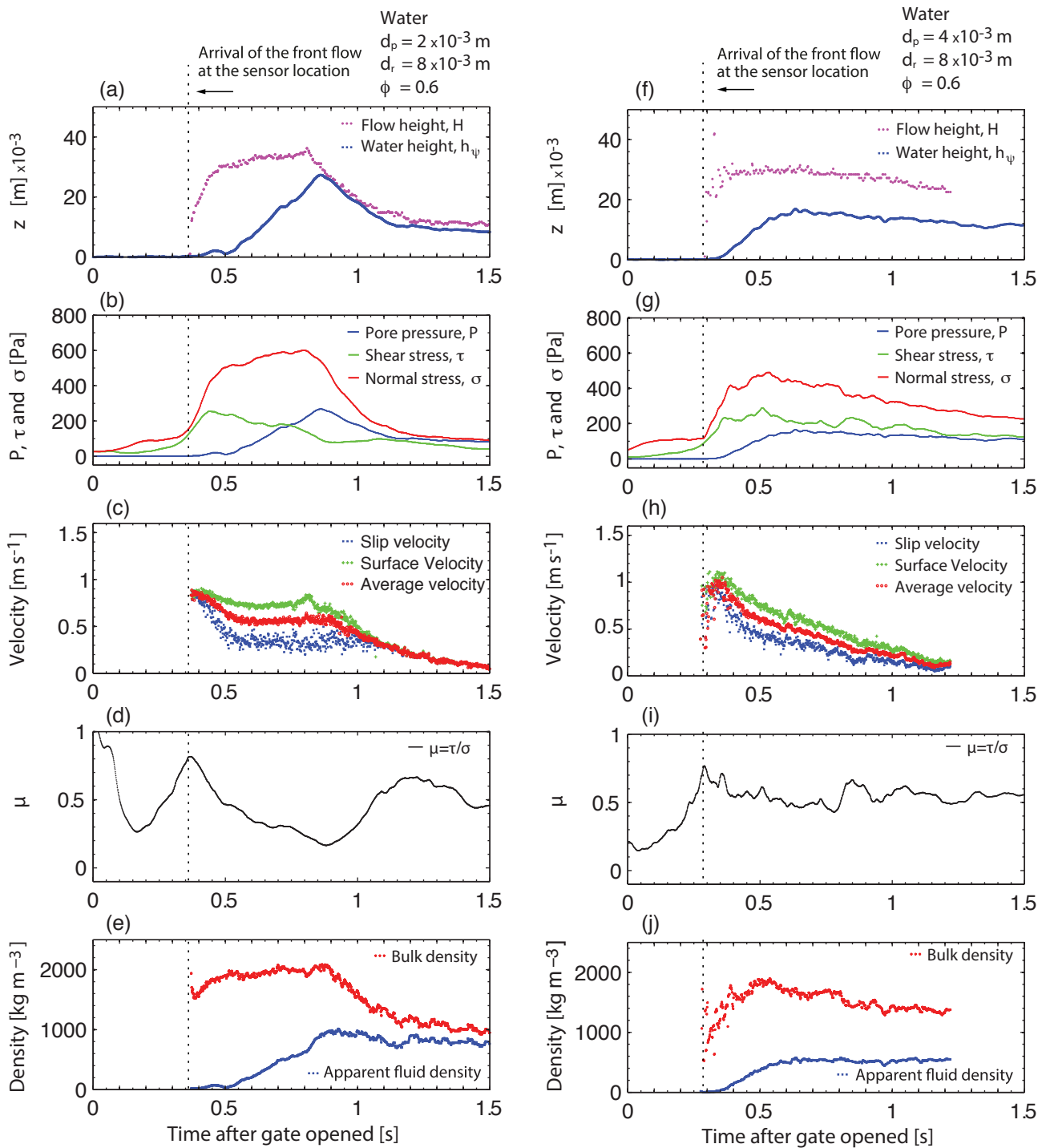


Figure 4.2. Flow evolution from the arrival of the flow to the sensor located at $232 \times 10^{-3} \text{ m}$ from the gate of water flow mixtures with solid volume fraction 0.6 over $8 \times 10^{-3} \text{ m}$ roughness element diameter of mono-disperse (a-e) $2 \times 10^{-3} \text{ m}$ and (f-j) $4 \times 10^{-3} \text{ m}$ particles diameter.

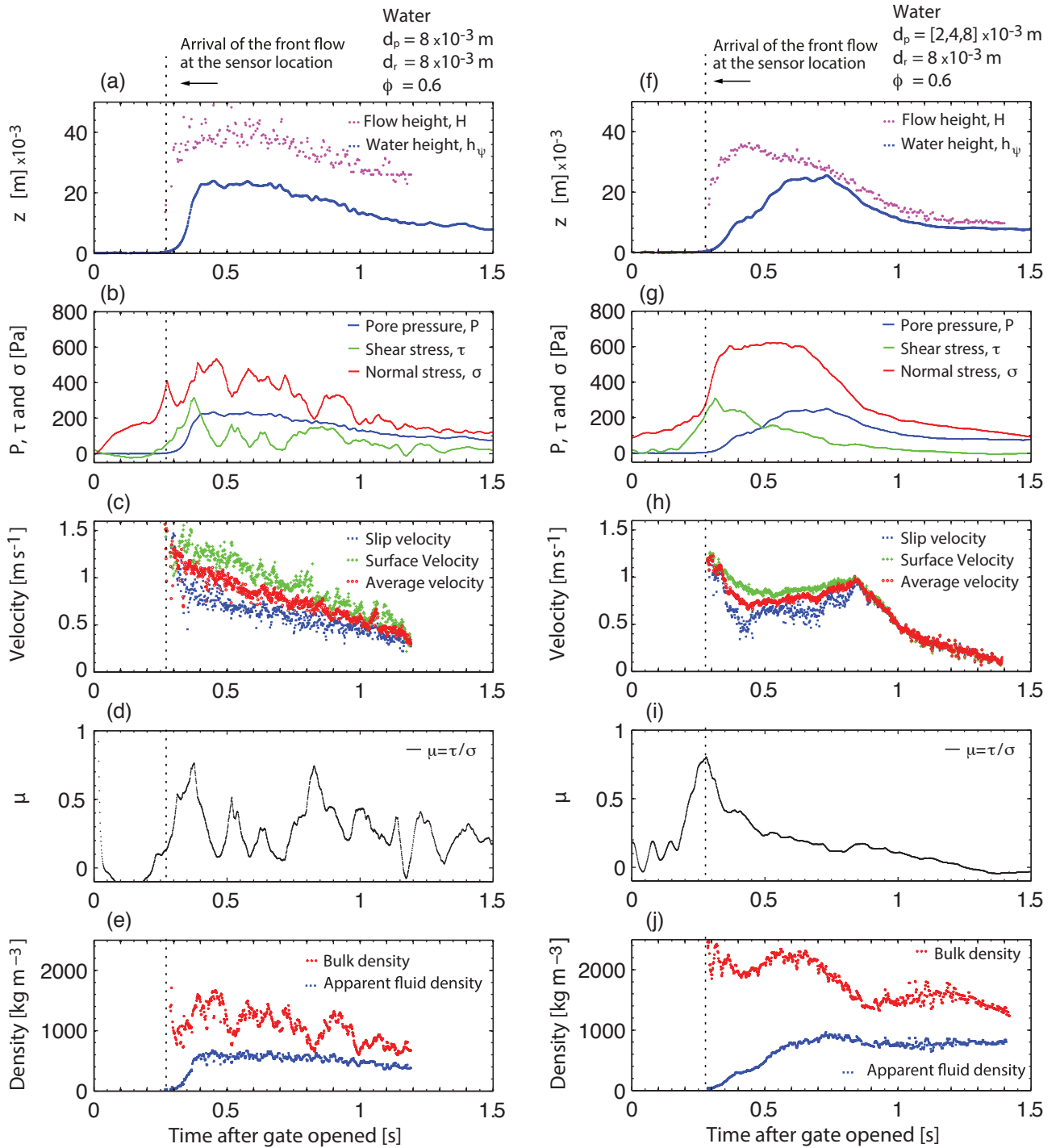


Figure 4.3. Flow evolution from the arrival of the flow to the sensor located at 232×10^{-3} m from the gate of water flow mixtures with solid volume fraction 0.6 over 8×10^{-3} m roughness element diameter of (a-e) 8×10^{-3} m and (f-j) 2,4 and 8×10^{-3} m particles diameter.

Velocity distributions

The evolution of the flow behaviour through the flow depth for different flow conditions is described with an averaged velocity profile $u(z)$ within the pseudo-plug region (defined in Chapter 3) at 50% flow length from the front (Figures 4.4, 4.8, and 4.12). Throughout the pseudo-plug region, the depth of the flow z and the down slope velocity u are normalized by the maximum height h_{max} and the maximum velocity u_{max} respectively.

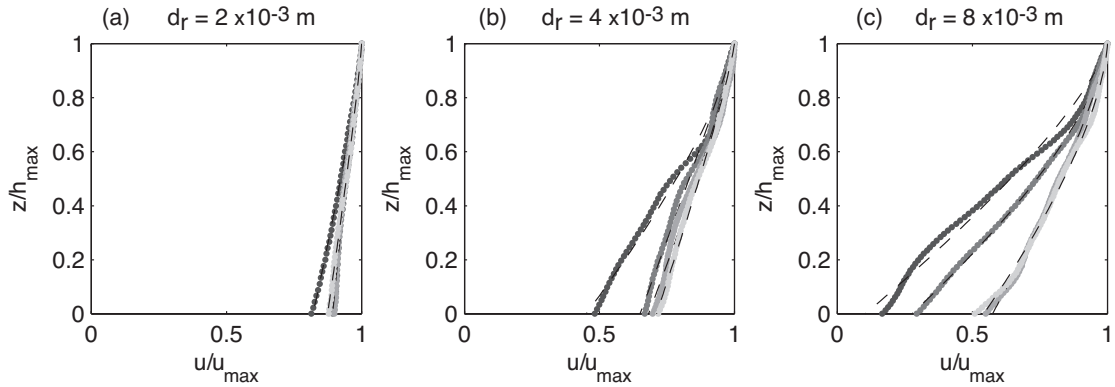


Figure 4.4. Average velocity profiles within the pseudo-plug region at 50% flow length from the front. Flows consist in particles mixed in water to a solid volume fraction of 0.6 for different roughness element diameters from (a) 2×10^{-3} m, (b) 4×10^{-3} m to (c) 8×10^{-3} m. Dashed black lines represents the fit power law (Equation 4.1.5). The particle diameter of the experimental flows is represented by the grey lines becoming lighter by increasing particle diameter from 2, 4, 8×10^{-3} m and poly-disperse mixture with a mean diameter of 4×10^{-3} m.

To quantify the characteristics of the flow and to be able to estimate the slip velocity and velocity profiles shapes, a power-law profile has been fitted to the average profiles at 50% flow length from the front within the pseudo-plug region

$$u(z) = u_{max} + (u_{slip} - u_{max}) \left(1 - \frac{z}{h_{max}}\right)^{\beta}, \quad (4.1.5)$$

where u_{slip} denote the slip velocity at the basal surface and β is the exponent of the distribution. This power law was fitted to the experimental data using a least square optimisation method to find the unknown variables u_{slip} and β . As a reference, for Newton fluids, in which the shear stress is linearly proportional to the rate of strain, the velocity profiles follow a $\beta = 2$ power law and for granular flows,

where stress become rate dependent, the velocity profiles fit a 3/2 power law being known as Bagnold velocity profile the latter one Takahashi [1991]. Table 4.1 gives the optimized slip velocity (u_{slip}/u_{max}) and exponent β and their residuals ($< 3\%$) fitted for the experimental velocity profiles corresponding to a mixture with water to a solid volume fraction 0.6 varying particles sizes and roughness element diameter.

Roughness $d_r \times 10^{-3}$ [m]	Particle size $d_p \times 10^{-3}$ [m]	Slip velocity u_{slip}/u_{max}	β	Residual %
2	2	0.82	1.21	0.2
2	4	0.89	1.00	0.3
2	8	0.89	0.91	0.4
2	[2,4,8]	0.87	1.16	0.2
4	2	0.45	1.35	1.8
4	4	0.65	1.06	1.0
4	8	0.68	1.20	1.3
4	[2,4,8]	0.71	1.15	0.7
8	2	0.10	1.32	2.9
8	4	0.28	1.47	0.8
8	8	0.57	1.28	0.7
8	[2,4,8]	0.54	1.51	1.0

Table 4.1. Optimised fit parameters for power law velocity profiles (Equation 4.1.5) for different particle sizes and roughness element diameters.

Characteristic flow depth measurements of the local average velocity show a strong dependence on roughness element and particle diameter. For the smaller roughness element, independent of the particle size of the flow, the flow at the bottom exhibits high slip velocities with very low velocity gradient through the flow depth. The flow moves smoothly as a ‘plug’ (Figure 4.4a). Increasing the roughness element diameter, the slip velocity decreases concurrently with an increase in velocity gradient through the depth (Figure 4.4b and 4.4c).

The relative size of the flow particles and roughness element diameter (d_p/d_r) appears to strongly influence the slip velocity. For ratios must exceeding a threshold value of $d_p/d_r \geq 1$ the slip velocity appears independent of the particle size. However for $d_p/d_r < 1$, decreasing particle sizes lead to a reduction in slip velocity.

For $d_p/d_r < 1$, the velocity distribution can have slight inflection points, and the greatest velocity gradient does not appears at the bottom of the flow. This could happen since small particles can be trapped when flow passes on a basal surface

with large roughness element diameters (Figure 4.5).

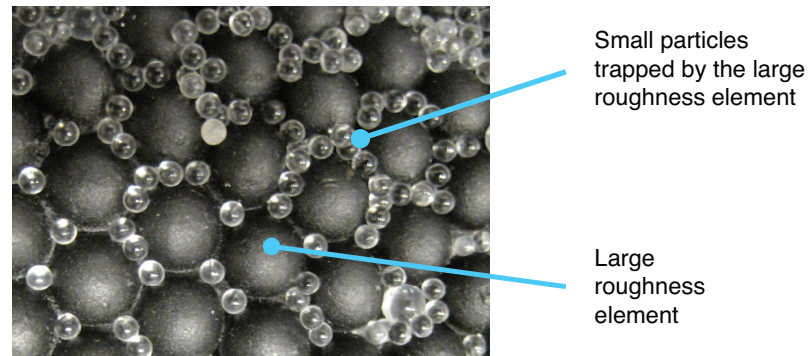


Figure 4.5. Top view of small particles trapped between the large roughness element.

Flow heights and front velocities

The evolution in time of the flow heights and front flow positions versus roughness element diameter are summarized in Figure 4.6, for mixtures of flows with water to a solid volume fraction of 0.6.

With increase in roughness, the flows become slower and reach greater heights for the 2×10^{-3} m particle size flows shown in Figure 4.6a and 4.6e. The higher friction at the base of the flow inhibits the sliding of the flow, retarding the whole flow and consequently increasing the depth of the flow. Noting that the front propagation with 4×10^{-3} and 8×10^{-3} m roughness is practically at the same speed. This could be owing to small diameter of the 2×10^{-3} m particles compared to the large particles of 8×10^{-3} m. The small particles are trapped between the large gaps, transforming into an equivalent smoother surface (Figure 4.5).

As the relative size of particles and roughness $d_p/d_r \geq 1$, the dependence of the flow front speed with the roughness element seems to be less conspicuous (Figure 4.6c and 4.6g).

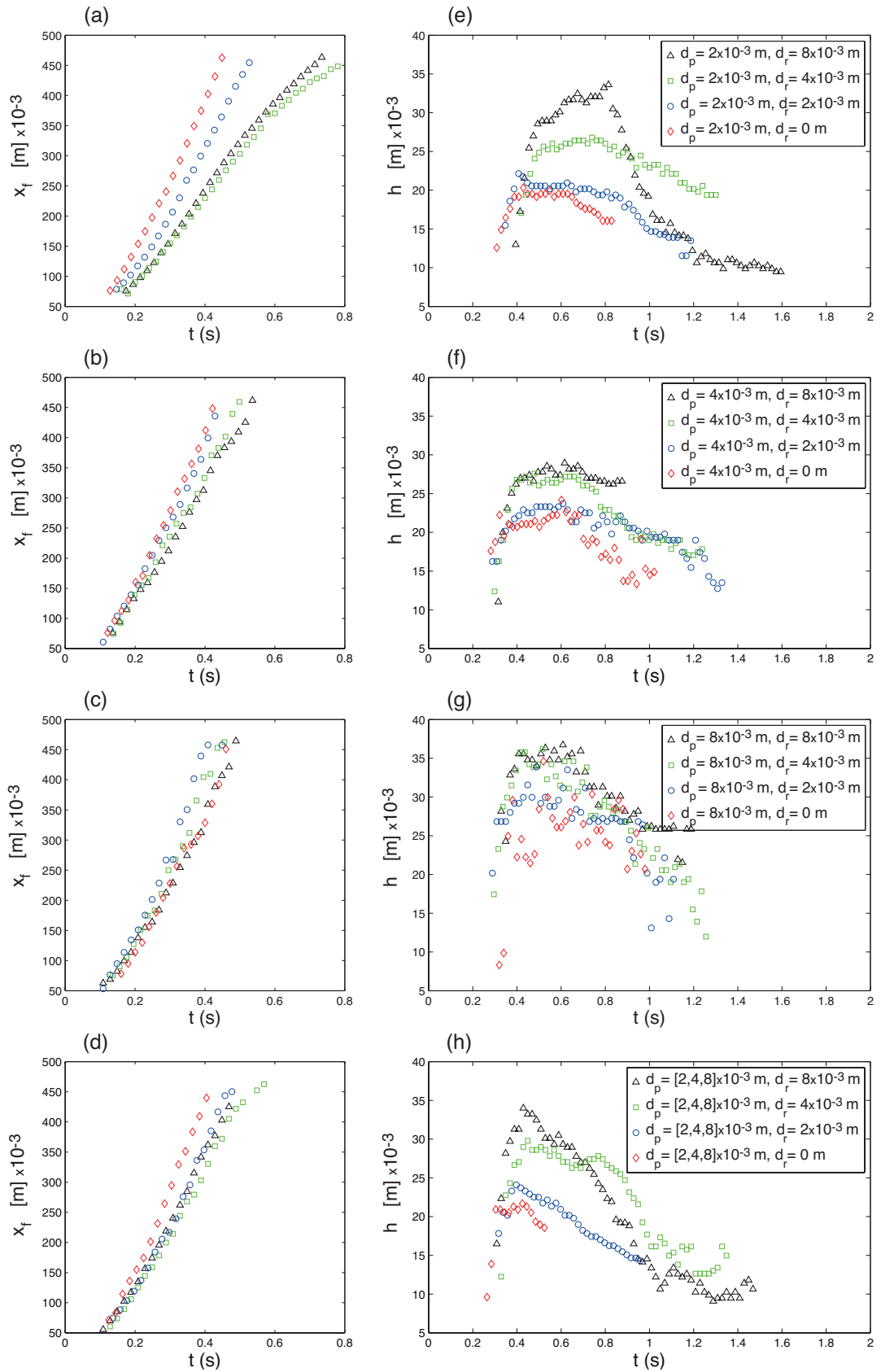


Figure 4.6. Time dependence of front position x_f (a-d) and height of the flow h (e-f). Rows are arranged by particle size, from mono dispersed 2×10^{-3} m flows to mixtures of 2×10^{-3} , 4×10^{-3} and 8×10^{-3} m particles versus roughness element diameter from 0, 2×10^{-3} , 4×10^{-3} and 8×10^{-3} m. Flows consist of particles mixed in water to a solid volume fraction of 0.6. The flow heights and velocities front are considered within the pseudo-plug region.

4.1.2 Effect of interstitial fluid

Flow quantities are examined for three mono-disperse 2×10^{-3} m particle flows varying with interstitial fluid: dry, water or glycerol with solid volume fraction 0.6 over 8×10^{-3} m roughness element diameter (Figure 4.7).

A very rapid expansion of the flow volume is observed in the dry particle flow at the front. The dispersive pressure originated by the particle interactions with the rough surface [Buser & Bartelt, 2011a] causes that a pronounced increase of the total height of the flow H (Figure 4.7a) and subsequent density decrease (4.7e). When the interstitial fluid is water or glycerol, the volume expansion is still observed but less markedly.

The normal basal stress changes in-phase with the total height of the flow (Figure 4.7a,f,k and 4.7b,g,l) with a correlation coefficient higher than 0.99 with water or glycerol as interstitial fluid. The dry flows, at the front of the flow where the flow exhibits a cloud of collisional and saltating particles, does not have positive correlation. However after 0.4 sec, when the flow moves in masse manner, the normal stress and height has a correlation coefficient of 0.86. The pore fluid pressure with glycerol as interstitial fluid also shows a lag. Note the large value of the lag is also affected by the position of the pore pressure sensor and the slow speed of the flow (further explanation in section 2.3). The shear stress evolves asynchronously relative to the pore fluid pressure.

The mixture with glycerol drastically reduces the flow velocity due to the high viscosity (Figure 4.7c,h,m). Flow images were recorded to 3 seconds, therefore the influence of the pore fluid pressure to the velocity cannot be visualized. However as discussed in section 4.1.1, reduction of the friction coefficient shows the presence of the pore fluid flow.

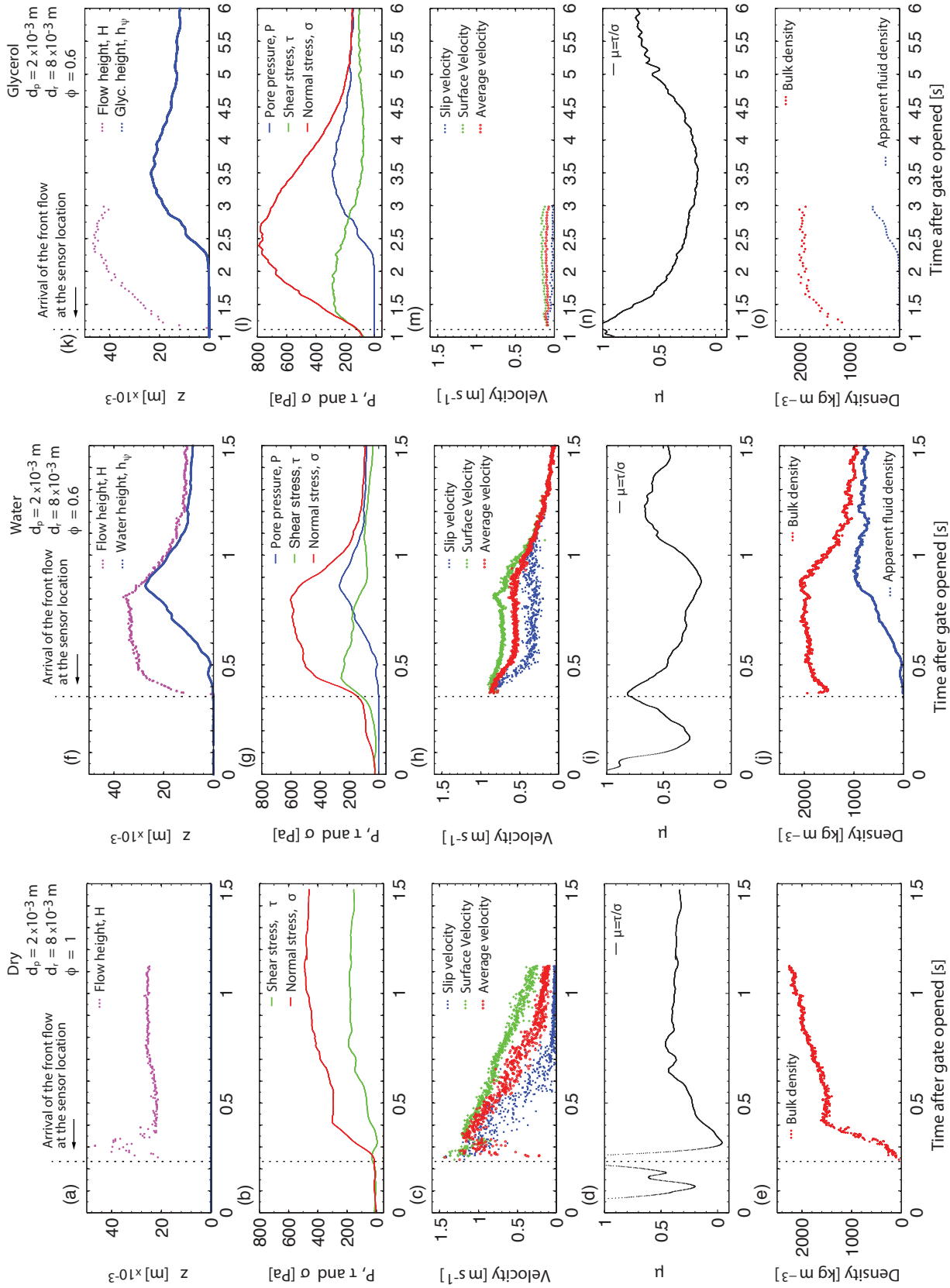


Figure 4.7. Flow evolution from the arrival of the flow to the sensor located at 232×10^{-3} m from the gate flows consisting of 2×10^{-3} m particles diameter over 8×10^{-3} m roughness element diameter (a-e) dry and with solid volume fraction 0.6 (f-i) water and (k-o) glycerol as interstitial fluid.

Velocity distributions

The velocity distributions along the depth, within the pseudo-plug region, have been analysed to study the influence of the interstitial fluid among dry flows, and flows mixed with water and glycerol to solid fraction 0.6 with a fixed roughness element diameter of 8×10^{-3} m (Figure 4.8).

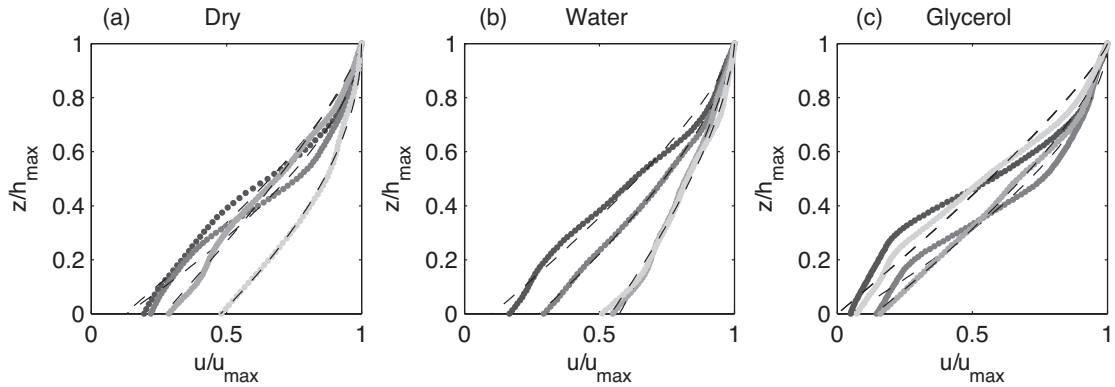


Figure 4.8. Average velocity profiles within the pseudo-plug region at 50% flow length from the front. Flows consist in (a) dry flows, and mixed to solid fraction of 0.6 with (b) water and (c) glycerol. Dashed black lines represents the fit power law. The particle diameter of the experimental flows is represented by the grey lines becoming lighter by increasing particle diameter from 2×10^{-3} , 4×10^{-3} , 8×10^{-3} m and poly-disperse mixture with a mean diameter of 4×10^{-3} m.

The velocity profiles for dry and flows with glycerol reveal different characteristics than those with water as the interstitial fluid. The latter exhibits the greatest velocity gradient near the bottom of the flow with a velocity distribution well fitted by a power law (residual $< 3\%$).

Nonetheless, dry flows and flows with glycerol present two inflection points, exhibiting a similar shape of an inverted ‘S’. The maximum velocity gradient occurs between the bottom and the mid-depth of the flow. The flow appears to form three layers. The middle layer of the flow, with the greatest gradient velocity moves between two layers with lower velocity gradient. The particles within the bottom layer move at very low slip speeds. This limited ability to move can be corroborated by looking at the sides camera images of the flow with mixture of particles and glycerol (Figure 4.9). The evolution of the flow in the bottom layer is highlighted with a dashed blue rectangle. This reveals visually similar patterns in the big white

particles, while the front has moved 0.1 m. The fact that the flow shows these distinguished layers with different velocity gradient reveals a non uniform particle concentration distribution [Armanini *et al.*, 2005; Iverson & Denlinger, 1987].

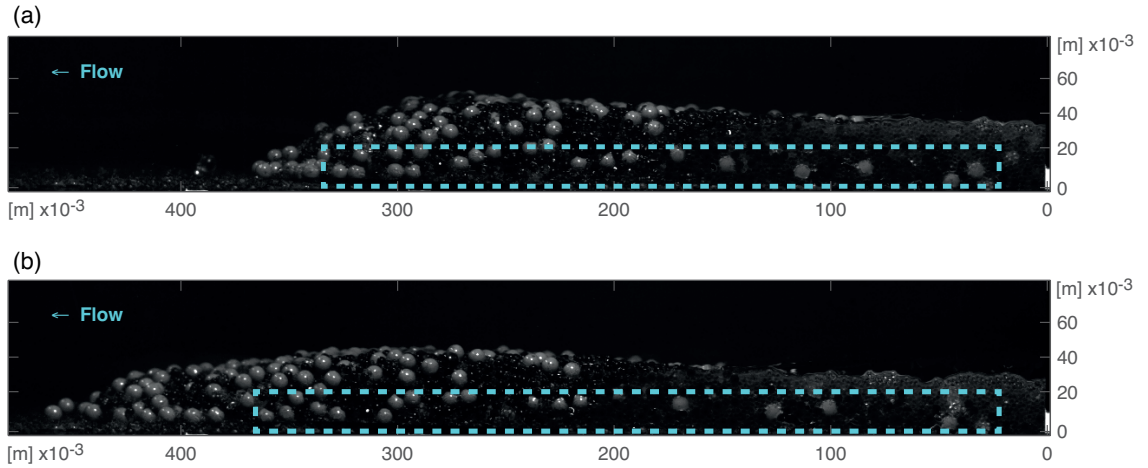


Figure 4.9. Series of side images showing the evolution of the flow after releasing 1 litre volume of mixed glass beads, 2×10^{-3} m (colourless), 4×10^{-3} m (black painted) to 8×10^{-3} m (white painted). These are mixed with glycerol to a solid volume fraction of 0.6, moving down a flume with an inclination angle of 27° over a roughness element diameter of 8×10^{-3} m. The dashed blue rectangle highlight the behaviour of the bottom layer of the flow, where particles seem to move relatively much slower than the flow front.

Experimental measurements by other researches found similar flow behaviours, where velocity profiles depict inflection points near the bottom and the top of the flow [Armanini *et al.*, 2005; Savage, 1979; Su *et al.*, 1993; Takahashi, 1991, 2007].

A simple power-law cannot properly predict these velocity profile, but still server to estimate slip velocity.

Table 4.2 includes the optimized slip velocity (u_{slip}/u_{max}) and exponent β and their residuals ($< 4\%$) except for mono-disperse flows of 2×10^{-3} m particles diameter with glycerol as interstitial fluid (residual $< 7\%$).

The threshold of relative size of the particles and roughness element diameter (d_p/d_r) evaluated in previous section for flows with water as interstitial fluid is not applicable for flows with glycerol as interstitial fluid. The presence of liquid with high viscosity, as in the case of glycerol, reduces the slip velocity approaching a no-slip boundary condition independent of particle size (Figure 4.8c).

Interstitial fluid	Particle size $d_p \times 10^{-3}$ [m]	Slip velocity u_{slip}/u_{max}	β	Residual %
Dry	2	0.12	1.37	3.6
Dry	4	0.13	1.66	3.4
Dry	8	0.27	1.23	1.8
Dry	[2,4,8]	0.48	1.91	0.7
Water	2	0.10	1.32	2.9
Water	4	0.28	1.47	0.8
Water	8	0.57	1.28	0.7
Water	[2,4,8]	0.54	1.51	1.0
Glycerol	2	0.00	1.20	6.8
Glycerol	4	0.05	1.73	3.7
Glycerol	8	0.14	1.44	1.3
Glycerol	[2,4,8]	0.00	1.19	3.5

Table 4.2. Optimised fit parameters for theoretical velocity profiles (Equation 4.1.5) for different particle sizes and interstitial fluid with a roughness diameter element of 8×10^{-3} m.

Flow heights and front velocities

The influence of interstitial fluid on flow heights and to the evolution in time of the flow heights and speed are reviewed in this section. Figures 4.10 illustrate the influence of the interstitial fluid in the heights and front positions in time when comparing dry, and wet flows with water and glycerol to solid volume fraction 0.6.

Increasing viscosity of the interstitial flow (from dry, water to glycerol), the flow speeds decrease drastically and nearly double the maximum height for 2×10^{-3} m particle size flows (Figure 4.10a and 4.10e).

When relative size of particles and roughness exceed $d_p/d_r \geq 1$, the front velocities and heights of the flows appear less dependent on the viscosity of the interstitial fluid (Figures 4.10c and 4.10g).

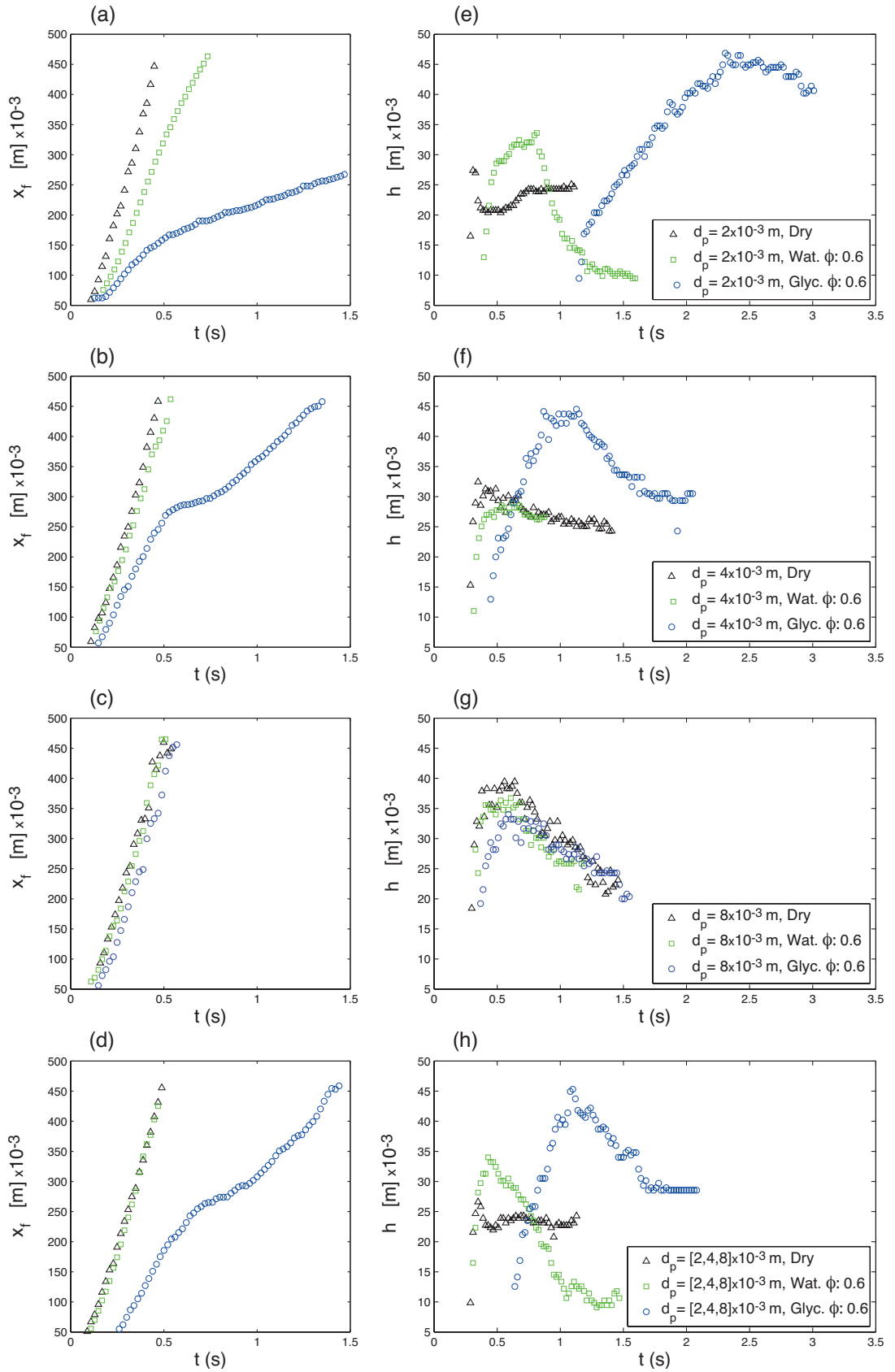


Figure 4.10. Time dependence of front position x_f (a-d) and height of the flow h (e-f). Rows are arranged by particle size, from mono-dispersed 2×10^{-3} m flows to mixtures of 2×10^{-3} , 4×10^{-3} and 8×10^{-3} m particles versus interstitial fluid (dry, water and glycerol). The 8×10^{-3} m roughness element is remained fixed. The flow heights and velocities front are considered within the pseudo-plug region.

4.1.3 Effect of solid volume fraction

Influence of the solid volume fraction on the dynamic characteristics is analysed here for two mono-disperse 2×10^{-3} m flows with solid volume fraction 0.4 and 0.6 over a 8×10^{-3} m roughness element diameter.

The main difference when reducing the solid volume fraction by increasing the fluid volume, is that the lag in pore fluid pressure response decreases (Figure 4.11) and the excess pore fluid pressure enhances the flow mobility by reducing the basal shear stress, agreeing with previous work at large-scale laboratory experiments and field measurements (Iverson *et al.* , 2010; McArdell *et al.* , 2007 respectively). Measurements of the shear stress and the pore fluid pressure reveal that they are out of phase. The shear stress reaches a maximum at the head and begins to decrease just when the pore fluid pressure at the base of the flow appears to start developing (Figure 4.11b,g).

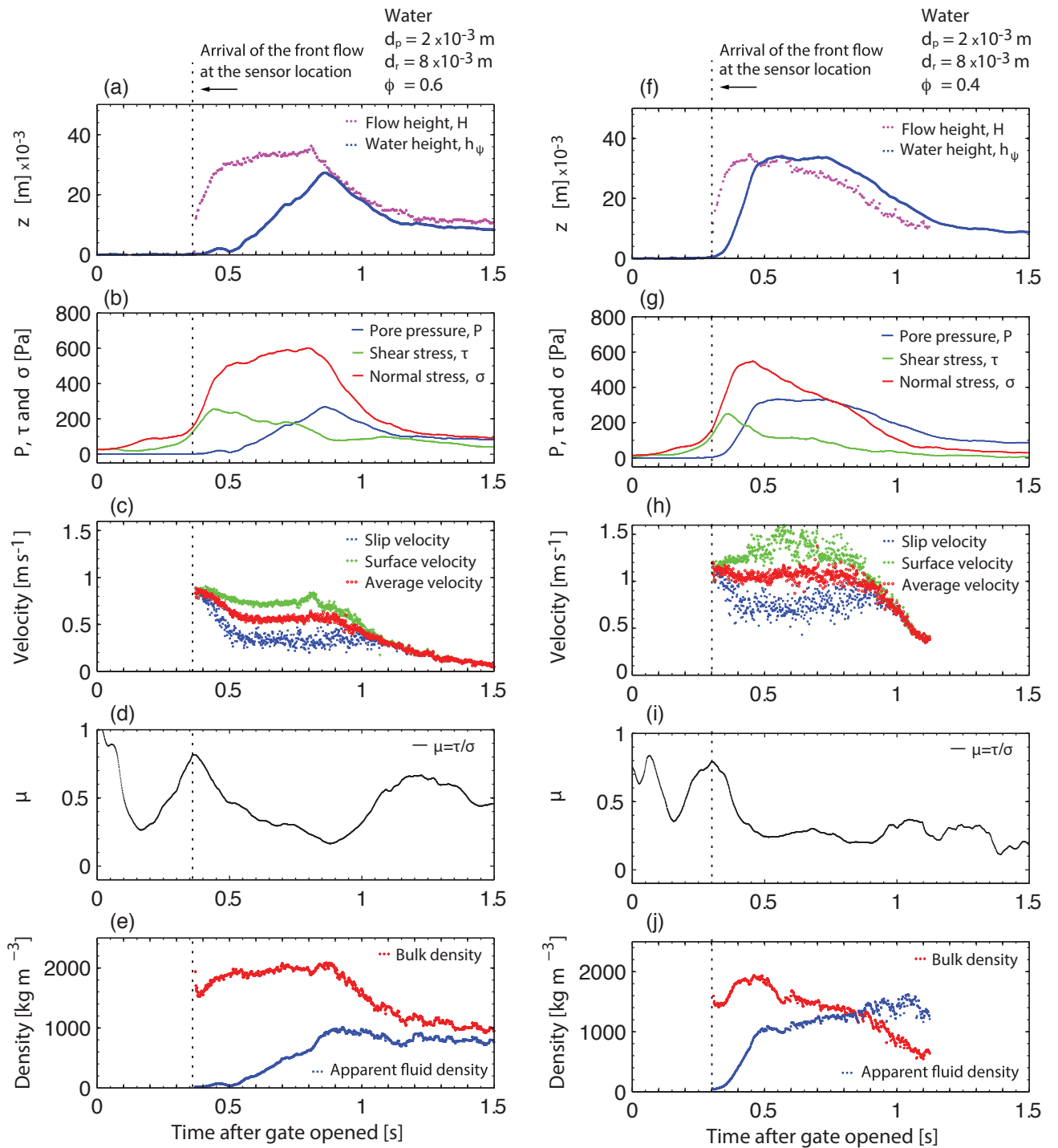


Figure 4.11. Flow evolution from the arrival of the flow to the sensor located at 232×10^{-3} m from the gate of 2×10^{-3} m particle mixed in water with solid volume fraction (a-e) 0.6 and (f-j) 0.4 over 8×10^{-3} m roughness element.

Velocity distributions

The velocity profiles corresponding to the solid volume fractions of 0.4 and 0.6 with water and glycerol are illustrated in Figure 4.12a,b and 4.12c,d respectively.

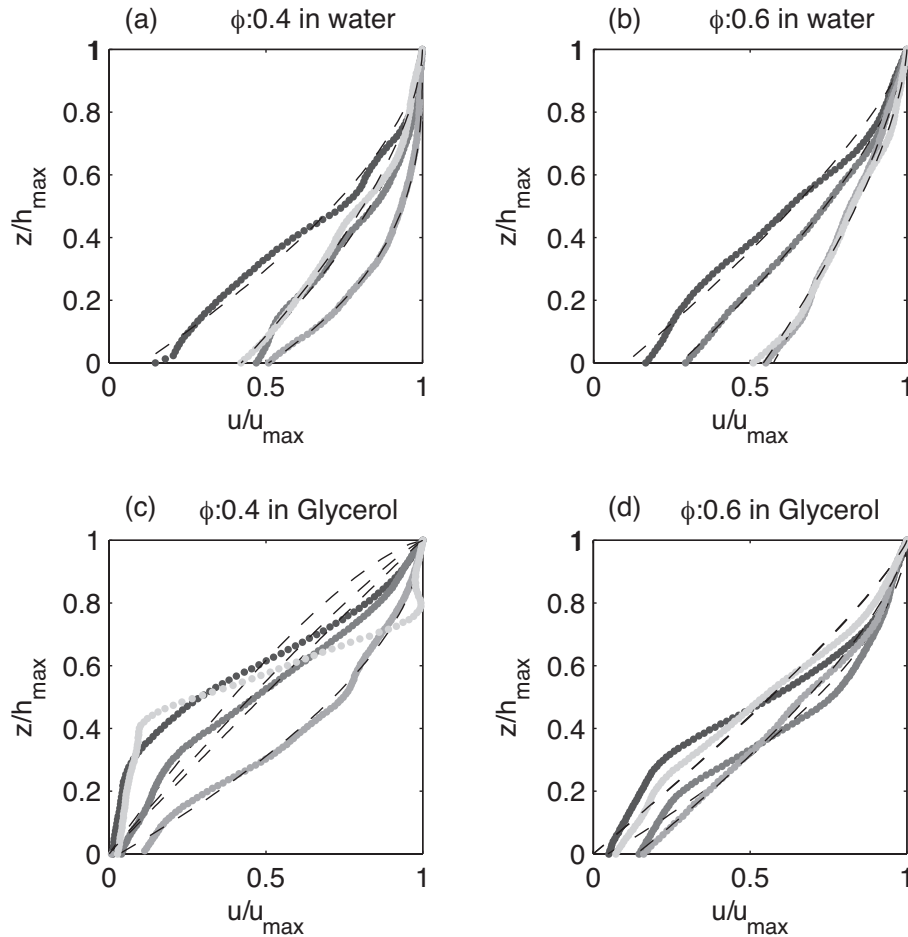


Figure 4.12. Average velocity profiles within the region with low standard deviation ($\leq 150 \times 10^{-3} \text{ m s}^{-1}$) at 50% flow length from the front. Flows consist in mixtures with water to solid fraction of (a) 0.4, (b) 0.6 and mixtures with glycerol to solid fraction of (c) 0.4 and (d) 0.6. Black lines represent the fit velocity (Equation 4.1.5). The particle diameter of the experimental flows is represented by the grey lines becoming lighter by increasing particle diameter from 2×10^{-3} , 4×10^{-3} , 8×10^{-3} m and poly-disperse mixture with a mean diameter of 4×10^{-3} m.

Table 4.3 refers to the optimized slip velocity ($u_{\text{slip}}/u_{\text{max}}$) and exponent β and their residuals. The slip velocity and velocity profiles shapes of the mixtures with water as interstitial fluid are still properly estimated with a power law curve ($< 3\%$).

However, reducing the solid volume fraction, in the case of glycerol as interstitial fluid, with small particles (i.e. 2×10^{-3} and 4×10^{-3} m) and mixed sizes (2×10^{-3} , 4×10^{-3} and 8×10^{-3} m), the power law cannot predict the shape of the velocity profiles (residuals up to 16), but the slip velocity is still appropriated. The reduction of the solid fraction, leads to increase the depth of the lower layer of the flow which moves very slowly (Figure 4.12c). The particle distribution throughout the depth shows higher concentration in the lower part of the flow and above this layer a fluid layer moves faster which contains some suspended particles as illustrated in Figure 4.13. This corresponds to the 'immature flows' discussed in Section 3.1.3.

Interstitial fluid	ϕ	Particle size $d_p \times 10^{-3}$ [m]	Slip velocity u_{slip}/u_{max}	β	Residual %
Water	0.4	2	0.10	1.65	2.8
Water	0.4	4	0.42	1.79	1.5
Water	0.4	8	0.51	2.99	0.6
Water	0.4	[2,4,8]	0.42	1.61	1.2
Water	0.6	2	0.10	1.32	2.9
Water	0.6	4	0.28	1.47	0.8
Water	0.6	8	0.57	1.28	0.7
Water	0.6	[2,4,8]	0.54	1.51	1.0
Glycerol	0.4	2	0.00	0.72	10.3
Glycerol	0.4	4	0.00	0.97	5.0
Glycerol	0.4	8	0.03	1.77	2.1
Glycerol	0.4	[2,4,8]	0.00	0.87	16.1
Glycerol	0.6	2	0.00	1.20	6.8
Glycerol	0.6	4	0.05	1.73	3.7
Glycerol	0.6	8	0.14	1.44	1.3
Glycerol	0.6	[2,4,8]	0.00	1.19	3.5

Table 4.3. Optimised fit parameters for theoretical velocity profiles (Equation 4.1.5) for different particle sizes, solid volume fraction and interstitial fluid with 8×10^{-3} m roughness element diameter.

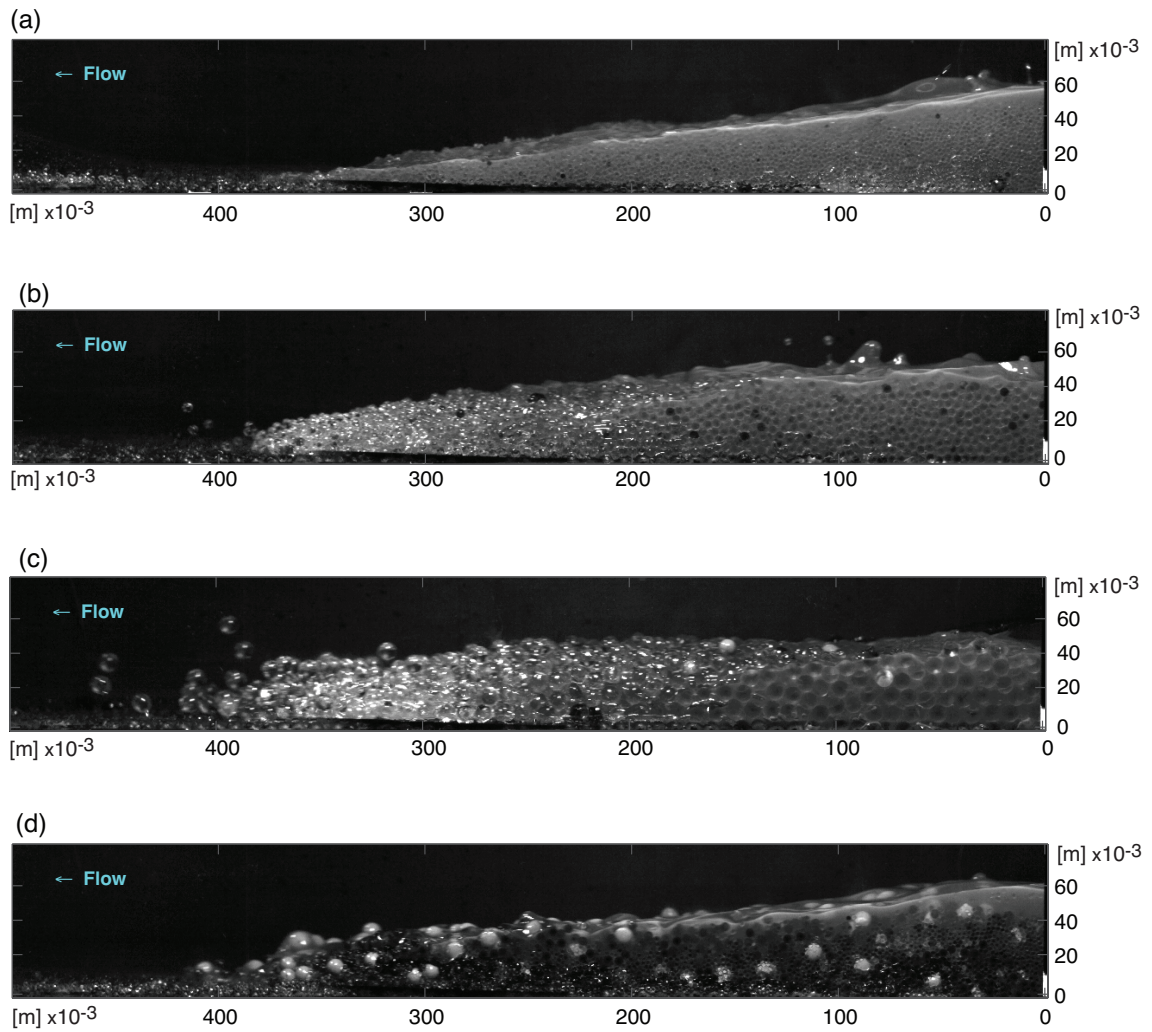


Figure 4.13. Side view of flows in glycerol with solid volume fraction 0.4, moving down a flume with at inclination 27° and a roughness element diameter of 8×10^{-3} m. Mono-disperse mixtures consisting of (a) 2×10^{-3} m, (b) 4×10^{-3} m and (c) 8×10^{-3} m particles. (d) Mixed 2×10^{-3} m (colourless), 4×10^{-3} m (painted black) and 8×10^{-3} m (painted white) glass beads in glycerol. Small particles (i.e. 2×10^{-3} and 4×10^{-3} m) and mixed sizes (2×10^{-3} , 4×10^{-3} and 8×10^{-3} m) cases a fast moving layer of liquid forms at the top surface of the flow. For the mono-disperse flow of 8×10^{-3} m, a dry granular front is formed followed by a saturated tail, with no fluid layer formed.

Flow heights and front velocities

The effect of the amount of fluid content on the flow heights and flow front positions is considered here.

Reducing the liquid content of the mixtures, the front velocity is reduced (Figures 4.14a,b,d). The presence of fluid leads to higher mobility of the flows, as consequence of reduction in the shear stress at the base of the flow.

With mixtures of 8×10^{-3} m particles and the relative size of particles and roughness $d_p/d_r \geq 1$, the influence of the solid volume fraction 0.4 to 0.6 is apparently weaker (Figure 4.14c).

The mixtures containing glycerol as interstitial fluid to solid volume fraction 0.6 and 0.7 at early times, seem to move at the same speed as to solid volume fraction 0.4. Then, the flows drastically decelerates, starting deposition process in the channel of the flume to a complete stop (Figures 4.14a,b).

Flow heights with water mixtures do not show a strong variation with the solid volume fraction.

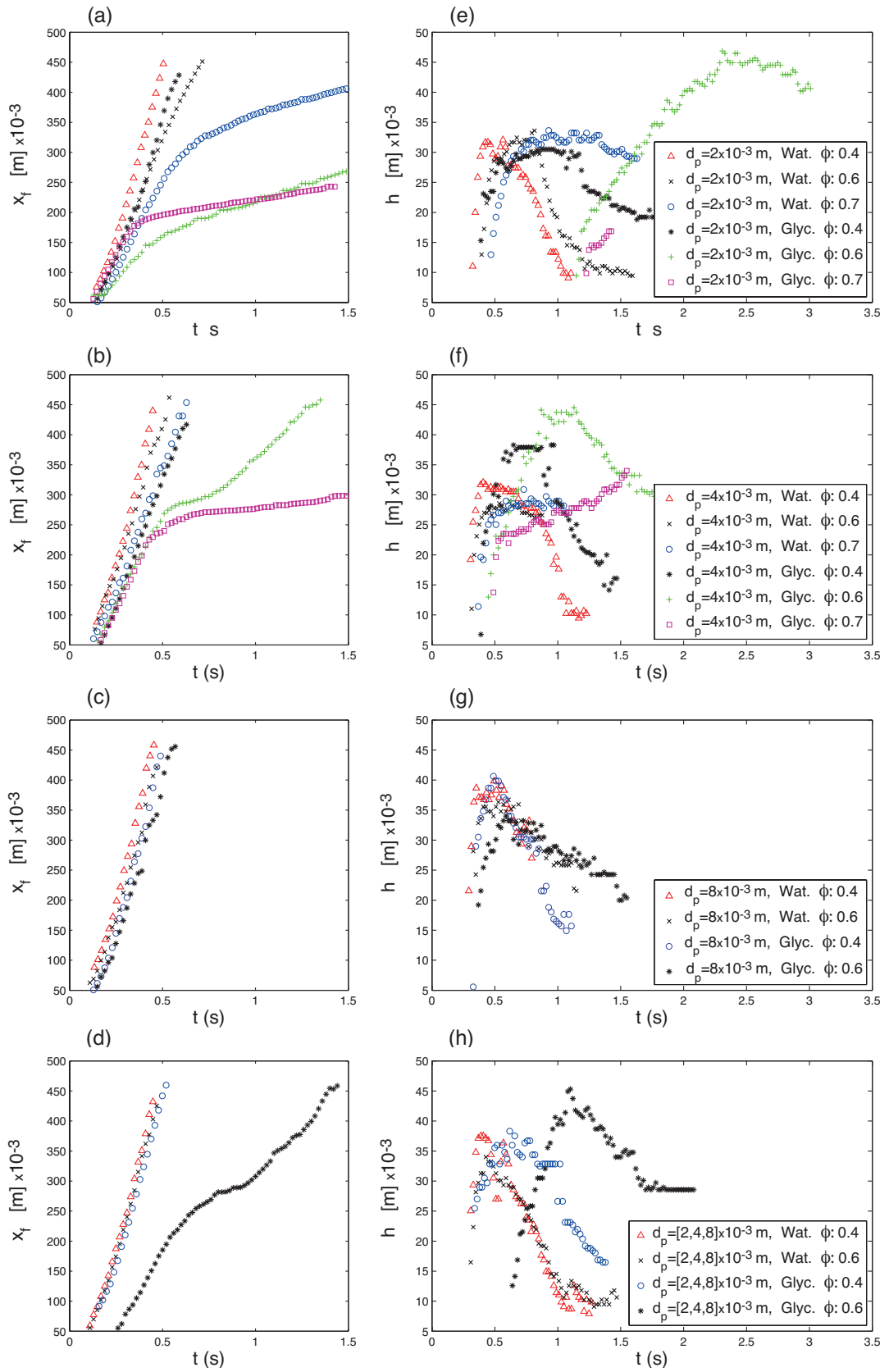


Figure 4.14. Time dependence of front position x_f (a-d) and height of the flow h (e-f). Rows are arranged by particle size, from mono dispersed 2×10^{-3} m flows to mixtures of 2×10^{-3} , 4×10^{-3} and 8×10^{-3} m particles versus solid volume fraction with water and glycerol as interstitial fluids. The 8×10^{-3} m roughness element is remained fixed. The flow heights and velocities front are considered within the pseudo-plug region.

4.2 Flow friction: Shear and normal stress ratio

Measurements of shear and normal stress at the sensor position (i.e. 232×10^{-3} m from the gate) are analysed when varying the particle diameters of the mixture (Figure 4.15), interstitial fluid (Figure 4.16) and solid volume fraction (Figure 4.17). The effective friction coefficient defined as the ratio $\mu = \tau/\sigma$ shows time dependant behaviour. The results show different relation between shear and normal stress when the flow height is growing (at the front of the flow) or decreasing (at the tail), showing a hysteresis process. This effect has also been observed in dense snow avalanches [Bartelt *et al.* , 2012] and laboratory dense granular flows [Pouliquen & Forterre, 2009].

Hysteresis of effective friction depends on the particles size. For flows with 4×10^{-3} m particles, a linear relation seems to describe the relation and it does not show hysteresis (Figures 4.15b). In the case of flows with 8×10^{-3} m, it is very difficult to define a relation between the basal stresses due to the strong agitation of the particles. When small particles are present in the flow, even in the mixture flows, the hysteresis is very evident (Figures 4.15a,d).

For mono-disperse 2×10^{-3} m particle diameter, flows with varying interstitial fluid or volume fraction also present some hysteresis (Figures 4.16 and 4.17).

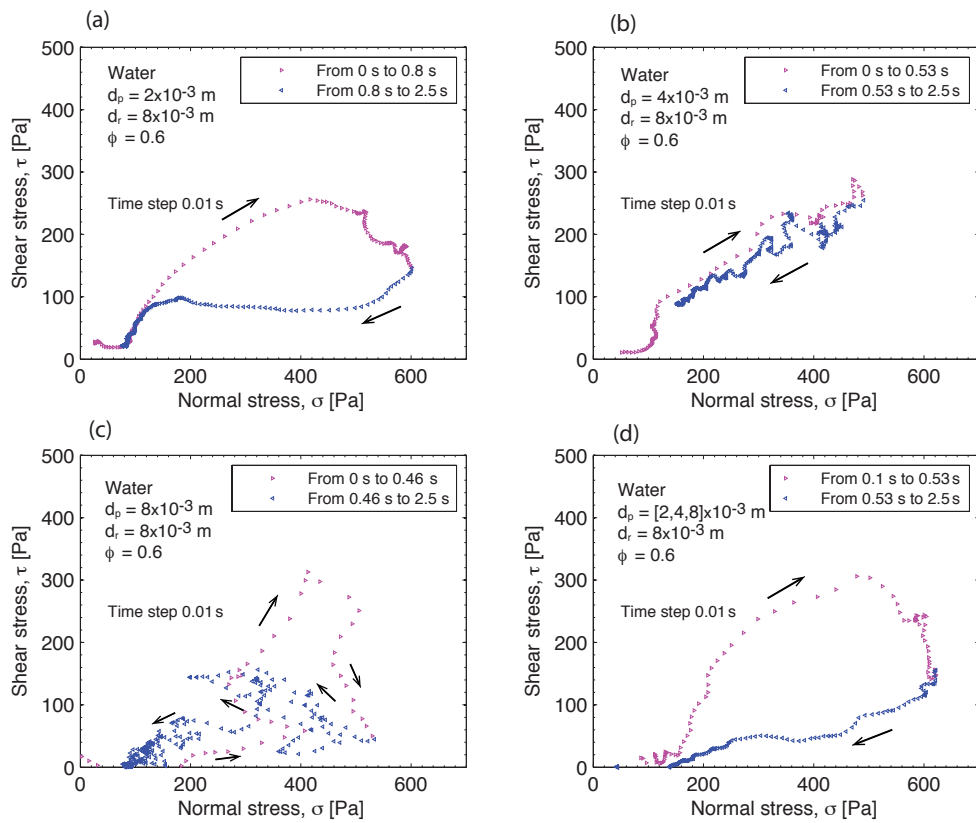


Figure 4.15. Ratio of shear stress τ and normal stress σ at 232×10^{-3} m from the gate of water flow mixtures with solid volume fraction 0.6 over 8×10^{-3} m roughness element diameter of (a) 2×10^{-3} m (b) 4×10^{-3} m (c) 8×10^{-3} m and (d) 2×10^{-3} , 4×10^{-3} and 8×10^{-3} m particles diameter.

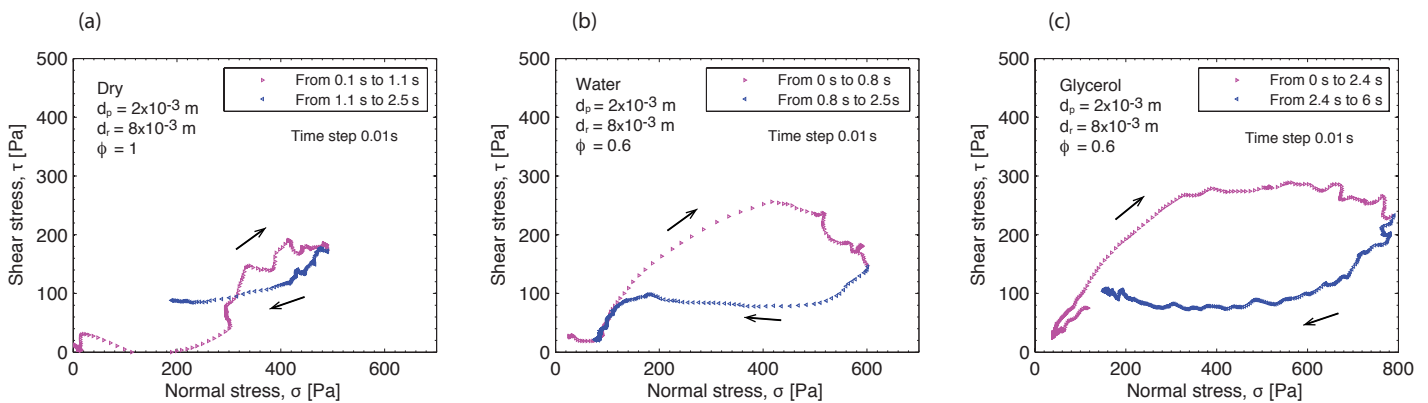


Figure 4.16. Ratio of shear stress τ and normal stress σ at 232×10^{-3} m from the gate of flows consisting of 2×10^{-3} m particles diameter (a) dry and with solid volume fraction 0.6 (b) water and (c) glycerol as interstitial fluid over 8×10^{-3} m roughness element diameter.

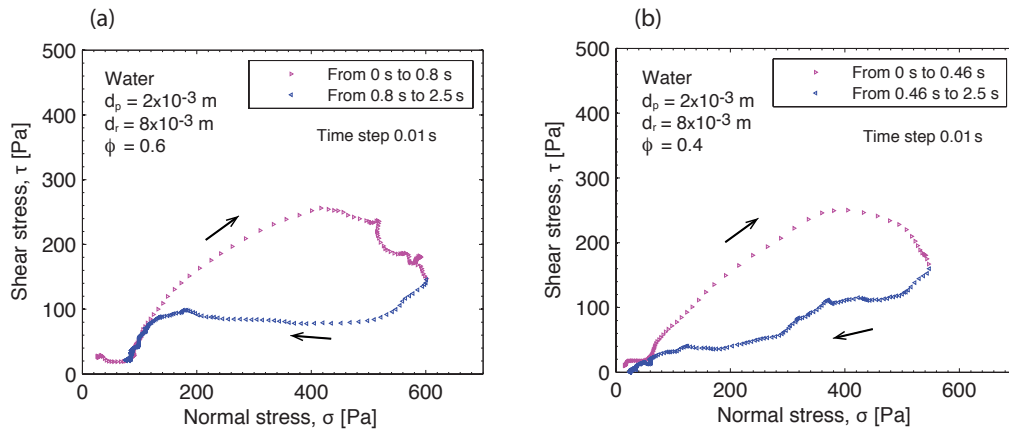


Figure 4.17. Ratio of shear stress τ and normal stress σ at 232×10^{-3} m from the gate of 2×10^{-3} m particle mixed in water with solid volume fraction (a) 0.6 and (b) 0.4 over 8×10^{-3} m roughness element diameter.

4.3 Conclusions

Measurements of the major dynamic features of laboratory-scale debris flow were analysed, showing different regimes from initiation to deposition, such as unsaturated granular front flows, shearing resistance reduction with the presence of pore fluid pressure and liquefied tails.

The evolution of the pore fluid pressure showed a lag relative to the height and basal stresses of the flow. Unsaturated front flows with zero or very low pore fluid pressure were observed in mono-disperse and poly-disperse mixtures. The lag of the pore fluid pressure shows on to increase with the presence of small particles in the mixture and with a more viscous interstitial fluid. Increasing the fluid content in the mixtures enhances flow mobility and reduces the lag of the pore fluid pressure. The relation between the ratio of measured basal stress or basal effective friction coefficient $\mu = \tau/\sigma$ showed a position-dependent behaviour from the front of the flow to the tail, showing a type of hysteresis in the measured values of the basal shear stress in some of the laboratory debris flows. Variations within the calculated bulk density were observed, indicating that an internal rearrangement of the particles in

the vertical directions might be considered.

The experimental results analysed with a power law velocity profile were reported. Flow composition and roughness element diameter have showed influence on the slip and front flow velocities and heights:

- Increasing the roughness diameter element, gives a more pronounced velocity gradients through the flow height, reduction of the slip velocity and reach greater heights. With ratios $d_p/d_r \geq 1$ the slip velocity and flow front speed appear independent on particle size. While $d_p/d_r < 1$ the slip velocity decreases simultaneous with the particle sizes, velocity profiles have slight inflection points and flows become slower.
- Viscous effects intervene in the formation of stratified structures through the flow depth. The dry flows and the flows with glycerol as interstitial fluid exhibited velocity profiles with an inverted 'S' shape, with the formation of sub-layers. Increasing viscosity of the interstitial fluid, increases slip velocity and heights and reduces the front velocity being dependent on size of particles and roughness when $d_p/d_r < 1$.
- The presence of more liquid content of the mixtures increases flow mobility. The increase in height with the reduction of the solid volume fraction is more notable with glycerol mixtures. Flows with ratios $d_p/d_r < 1$ leads to the formation of fluid top layer.

The results from these experiments give a better understanding of some of the underpinning physics of debris flows and probes that flow models should be account with evolving rheologies and variations in density through depth as consequence of the internal rearrangement of the flow.

Chapter 5

Experimental flow simulation with RAMMS

A numerical simulation of laboratory debris flows (Figure 5.1) using a computer model RAMMS (RApid Mass Movements Simulation, [RAMMS, 2013]) is discussed.

5.1 Numerical Model

RAMMS is a numerical simulation model to calculate run-out distance, velocities, flow heights and impact pressures in natural hazards (snow avalanches, debris flows and rockfalls) from initiation to run-out in three-dimensional terrain [Christen *et al.*, 2012]. RAMMS solves the depth averaged equations of mass and momentum, subject to the Voellmy-Salm frictional relationship and the depth averaged random kinetic energy equation (associated with the random movements and inelastic interaction between the particles) using finite volume techniques, [Bartelt *et al.*, 2012; Christen *et al.*, 2010a, 2008, 2010b].

A version of the program RAMMS was created to accommodate the present small scale laboratory experiments.

5.1.1 Governing equations

Two fixed coordinate directions X and Y and $Z(X, Y)$ define the geometry of the flume complete with the run-out area. The coordinates (X, Y) have a resolution of

$5 \times 10^{-3} \text{ m} \times 5 \times 10^{-3} \text{ m}$. A local surface coordinate system (x, y, z) is defined, being (x, y) parallel to flow slope with an angle of 27° and z perpendicular to the local $x - y$ plane (Figure 5.1). The vector $\mathbf{g} = (g_x, g_y, g_z)$ is the gravitational acceleration.

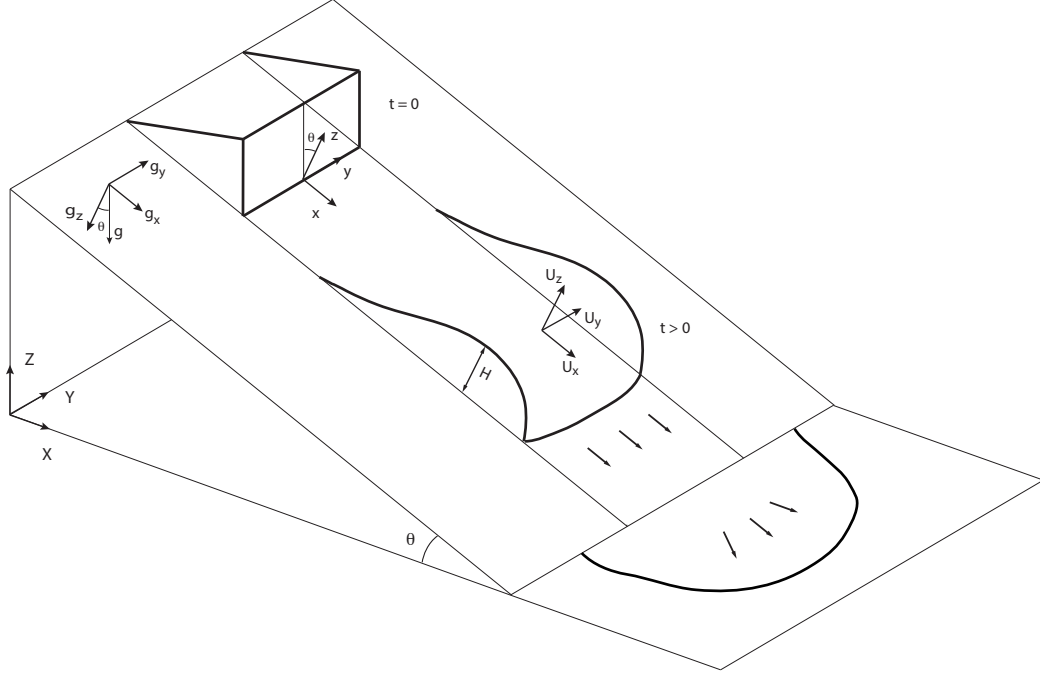


Figure 5.1. The geometry description of the chute $Z(X, Y)$ is given in a horizontal $X - Y$ coordinates system. The local surface coordinates system (x, y, z) with the directions x and y parallel to the flow slope with an angle of θ and z direction is perpendicular to the local $x - y$ plane. The gravitational acceleration and the depth average mean velocity components are $\mathbf{g} = (g_x, g_y, g_z)$ and $\mathbf{U} = (U_x, U_y, U_z)$ respectively.

The laboratory debris flow were characterized by an unsteady and non-uniform flow varying height and velocity. The flow motion is described with a system of depth averaged partial differential equations which comprise the depth averaged mass balance and momentum equations [Pudasaini & Hutter, 2007; Savage & Hutter, 1989]

$$\frac{\partial H}{\partial t} + \frac{\partial}{\partial x} (HU_x) + \frac{\partial}{\partial y} (HU_y) = 0, \quad (5.1.1)$$

$$\frac{\partial HU_x}{\partial t} + \frac{\partial}{\partial x} \left(HU_x^2 + \frac{g_z H^2}{2} \right) + \frac{\partial}{\partial y} (HU_x U_y) = G_x - \tau_x, \quad (5.1.2)$$

$$\frac{\partial HU_y}{\partial t} + \frac{\partial}{\partial x} (HU_x U_y) + \frac{\partial}{\partial y} \left(HU_y^2 + \frac{g_z H^2}{2} \right) = G_y - \tau_y, \quad (5.1.3)$$

where $H(x, y, t)$ is the height of the flow at time t , $U_x(x, y, t)$ and $U_y(x, y, t)$ are

the depth averaged mean velocity parallel to the slope in the x and y direction, respectively and the magnitude of the flow velocity is $\|U\| = \sqrt{U_x^2 + U_y^2}$. It is assumed that the mean velocity in the z -direction (slope normal) is $U_z = 0$.

The right hand side terms, the driving forces acting on the flow, are the gravitational acceleration $G = (G_x, G_y)^T = (Hg_x, Hg_y)^T$ and the frictional deceleration $\tau = (\tau_x, \tau_y)^T$ (discussed in section 5.1.2).

The evolution of the frictional-collisional flows, from unsaturated flow fronts to a fluidized tail are strongly related with kinetic energy balances [Ancy & Evesque, 2000; Bartelt *et al.*, 2012, 2014, 2006; Buser & Bartelt, 2009, 2011b]. Therefore, an energy equation (5.1.7) must be added to the model to account for not only the mean velocity but also velocity fluctuations around the mean and the kinetic energy associated to the particle fluctuations referred as $R(x, y, t)$ [Bartelt *et al.*, 2006; Buser & Bartelt, 2009].

The total velocity of the flow \hat{U} can be divided into mean velocities $\mathbf{U} = (U_x, U_y, U_z)$ and fluctuation velocities $\mathbf{U}_r = (U_{rx}, U_{ry}, U_{rz})$ in such a way that the total velocity is defined as

$$\hat{U}_x = U_x + U_{rx}, \quad \hat{U}_y = U_y + U_{ry}, \quad \hat{U}_z = U_z + U_{rz}. \quad (5.1.4)$$

The total kinetic energy of the particles (per unit density) is the sum of the translational (in the flow direction) and random kinetic energies of the flow

$$K(x, y, t) = \frac{1}{2}(U_x^2 + U_y^2) \quad \text{and} \quad \hat{R}(x, y, z, t) = \frac{1}{2}(U_{rx}^2 + U_{ry}^2 + U_{rz}^2), \quad (5.1.5)$$

being the depth averaged random kinetic energy R of the flow

$$R(x, y, z, t) \equiv \frac{1}{H} \int_0^H \hat{R}(x, y, z, t) dz. \quad (5.1.6)$$

The depth averaged energy equation which refers to the kinetic energy associated to these particle velocity fluctuations is defined

$$\frac{\partial}{\partial t} (HR) + \frac{\partial}{\partial x} (HRU_x) + \frac{\partial}{\partial y} (HRU_y) = \alpha(\tau U) - \beta_R(RH), \quad (5.1.7)$$

where the first right hand side term is the production of the fluctuation energy R which is proportional to the frictional work done by shear forces and the second term represents its decay due to the collision of the particles of the flow. The parameters $\alpha \in [0, 1]$ and $\beta_R \geq 0$ determine the evolution of R from initiation to deposition [Bartelt *et al.* , 2012; Buser & Bartelt, 2009].

5.1.2 Constitutive relations

The frictional shear stress τ based on Voellmy fluid model (Section 1.5.1-iii) is extended to account for the random kinetic energy R [Bartelt *et al.* , 2012; Christen *et al.* , 2010a, 2008, 2010b]

$$\tau_x = \frac{U_x}{\|U\|} \left(\mu(R)g_z H + \frac{g\|U\|^2}{\xi(R)} \right) \quad (5.1.8)$$

and

$$\tau_y = \frac{U_y}{\|U\|} \left(\mu(R)g_z H + \frac{g\|U\|^2}{\xi(R)} \right), \quad (5.1.9)$$

where the coefficient of dry-Coulomb μ and the turbulent ξ friction coefficients are dependent of R . The empirical relationship is defined as

$$\mu(R) = \mu_0 \exp\left(-\frac{R}{R_0}\right) \quad \text{and} \quad \xi(R) = \xi_0 \exp\left(-\frac{R}{R_0}\right) \quad (5.1.10)$$

being μ_0 and ξ_0 the static friction coefficients

$$\mu(R=0) = \mu_0 \quad \text{and} \quad \xi(R=0) = \xi_0. \quad (5.1.11)$$

The $\mu_0 \approx \tan \varphi$ where φ is angle of repose. The parameter R_0 refers to the activation energy to fluidize the flow, which depends of the particle size, total height and particle cohesion [Bartelt *et al.* , 2014]

$$R_0 = C + \tau = C + \rho g_z H \quad (5.1.12)$$

where C is the cohesion between particles (see below).

Extended model to include cohesion

Fluid-particle flows can have inter-granular cohesive forces which add strength to the material and retard mobility fluidity, except when the flow is oversaturated (the particles are completely immersed in the liquid). Even in dry flows (theoretically cohesionless material), the humidity in the air could enhance the formation of tiny liquid bridge between the particles at the contact points, introducing the cohesion effect [Mitarai & Nori, 2006], or even electrostatic forces could also give rise to cohesion between particles [Pudasaini & Hutter, 2007].

The Voellmy equation (Equation 5.1.8 and 5.1.9) is then modified to include cohesion [Bartelt *et al.* , 2014]

$$\tau_x = \frac{U_x}{\|U\|} \left(\mu(R)\sigma + (1 - \mu(R))C - (1 - \mu(R))C \exp\left(-\frac{\sigma}{C}\right) + \frac{\rho g \|U\|^2}{\xi(R)} \right) \quad (5.1.13)$$

and

$$\tau_y = \frac{U_y}{\|U\|} \left(\mu(R)\sigma + (1 - \mu(R))C - (1 - \mu(R))C \exp\left(-\frac{\sigma}{C}\right) + \frac{\rho g \|U\|^2}{\xi(R)} \right). \quad (5.1.14)$$

5.1.3 Numerical solution

The governing equations (5.1.1)-(5.1.3) and (5.1.7) which describe the flow motion can be written as follows:

$$\frac{\partial \mathbf{U}}{\partial t} + \frac{\partial \mathbf{F}(\mathbf{U})}{\partial x} + \frac{\partial \mathbf{G}(\mathbf{U})}{\partial y} = \mathbf{S}(\mathbf{U}) \quad (5.1.15)$$

$$\mathbf{U} = \begin{pmatrix} H \\ HU_x \\ HU_y \\ HR \end{pmatrix} \quad \mathbf{F}(\mathbf{U}) = \begin{pmatrix} HU_x \\ HU_x^2 + \frac{g_z H^2}{2} \\ HU_x U_y \\ HRU_x \end{pmatrix} \quad \mathbf{G}(\mathbf{U}) = \begin{pmatrix} HU_y \\ HU_x U_y \\ HU_y^2 + \frac{g_z H^2}{2} \\ HRU_y \end{pmatrix} \quad (5.1.16)$$

$$\mathbf{S}(\mathbf{U}) = \begin{pmatrix} 0 \\ G_x - \tau_x \\ G_y - \tau_y \\ \alpha(\tau U) - \beta_R(RH) \end{pmatrix}$$

where $\mathbf{U}(x, y, t)$ is the vector of the unknown state variable, $\mathbf{F}(\mathbf{U})$ and $\mathbf{G}(\mathbf{U})$ are the flux functions. The vector $\mathbf{S}(\mathbf{U})$ contains the sources such as mass entrainment by erosion (in the present work it is zero), the gravitational acceleration, G_x and G_y , the production of random kinetic energy, $\alpha(\tau U)$, and sinks due to deposition of particles (it is not considered here and set to zero), the deceleration frictional forces, τ_x and τ_y , and the decay of the random kinetic energy, $-\beta_R RH$.

The model solves the system equation using a finite volume scheme [LeVeque, 2002] over an integral version of the equations, which correctly account for shocks. For the discretization method and time integration refers to Christen *et al.* [2010a].

5.1.4 Model input

The simulations were performed using a single block release with the total volume of the mixture. This block release was defined by the dimensions of the polygonal prism shape of the mixture behind the lock gate before the release.

The two simulations performed correspond to dry mixtures of 2 mm particle diameter over 2×10^{-3} and 8×10^{-3} m roughness element diameter. The initial height before the gate was opened, H_0 , the coefficient α and β_R (Equation 5.1.7), which define the production and decay of the random kinetic energy, and the friction parameters (Section 5.1.2) are summarized in Table 5.1. The parameters have been estimated in order to match the experimental debris flow evolution but are physically

consistent. The two simulations are for identical conditions except for the roughness element diameter, Simulation 1 and 2 correspond to 2×10^{-3} m (smooth surface) and 8×10^{-3} m roughness element diameter respectively.

Symbol	[Units]	Simulation 1	Simulation 2
H_0	m	112×10^{-3}	111×10^{-3}
d_p	m	2×10^{-3}	2×10^{-3}
d_r	m	2×10^{-3}	8×10^{-3}
ρ_p	kg m^{-3}	2600	2600
α	m s^2	0.15	0.25
β_R		2	2
R_0		50	50
ξ_0		500	100
μ_0		0.42	0.75
C	Pa	150	250

Table 5.1. Summary input parameters of the simulations.

5.1.5 Model results

Simulation 1

The model was able to reproduce the mean velocities of the flow (Figure 5.2a), especially at the front of the flow and in the body. However, at the tail the flow decays faster than the experimental flow. The evolution of the height of the flow and the normal stress estimated with the model show similarity to the experimental (Figures 5.2b and 5.2d respectively). The arrival of the flows is observed with an abrupt increase, but the simulation decreases at the tail faster than the experimental flow. This can be explained by looking at the flow height colour map calculated by the model (Figure 5.3). The release zone indicates that there is some material stuck, approximately 20×10^{-3} m (of the 110×10^{-3} m initial height) which has not been released. The shear stress estimated by the model had very poor agreement with the experimental measured data (Figure 5.2c).

The run-out deposit is well estimated with a similar shape and total distance (Figure 5.2a)

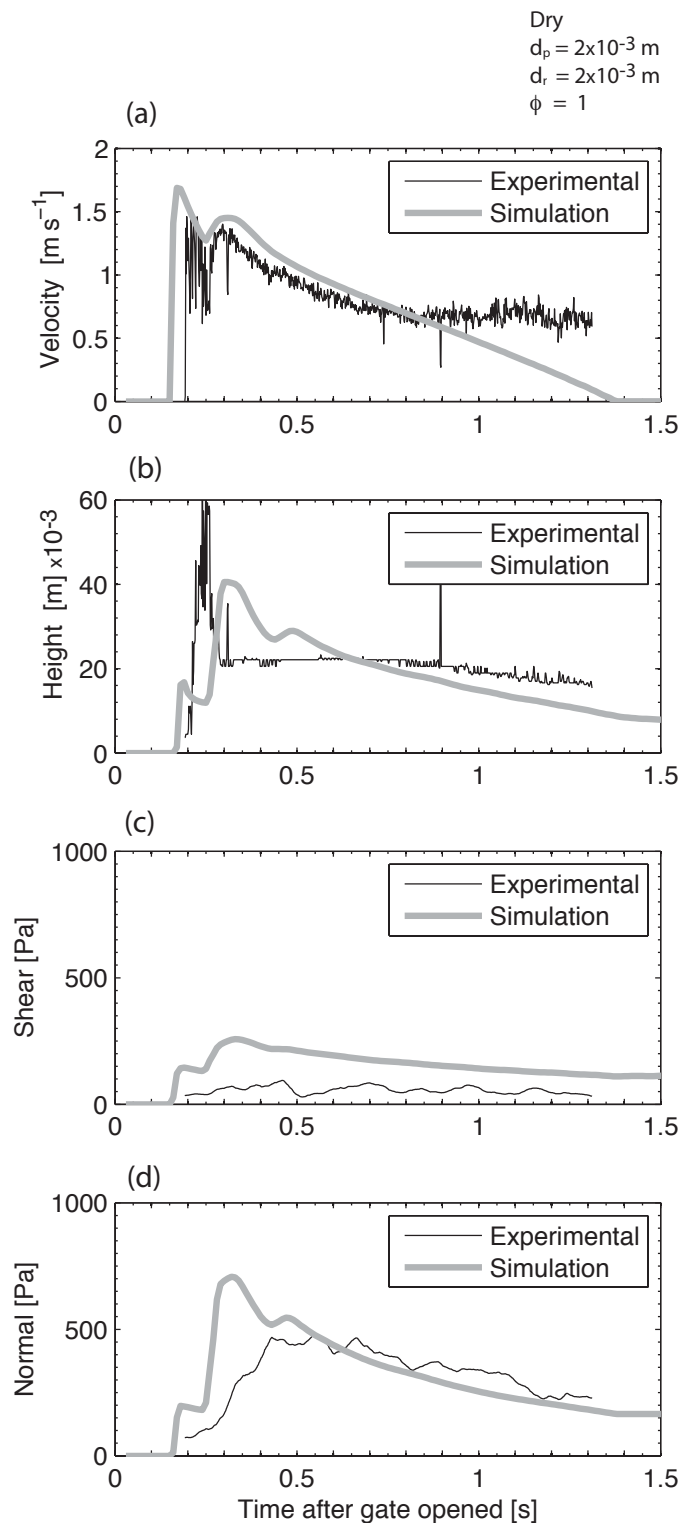


Figure 5.2. Comparison between measured values of the experimental laboratory flow (black line) and the simulation with RAMMS model (grey line) of the evolution of a dry mixture of mono disperse 2×10^{-3} m particle size over 2×10^{-3} m roughness element diameter. (a) Average velocity, (b) height of the flow, (c) shear stress and (d) normal stress.

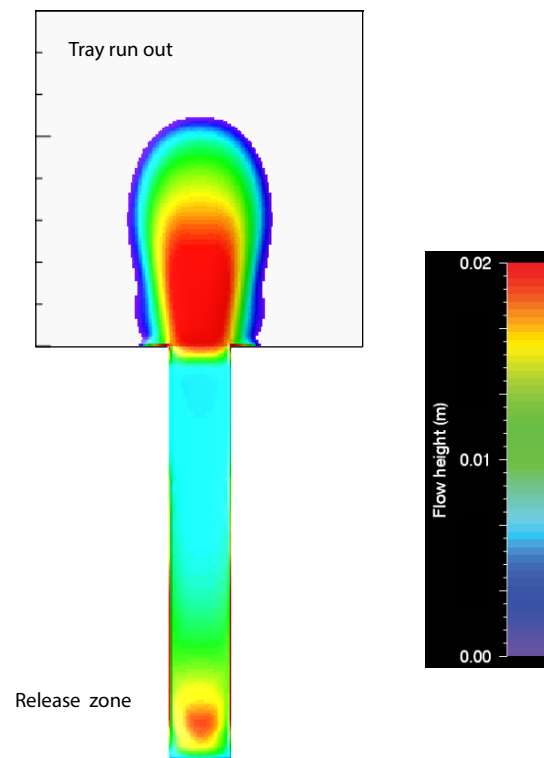


Figure 5.3. Colour map visualising flow height from the release zone along the flume channel to the tray run-out estimated by the model. The release zone shows remaining material approximately the 20×10^{-3} m (of the 110×10^{-3} m initial height) which has not been released.



Figure 5.4. Deposit of the laboratory flow consisting of dry mixture of mono disperse 2×10^{-3} m particle size over 2×10^{-3} m roughness element diameter.

Simulation 2

The model can reproduce the mean velocities (Figure 5.5a). The high roughness element diameter (i.e. 8×10^{-3} m) makes the flow to stop earlier (the velocity decays faster than the previous laboratory flow in simulation 1). The high friction makes more difficult that the flow moves and most of the deposition occurs at the flume channel. The height of the flow estimated by the model shows abrupt increase reaching the biggest height later than the experimental flow (Figure 5.5b). The experimental flow showed the tail of the flow higher than the body due to the deposition of the flow at the flume without reaching the run-out tray.

The shear and normal stresses (Figure 5.2c,d respectively) do not agree with the measurements in the experimental flows. This can be explained due that the high roughness element diameter (i.e. 8×10^{-3} m) the flow exhibit high granular temperature specially near the front (Figure 4.7a), avoiding full contact with the force plate. However, at the tail both have right order of magnitude values where the flow do not exhibited high temperature.

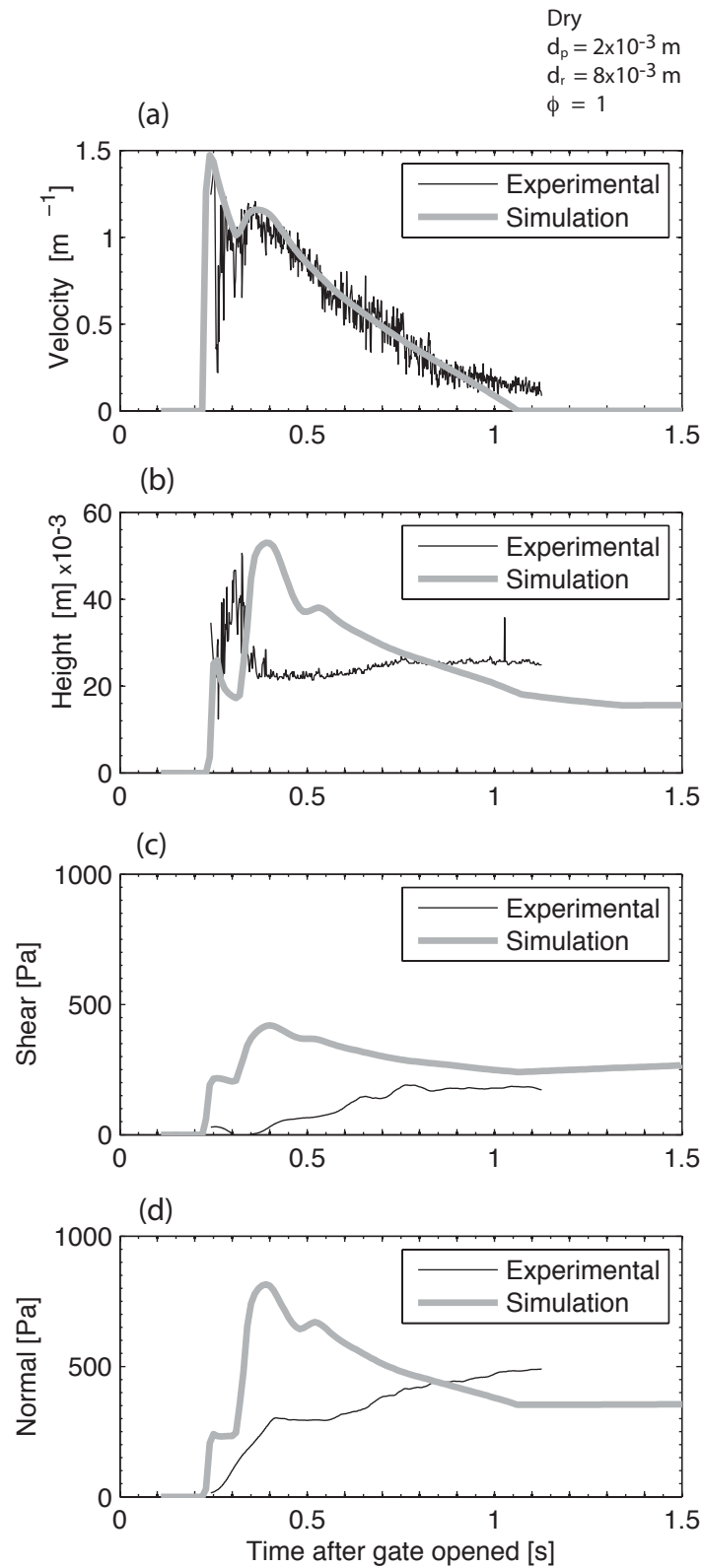


Figure 5.5. Comparison between measured values of the experimental laboratory flow (black line) and the simulation with RAMMS model (grey line) of the evolution of a dry mixture of mono disperse $2 \times 10^{-3} \text{ m}$ particle size over $8 \times 10^{-3} \text{ m}$ roughness element diameter. (a) Average velocity, (b) height of the flow, (c) shear stress and (d) normal stress..

5.2 Conclusions

Data from small scale laboratory experiments were used to validate numerical debris flow model. The model requires to be calibrated to determine the best-fit parameters which are physically consistent. Two simulations with dry flows and same starting conditions were performed under the influence of different roughness element diameter. The model was capable to reproduce the average velocities for both simulations. The height and normal stress showed abrupt front of the flow although are not the best represented by the model. The shear stress measurements di not agree with the model.

Chapter 6

Conclusions

This work describes small scale laboratory debris flow experiments. These experiments were carried out using both dry glass beads and glass beads in mixtures of water or glycerol, which were released from behind a lock gate to flow down an inclined flume. The main objective was to gain a better understanding of how fluid-particle interaction determines dynamic morphological features under the influence of particle size, roughness element diameter, interstitial fluid viscosity and solid volume fraction. The design base of the physical model was after Froude and Reynolds particle number scaling similarity criteria to achieve dynamic similarity with full-scale debris flows, to ensure that gravity forces are correctly scaled and turbulent fluid-particle interaction. A statistical method based on the standard deviation from the local average velocities obtained from the Particle Image Velocimetry technique allowed systematically to define of the characteristic front position and of flow height. Low and high deviation from the local mean define the two co-existent regimes of non-fluctuating and intermittent collisional regions, define by the low and high deviation from the local mean, showed the influence of flow composition and roughness element diameter.

These small scale laboratory debris flow experiments showed morphological characteristics present in full-scale debris flows, characteristics such as the formation of unsaturated, i.e. with a low fluid content front, and a liquefied tail, segregation and levee formation. The evolution of the pore fluid pressure was analysed finding that the lag of the pore fluid pressure shows an increase with the presence of small

particles in the mixtures and with a more viscous interstitial fluid. Reduction of the lag of the pore fluid pressure was observed when increasing the fluid content in the mixtures.

The present laboratory debris flow showed influence in the slip and front velocities and heights depending on flow composition and roughness element diameters, probing the need to account for an evolute rheology and internal rearrangement of the flow through the depth.

The observation of unsaturated fronts in mono-disperse flows implies that size segregation cannot be the only mechanism attributed to this phenomena. The mechanism could be explained by the relative acceleration and interaction between the particles and fluid phase. Future studies, with more advance experiments, should focus on differentiating between the fluid and the particle velocities.

Bibliography

- Adrian, Ronald J. 1991. Particle-imaging techniques for experimental fluid mechanics. *Annual review of fluid mechanics*, **23**(1), 261–304.
- Ancey, C. 2009. Debris Flows. *cole Polytechnique Fdrale de Lausanne, Ecublens, 1015 Lausanne, Switzerland*.
- Ancey, Christophe. 2001. Dry granular flows down an inclined channel: Experimental investigations on the frictional-collisional regime. *Physical Review E*, **65**(1), 011304.
- Ancey, Christophe. 2012. *Gravity flow on steep slope*. Cambridge University Press.
- Ancey, Christophe, & Evesque, Pierre. 2000. Frictional-collisional regime for granular suspension flows down an inclined channel. *Physical Review E*, **62**(6), 8349.
- Ancey, Christophe, Coussot, Philippe, & Evesque, Pierre. 1999. A theoretical framework for granular suspensions in a steady simple shear flow. *Journal of Rheology (1978-present)*, **43**(6), 1673–1699.
- Ao, Sio-Iong, & Gelman, Len. 2010. *Electronic Engineering and Computing Technology*. Vol. 60. Springer Netherlands.
- Armanini, Aronne, Capart, Hervé, Fraccarollo, Luigi, & Larcher, Michele. 2005. Rheological stratification in experimental free-surface flows of granular-liquid mixtures. *Journal of Fluid Mechanics*, **532**, 269–320.
- Bagnold, RA. 1954. Experiments on a gravity-free dispersion of large solid spheres in a Newtonian fluid under shear. *Proceedings of the Royal Society of London. Series A, Mathematical and Physical Sciences*, 49–63.

- Balmforth, NJ, Craster, RV, Perona, P, Rust, AC, & Sassi, R. 2007. Viscoplastic dam breaks and the Bostwick consistometer. *Journal of non-newtonian fluid mechanics*, **142**(1), 63–78.
- Barber, C Bradford, Dobkin, David P, & Huhdanpaa, Hannu. 1996. The quick-hull algorithm for convex hulls. *ACM Transactions on Mathematical Software (TOMS)*, **22**(4), 469–483.
- Bartelt, P., Bühler, Y., Buser, O., Christen, M., & Meier, L. 2012. Modeling mass-dependent flow regime transitions to predict the stopping and depositional behavior of snow avalanches. *Journal of Geophysical Research: Earth Surface*, **117**(F1).
- Bartelt, P., Buser, O., Bühler, Y., Dreier, L, & Christen, M. 2014. Numerical simulation of snow avalanches: Modelling dilatative processes with cohesion in rapid granular shear flows. *In: Proceedings of the 8th European Conference on Numerical Methods in Geotechnical Engineering*.
- Bartelt, Perry, Buser, Othmar, & Platzer, Katharina. 2006. Fluctuationdissipation relations for granular snow avalanches. *Journal of Glaciology*, **52**(179), 631–643.
- Berzi, Diego, & Jenkins, JT. 2009. Steady inclined flows of granular-fluid mixtures. *Journal of Fluid Mechanics*, **641**, 359–387.
- Bisantino, Tiziana, Fischer, Peter, & Gentile, Francesco. 2010. Rheological characteristics of debris-flow material in South-Gargano watersheds. *Natural Hazards*, **54**, 209–223. 10.1007/s11069-009-9462-4.
- Blume, Peter A. 2007. *The LabVIEW Style Book (National Instruments Virtual Instrumentation Series)*. Upper Saddle River, NJ, USA: Prentice Hall PTR.
- Bowman, Elisabeth T., Laue, Jan, Imre, Bernd, & Springman, Sarah M. 2010. Experimental modelling of debris flow behaviour using a geotechnical centrifuge. *Canadian Geotechnical Journal*, **47**(7), 742–762.
- Branney, M.J., & Kokelaar, B.P. 2002. *Pyroclastic density currents and the sedimentation of ignimbrites*. Geological Society Pub House.

- Buser, Othmar, & Bartelt, Perry. 2009. Production and decay of random kinetic energy in granular snow avalanches. *Journal of Glaciology*, **55**(189), 3–12.
- Buser, Othmar, & Bartelt, Perry. 2011a. Dispersive pressure and density variations in snow avalanches. *Journal of Glaciology*, **57**(205), 857–860.
- Buser, Othmar, & Bartelt, Perry. 2011b. Dispersive pressure and density variations in snow avalanches. *Journal of Glaciology*, **57**(205), 857–860.
- Campbell, C.S. 1990. Rapid granular flows. *Annual Review of Fluid Mechanics*, **22**(1), 57–90.
- Christen, M, Kowalski, J, & Bartelt, P. 2010a. RAMMS: Numerical simulation of dense snow avalanches in three-dimensional terrain. *Cold Regions Science and Technology*, **63**(1), 1–14.
- Christen, M, Bühler, Y, Bartelt, P, Leine, R, Glover, J, Schweizer, A, Graf, C, McArdell, BW, Gerber, W, Deubelbeiss, Y, *et al.* . 2012. Integral hazard management using a unified software environment: numerical simulation tool” RAMMS” for gravitational natural hazards. *Pages 23–26 of: 12th Congress INTERPRAEVENT.*
- Christen, Marc, Bartelt, Perry, Kowalski, Julia, & Stoffel, Lukas. 2008. Calculation of dense snow avalanches in three-dimensional terrain with the numerical simulation program RAMMS. *Pages 21–27 of: International Snow Science Workshop.*
- Christen, Marc, Bartelt, Perry, & Kowalski, Julia. 2010b. Back calculation of the In den Arelen avalanche with RAMMS: interpretation of model results. *Annals of Glaciology*, **51**(54), 161–168.
- Costa, J. E. 1984. Physical Geomorphology of Debris Flows. *Developments and Applications of Geomorphology*, 268–317.
- Coussot, P. 1995. Structural similarity and transition from Newtonian to non-Newtonian behavior for clay-water suspensions. *Physical Review Letters*, **74**, 3971–3974.

- Coussot, P., & Meunier, M. 1996. Recognition, classification and mechanical description of debris flows. *Earth-Science Reviews*, **40**(3-4), 209–227.
- Coussot, Philippe, Laigle, Dominique, Arattano, Massimo, Deganutti, Andrea, & Marchi, Lorenzo. 1998. Direct determination of rheological characteristics of debris flow. *Journal of hydraulic engineering*, **124**(8), 865–868.
- Daerr, Adrian. 2001. Dynamical equilibrium of avalanches on a rough plane. *Physics of Fluids (1994-present)*, **13**(7), 2115–2124.
- Dalziel, S. 2000-2012. Digiflow. Advanced image processing for fluid Mechanics. *Dalziel Research Partners*.
- Dalziel, Stuart B. 2012. *Laboratory Modeling*. Vol. 2. CRC Press. Chap. 31, pages 443–456.
- Davies, M.C.R., Bowman, E.T., & White, D.J. 2010. Physical modelling of natural hazards. *Physical Modeling in Geotechnics—7th ICPMG*.
- Davies, Timothy R.H. 1990. Debris-flow surges—experimental simulation. *J. Hydrol.(NZ)*, **29**(1).
- Davies, T.R., Phillips, C.J., Pearce, A.J., & Zhang, X.B. 1992. Debris flow behaviour—an integrated overview. *IAHS Publ*, **209**, 217–225.
- Deubelbeiss, Yolanda, & Graf, Christoph. 2013. Two different starting conditions in numerical debris flow models—Case study at Dorfbach, Randa (Valais, Switzerland). *GRAF, C.(Red.) Mattertal—ein Tal in Bewegung. Publikation zur Jahrestagung der Schweizerischen Geomorphologischen Gesellschaft*, **29**, 125–138.
- Essick, John. 2012. *Hands-on introduction to LabVIEW for scientists and engineers*. Oxford University Press.
- Félix, Gwenaëlle, & Thomas, Nathalie. 2004. Relation between dry granular flow regimes and morphology of deposits: formation of levées in pyroclastic deposits. *Earth and Planetary Science Letters*, **221**(1), 197–213.

- Gidaspow, Dimitri. 1994. *Multiphase flow and fluidization: continuum and kinetic theory descriptions*. Academic press.
- Gonzalez, Rafael C, Woods, Richard Eugene, & Eddins, Steven L. 2004. *Digital image processing using MATLAB*. Pearson Education India.
- Graf, Christoph, & McArdell, Brian W. 2009. Debris-flow monitoring and debris-flow runout modelling before and after construction of mitigation measures: an example from an instable zone in the Southern Swiss Alps. *Pages 3–5 of: La géomorphologie alpine: entre patrimoine et contrainte. Actes du colloque de la Société Suisse de Géomorphologie, edited by: Lambiel, C., Reynard, E. and Scapozza, C.*
- Gray, J.M.N.T, & Thornton, A.R. 2005. A theory for particle size segregation in shallow granular free-surface flows. *Proceedings of the Royal Society A: Mathematical, Physical and Engineering Science*, **461**(2057), 1447–1473.
- Harris, Charles, Vonder Mühl, Daniel, Isaksen, Ketil, Haeberli, Wilfried, Sollid, Johan Ludvig, King, Lorenz, Holmlund, Per, Dramis, Francesco, Guglielmin, Mauro, & Palacios, David. 2003. Warming permafrost in European mountains. *Global and Planetary Change*, **39**(3), 215–225.
- Hsü, Kenneth J. 1975. Catastrophic debris streams (sturzstroms) generated by rockfalls. *Geological Society of America Bulletin*, **86**(1), 129–140.
- Hübl, Johannes, Suda, Jürgen, Proske, Dirk, Kaitna, Roland, & Scheidl, Christian. 2009. Debris flow impact estimation. *Pages 137–148 of: Eleventh international symposium on water management and hydraulic Engineering*, vol. 1.
- Hungr, Oldrich, Evans, SG, Bovis, MJ, & Hutchinson, JN. 2001. A review of the classification of landslides of the flow type. *Environmental & Engineering Geoscience*, **7**(3), 221–238.
- Hunt, M. 2000 (Mar.). Shear flows of granular materials. *Page 5005 of: APS March Meeting Abstracts*.

- Hürlimann, M, Rickenmann, D, & Graf, Ch. 2003. Field and monitoring data of debris-flow events in the Swiss Alps. *Canadian Geotechnical Journal*, **40**(1), 161–175.
- Hutter, K. 2005. Geophysical granular and particle-laden flows: review of the field. *Philosophical Transactions of the Royal Society A: Mathematical, Physical and Engineering Sciences*, **363**(1832), 1497.
- Iverson, Richard M. 2009. Elements of an improved model of debris-flow motion. *Pages 9–16 of: Powders and Grains 2009: Proceedings of the 6th International Conference on Micromechanics of Granular Media*. American Institute of Physics.
- Iverson, Richard M, & LaHusen, Richard G. 1993. Friction in debris flows: Inferences from large-scale flume experiments. *American Society of Civil Engineers (Ed.), Hydraulic Engineering*, **93**.
- Iverson, R.M. 1997. The physics of debris flows. *Reviews of Geophysics*, **35**, 245–296.
- Iverson, R.M. 2003. The debris-flow rheology myth. *Debris flow hazard mitigation: mechanics, prediction, and assessment*, **1**, 303–314.
- Iverson, R.M. 2005. Debris-flow mechanics. *Debris-flow hazards and related phenomena*, 105–134.
- Iverson, R.M. 2012. Elementary theory of bed-sediment entrainment by debris flows and avalanches. *Journal of Geophysical Research: Earth Surface*, **117**(F3).
- Iverson, R.M., & Denlinger, R.P. 1987. The physics of debris flows a conceptual assessment. *Erosion and Sedimentation in the Pacific Rim, International Association of Hydrological Sciences publication no. 165*, 155–165.
- Iverson, R.M., & Denlinger, R.P. 2001. Flow of variably fluidized granular masses across three-dimensional terrain 1. Coulomb mixture theory. *Journal of Geophysical Research*, **106**(B1), 537–552.
- Iverson, R.M., & Vallance, J. W. 2001. New views of granular mass flows. *Geology*, **29**(2), 115–118.

- Iverson, R.M., Logan, M., LaHusen, R.G., & Berti, M. 2010. The perfect debris flow? Aggregated results from 28 large-scale experiments. *Journal of Geophysical Research*, **115**(F3), F03005.
- Jakob, M., & Hungr, O. 2005. *Debris-flow hazards and related phenomena*. Springer Verlag.
- Jakob, Matthias, Hungr, Oldrich, & Hungr, Oldrich. 2005. Classification and terminology. *Pages 9–23 of: Debris-flow Hazards and Related Phenomena*. Springer Praxis Books. Springer Berlin Heidelberg.
- Johnson, A.M., & Rodine, J.R. 1984. *Slope Instability (Landscape systems). Chapter 8: Debris Flow*. John Wiley & Sons Ltd.
- Johnson, Arvid M. 1965. *A model for debris flow: a thesis in geology*. Pennsylvania State University.
- Johnson, Arvid M. 1970. *Physical processes in geology: a method for interpretation of natural phenomena; intrusions in igneous rocks, fractures, and folds, flow of debris and ice*. Freeman, Cooper.
- Johnson, CG, Kokelaar, BP, Iverson, RM, Logan, M, LaHusen, RG, & Gray, JMNT. 2012. Grain-size segregation and levee formation in geophysical mass flows. *Journal of Geophysical Research: Earth Surface (2003–2012)*, **117**(F1).
- Kaitna, R., Rickenmann, D., & Schatzmann, M. 2007. Experimental study on rheologic behaviour of debris flow material. *Acta Geotechnica*, **2**(2), 71–85.
- Kaitna, Roland, & Rickenmann, Dieter. 2007. A new experimental facility for laboratory debris flow investigation. *Journal of Hydraulic Research*, **45**(6), 797–810.
- Koos, Erin, Linares-Guerrero, Esperanza, Hunt, Melany L, & Brennen, Christopher E. 2012. Rheological measurements of large particles in high shear rate flows. *Physics of Fluids*, **24**, 013302.
- Kowalski, Julia, & McElwaine, Jim N. 2013. Shallow two-component gravity-driven flows with vertical variation. *Journal of Fluid Mechanics*, **714**, 434–462.

- Legros, Francois. 2002a. Can Dispersive Pressure Cause Inverse Grading in Grain Flows? *Journal of Sedimentary Research*, **72**(1), 166–170.
- Legros, François. 2002b. The mobility of long-runout landslides. *Engineering Geology*, **63**(3), 301–331.
- LeVeque, Randall J. 2002. *Finite volume methods for hyperbolic problems*. Vol. 31. Cambridge university press.
- Major, J.J., & Pierson, T.C. 1992. Debris flow rheology: experimental analysis of fine-grained slurries. *Water resources research*, **28**(3), 841–857.
- Mason, Robert L, Gunst, Richard F, & Hess, James L. 2003. *Statistical design and analysis of experiments: with applications to engineering and science*. Vol. 474. John Wiley & Sons.
- McArdell, B.W., Bartelt, P., & Kowalski, J. 2007. Field observations of basal forces and fluid pore pressure in a debris flow. *Geophysical Research Letters*, **34**(7), L07406.
- Medina, Vicente, Hürlimann, Marcel, & Bateman, Allen. 2008. Application of FLATModel, a 2D finite volume code, to debris flows in the northeastern part of the Iberian Peninsula. *Landslides*, **5**(1), 127–142.
- Middleton, G.V. 1970. Experimental studies related to problems of flysch sedimentation. *Flysch Sedimentology in North America*, 253–272.
- Mitarai, Namiko, & Nori, Franco. 2006. Wet granular materials. *Advances in Physics*, **55**(1-2), 1–45.
- Mueller, Erich R, Pitlick, John, & Nelson, Jonathan M. 2005. Variation in the reference Shields stress for bed load transport in gravel-bed streams and rivers. *Water Resources Research*, **41**(4).
- Naef, D, Rickenmann, D, Rutschmann, P, & McArdell, BW. 2006. Comparison of flow resistance relations for debris flows using a one-dimensional finite element simulation model. *Natural Hazards & Earth System Sciences*, **6**(6).

- Ogawa, S. 1978. Multitemperature theory of granular materials.
- Otsu, Nobuyuki. 1975. A threshold selection method from gray-level histograms. *Automatica*, **11**(285-296), 23–27.
- Phillips, Christopher J., & Davies, Timothy R.H. 1991. Determining rheological parameters of debris flow material. *Geomorphology*, **4**(2), 101 – 110.
- Pitman, E Bruce, & Le, Long. 2005. A two-fluid model for avalanche and debris flows. *Philosophical Transactions of the Royal Society A: Mathematical, Physical and Engineering Sciences*, **363**(1832), 1573–1601.
- Pope, Stephen B. 2000. *Turbulent flows*. Cambridge university press.
- Potapov, Alexander V, Hunt, Melany L, & Campbell, Charles S. 2001. Liquid solid flows using smoothed particle hydrodynamics and the discrete element method. *Powder Technology*, **116**(23), 204 – 213.
- Pouliquen, O, & Vallance, JW. 1999. Segregation induced instabilities of granular fronts. *Chaos: An Interdisciplinary Journal of Nonlinear Science*, **9**(3), 621–630.
- Pouliquen, Olivier. 1999. Scaling laws in granular flows down rough inclined planes. *Physics of Fluids (1994-present)*, **11**(3), 542–548.
- Pouliquen, Olivier, & Forterre, Yoel. 2009. A non-local rheology for dense granular flows. *Philosophical Transactions of the Royal Society A: Mathematical, Physical and Engineering Sciences*, **367**(1909), 5091–5107.
- Pouliquen, Olivier, Delour, Jean, & Savage, Stuart B. 1997. Fingering in granular flows.
- Pudasaini, Shiva P. 2011. Some exact solutions for debris and avalanche flows. *Physics of Fluids (1994-present)*, **23**(4), 043301.
- Pudasaini, Shiva P. 2012. A general two-phase debris flow model. *Journal of Geophysical Research: Earth Surface (2003–2012)*, **117**(F3).

- Pudasaini, Shiva P, & Hutter, Kolumban. 2007. *Avalanche dynamics: dynamics of rapid flows of dense granular avalanches*. Springer.
- Pudasaini, SP, Wang, Y, & Hutter, K. 2005. Modelling debris flows down general channels. *Natural Hazards & Earth System Sciences*, **5**(6).
- Raffel, Markus. 2007. *Particle image velocimetry: a practical guide*. Springer.
- RAMMS. 2013 (March). *User Manual v1.5 Debris Flow*. WSL Institute for Snow and Avalanche Research SLF.
- Reddy, T Agami. 2011. *Applied data analysis and modeling for energy engineers and scientists*. Springer.
- Reynolds, Osborne. 1885. LVII. On the dilatancy of media composed of rigid particles in contact. With experimental illustrations. *Philosophical Magazine Series 5*, **20**(127), 469–481.
- Rickenmann, D., Laigle, D., McArdell, B., & Hbl, J. 2006. Comparison of 2D debris-flow simulation models with field events. *Computational Geosciences*, **10**, 241–264. 10.1007/s10596-005-9021-3.
- Rondon, L., Pouliquen, O., & Aussillous, P. 2011. Granular collapse in a fluid: Role of the initial volume fraction. *Physics of Fluids (1994-present)*, **23**(7).
- Salm, B. 1993. Flow, flow transition and runout distances of flowing avalanches. *Annals of Glaciology*, **18**, 221–221.
- Sanvitale, N. ; Genevois, R. ; Bowman E. 2010. Optical investigation through a flowing saturated granular material. *Physical Modeling in Geotechnics–7th ICPMG*.
- Savage, S.B. 1984. The mechanics of rapid granular flows. *Adv. Appl. Mech*, **24**, 289–366.
- Savage, SB, & Hutter, K. 1989. The motion of a finite mass of granular material down a rough incline. *Journal of Fluid Mechanics*, **199**, 177–215.

- Savage, Stuart B. 1979. Gravity flow of cohesionless granular materials in chutes and channels. *Journal of Fluid Mechanics*, **92**, 53–96.
- Schaaf, Peter, & Carrasco-Núñez, Gerardo. 2010. Geochemical and isotopic profile of Pico de Orizaba (Citlaltépetl) volcano, Mexico: Insights for magma generation processes. *Journal of Volcanology and Geothermal Research*, **197**(1), 108–122.
- Scheuner, T, Schwab, S, & McArdell, BW. 2011. Application of a two-dimensional numerical model in risk and hazard assessment in Switzerland. *5th DFHM, Padua, Italy*.
- Schofield, A., & Wroth, P. 1968. Critical state soil mechanics.
- Shapiro, L.G., & Stockman, G.C. 2001. *Computer visión*. Prentice Hall.
- Simpson, John E. 1997. *Gravity currents in the environment and the laboratory*. Cambridge University Press.
- Srinivasan, GN, & Shobha, G. 2007. Segmentation techniques for target recognition. *International Journal of Computers and Communications*, **1**(3), 313–333.
- Su, C.G., Lien, H.P., & Chiang, Y.C. 1993. The experiment of velocity and concentration distribution of granules in water-debris flow. *Proc. 4th Int. Symposium on river sedimentation*, **24**(1), 75–82.
- Takahashi, T. 1981. Debris Flow. *Annual Review of Fluid Mechanics*, **13**(1), 57–77.
- Takahashi, T. 1991. *Debris flow*. Monograph of IAHR.
- Takahashi, T. 2001. Mechanics and simulation of snow avalanches, pyroclastic flows and debris flow. *Special Publication of the International Association of Sedimentologists*, **31**, 11–43.
- Takahashi, T. 2007. *Debris flow: mechanics, prediction and countermeasures*. Routledge.
- Unser, Michael. 1999. Splines: A perfect fit for signal and image processing. *Signal Processing Magazine, IEEE*, **16**(6), 22–38.

- WGMS. 2013. Glacier Mass Balance Bulletin No. 12 (2010-2011). Zemp, M., Nussbaumer, S.U., Naegeli, K., Grtner-Roer, I., Paul, F., Hoelzle, M. and Haeberli, W. (eds.), ICSU (WDS) / IUGG (IACS) / UNEP / UNESCO / WMO, World Glacier Monitoring Service, Zurich, Switzerland: 106 pp.
- Yano, Katsumasa, & Daido, Atsuyuki. 1965. Fundamental study on mud-flow. *Bulletin of the Disaster Prevention Research Institute*, **14**(2), 69–83.
- Zanuttigh, B, Lamberti, A, *et al.* . 2002. Granular flow in equilibrium with the bottom: experimental analysis and theoretical prediction. *Nonlinear Processes in Geophysics*, **9**(3/4), 207–220.
- Zuiderveld, Karel. 1994. Graphics Gems IV. San Diego, CA, USA: Academic Press Professional, Inc.